Experimental Measurements of Fall Voltages and Droplet Temperature in GMAW

by

Cory L. McIntosh

A thesis submitted in partial fulfillment of the requirements for the degree of

Master of Science

in

Welding Engineering

Department of Chemical and Materials Engineering
University of Alberta

Abstract

Heat distribution measurements in Gas Metal Arc Welding (GMAW) were concurrently measured at the cathode and anode giving increased insight and prediction capabilities. A calorimeter and water cooled cathode were used to determine energy partitions in GMAW for various electrodes, currents, shielding gases, and waveforms. Fall voltage, droplet temperature, and thermal efficiency measurements were inferred from the heat distribution measurements at the cathode and anode. Secondary and less dominant voltage losses were directly measured or modelled. The simultaneous measurements of all voltage loss regions allowed the determination of arc column voltage potential. All fall voltage measurements were comparable with those found in literature.

Measurements show overall cathode fall voltage is independent from current and waveform selection and appears to be the first time to be experimentally verified for both steel and aluminum. Overall cathode fall voltage was measured to be 12.7 V and 10.9 V for steel and aluminum electrodes respectively. Results indicate that arc composition and temperature could be influencing overall cathode fall voltages. Overall anode fall voltage was independent on current and waveform selection and averaged at 4.7 V and 6.1 V for steel and aluminum respectively. Droplet temperature results indicate that a minimum in temperature exists at the transition point between globular and spray metal transfer in a steel electrode. By modifying small amounts of CO_2 in the shielding gas, droplet temperature can be lowered while still maintaining a similar deposition rate. Values of cathode and anode fall voltages were used to determine deposition rates with results correlating well with other literature.

The experiments performed in this study were able to give consistent measurements when spatter was not an issue and were representative of typical GMAW parameters. Voltage loss and deposition rate calculations correlate well with other literature indicating that fall voltage and droplet temperature measurements are correct. These experimental results in conjunction with models will grant greater understanding and comprehension pertaining to metal transfer, droplet temperature, fume formation, deposition rates, and heat distribution in GMAW.

Preface

The material presented in this thesis are parts of the research project under the supervision of Dr. Patricio Mendez which was funded by Indalco Alloys Inc. This is a paper-based thesis utilizing similar experimental equipment between work. The high similarity between each paper has resulted in numerous sections having a large amount of repeatability.

Chapter 2 of this thesis is a paper published by McIntosh, C., Chapuis, J., and Mendez, P. F., "Effect of Ar-CO_2 Gas Blends on Droplet Temperature in GMAW", Welding Research Supplement, 2016, vol. 95(8), 273-279. Mcintosh, C. was responsible for conducting the bulk of experiments, analysis, and writing. Chapuis, J. conducted experiments and analysis. Mendez, P. F. was the supervisory author and was involved with advising experimental work and paper revisions.

Chapter 3 of this thesis is a paper published by McIntosh, C., and Mendez, P. F., 2017 "Experimental Measurements of Fall Voltages in Gas Metal Arc Welding", Welding Research Supplement. Mcintosh, C. was responsible for conducting the experimental work, analysis of results, and composition of the paper. Mendez, P. F. was the supervisory author and was involved with paper revisions.

Chapter 4 of this thesis is a paper to be published by McIntosh, C., and Mendez, P. F., 2017 "Fall Voltages in Advanced Waveform Aluminum GMAW", Welding Research Supplement. McIntosh, C. was responsible for preparation and conduction of experiments, analysis, and composition of the paper. Mendez, P. F. was the supervisory author and was involved with revisions of the manuscript.

Acknowledgement

I would like to thank Dr. Patricio Mendez for giving me the amazing opportunity to be a part of the Canadian Centre for Welding and Joining (CCWJ). As one of the most charismatic people I have ever met, his inspirational words have driven me to reach for new heights in both my day to day life and in my professional career. The numerous occasions where we bounced crazy ideas about arc physics has been some of the most intense and thought provoking moments of my life and was a breath of fresh air. With an interesting career path ahead, I hope to keep in touch and maintain a strong friendship in the years to come.

I would like to thank everyone involved at the CCWJ including Nairn Barnes, Rebekah Bannister, Goetz Dapp, Mitch Grams, Dmytro Havrylov, Vivek Sengupta, and Gentry Wood. Their help with coming up with insane, wild, and unrealistic ideas has been a blast and has made many days at the lab spontaneous and unpredictable. Whether doing experiments or various sides projects in the lab, the fun, welcoming, and open-mindedness of everyone has made my time at the lab some of the best experiences in my life. The trips to St. John's, Chicago, Las Vegas, and Australia have been some of the biggest highlights of the degree and having everyone there made the experience even better.

My family has supported me throughout my degree and has made my life insurmountably better. They have always supported my decisions and encouraged me to follow my dreams and desires. Their unconditional love, patience, and care have helped me throughout my entire life and words cannot express my gratitude.

Lastly, and most importantly, Celine Mah deserves the most thanks of all. Her love and care was the main reason any of this was possible. Her encouraging and heart-warming personality gave me the confidence to continue forward and will always be cherished. With unknowns in the horizon, her bright smile and cheerful attitude is something that I will always want by my side.

Contents

List of Figures

List of Tables

1. Introduction

1.1. Introduction

Understanding heat distribution in Gas Metal Arc Welding (GMAW) has been a major interest for many industrial companies as this knowledge grants insight into heat inputs efficiencies, deposition rates, metal transfer, penetration, spatter, alloy retention, droplet temperature, and fume formation rates [16]. Knowledge in GMAW has primarily developed from an empirical understanding with most results obtained through trail and error. Greater emphasis is being implemented worldwide to predict GMAW scenarios utilizing models and trends. These models often require experimental information which is unobtainable through modelling. Fall voltages and droplet temperatures are the experimental values of interest in many GMAW models [3, 16–28]. This thesis outlines how experimental measurements of fall voltage and droplet temperature were made.

1.2. Thesis Objective

The objective of this thesis is to assist the welding industry by experimentally determining fall voltages, droplet temperature, and heat distribution in GMAW with various electrodes, welding parameters, waveforms, and shielding gases. These measurements will assist various models giving a better understanding of the GMAW system.

1.3. Thesis Outline

This is a paper-based thesis with each chapter comprising of its own set of objectives, experiments, and conclusions. The three papers use the same experimental setup and calculations and are more thoroughly outlined in Appendix A.

Chapter 2 focuses on determining droplet temperature as a function of current and shielding gas in GMAW. This work shows that a droplet temperature minimum exists at the transition point between globular and spray for all shielding gases used.

Chapter 3 focuses on determining overall cathode and anode fall voltages in a GMAW steel system as a function of current and metal transfer. This was the first time all fall voltages were

simultaneously measured as a function of current. These results indicate that overall cathode and anode fall voltage are constant with current with other voltage losses dependent on current.

Chapter 4 is similar to chapter 3 but with an emphasis on waveform selection in aluminum GMAW. It was found that waveform selection had very little influence on results at the currents tested. Trends found were comparable with total voltage loss values. Differences in the overall cathode fall voltage values between steel and aluminum indicate that the arc's composition and temperature could be affecting results.

2. Effect Of Ar - CO_2 Gas Blends on Droplet Temperature in GMAW

2.1. Introduction

Fume emission in Gas Metal Arc Welding (GMAW) is a major health concern to workers due to the numerous carcinogenic and respiratory issues associated with metallic inhalation [14, 19, 26, 29–31]. Industrial welding shops have utilized several methods to alleviate fume inhalation problems such as proper ventilation, different waveforms, wire selection, and/or welding parameters [32]. These methods have proven to be effective but with health organizations continually mandating a lowering of the Occupational Exposure Limit (OEL) new methods are needed to reduce fume generation [30].

Fume generation has been extensively studied both experimentally [14, 21, 24, 26, 30] and theoretically [19, 20, 29, 33]. In GMAW, the majority of fumes are created at the electrode due to overheating at the anode surface. This is evident in the fume emission differences exhibited between autogenous Gas Tungsten Arc Welding (GTAW) and GMAW [19, 26]. Models of GMAW during electrode heating have shown that droplet temperature is influenced by droplet size [19, 21] and metal transfer mode [3] and can qualitatively help understand fume emission.

It has been determined from models and past experimentation that current is an important experimental variable due to its role in resistive heating and metal transfer mode [19]. Different welding parameters have resulted in variation when measuring droplet temperature and has ranged between 1700 °C - 2700 °C (3092 °F - 4892 °F) depending on anode composition, cathode composition, and shielding gas [1–3, 16, 34–44].

Literature focuses primarily on determining temperature distributions as a function of current. Unlike others who had looked at a large range current, Soderstrom's [3, 45] work focused on measuring droplet temperature in the transition zone between globular and spray transfer. The transition zone is an area commonly referred to as projected spray transfer and is an area where droplet detachment frequency is higher than globular transfer without excessive heating found in spray transfer [30, 46]. Soderstrom found a local minimum in droplet temperature in the transition zone between globular and spray metal transfer in carbon steel, stainless steel, and aluminium using pure Ar shielding gas. The transition zone was found to be around 205 A

at 1800 °C (3272 °F) in carbon steel and is useful to the development of new waveforms as the lower droplet temperature can reduce fume emission. Temperature values of 1800 °C (3272 °F) were also found in globular transfer but poor welding characteristics make globular metal transfer mode undesirable in industry [30]. Soderstrom's work was later verified by Scott's [2] work which had very similar results for carbon steel. Scott found the transition zone at 205 A with a minimum in droplet temperature of ∼2200 °C (3992 °F).

Siewert [43] used a combination of pyrometry and calorimetry to measure droplet temperature for a pure Ar, pure iron system in pulsed GMAW. Siewert found the average droplet temperature to be 2200 °C (3992 °F) and showed that the surface temperature of droplets is significantly higher near the anode arc attachment spot reaching upwards of 2700 °C (4892 °F) due to localized overheating. Yamazaki and Tanaka [41, 42, 47] measured overall droplet temperature for carbon steel in constant voltage mode using pure CO_2 and 20% CO_2 - 80% Ar shielding gas environments. Tanaka's results found that droplet temperature ranged between 1900 °C - 2300 °C (3452 °F - 4172 °F) when utilizing pyrometry. Pyrometry is beneficial as the surface temperature of the droplet can be measured without disruption of the system but is not always the best indication of the overall droplet temperature [3]. Large uncertainties in pyrometry can arise due to the metallic evaporation and plasma radiation associated with welding processes [41].

Zielinska [48, 49] looked at the effect of increasing CO_2 in Ar - CO_2 blends and found that the transition current between globular and spray transfer increases with higher concentrations of CO_2. Zielinska [48] found a transition current of ∼252 A, 280 A, and 330 A for pure Ar, 5% CO_2 - 95% Ar, and 10% CO_2 - 90% Ar respectively.

The region near the transition zone has shown a minimum in droplet temperature utilizing pure Ar shielding gas [3]. Droplet temperature using Ar - CO_2 blends has been determined in past literature but a comprehensive graph has yet to be determined showing the change in droplet temperature with changing current and CO_2 concentration. This paper focuses on exploring the effects of Ar - CO_2 shielding gas blends on the overall droplet temperature near the transition zone.

2.2. Experimental Setup

The experimental setup is identical to the calorimeter setup used by Scott as seen in Figure 2.1 [1, 2]. The setup is divided into several parts including the solid state calorimeter, water cooled copper cathode, custom contact tip, and synchronized high speed videography with data acquisition. The unique nature of this setup allows cathodic and anodic heat inputs to be measured independently. Measurements are limited to free-flight metal transfer modes only and cannot measure short-circuit waveforms.

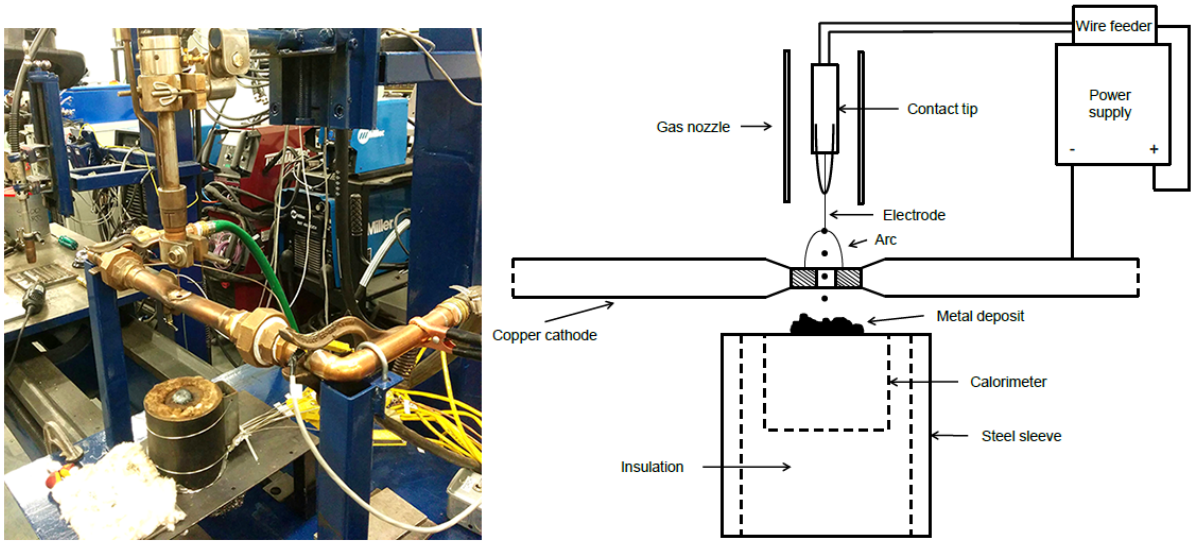

Fig. 2.1: Solid state copper calorimeter and copper cathode setup (not to scale) [1, 2].

Two welding power supplies were used in this research. Tests utilizing pure Ar and 5% CO_2 - 95% Ar shielding gas were performed with a Lincoln Power Wave S500 and a Lincoln 84 Dual Feeder using program 5 (Weld set reference: Z153615). Tests utilizing 10% CO_2 - 90% Ar shielding gas were performed with a Miller PipePro 450RFC and a Miller PipePro Single Feeder. All welds were done in constant voltage mode in direct current electrode positive polarity. The welding torch was a Tregaskiss Tough Gun I.C.E. water-cooled robotic MIG torch. The wire used in all experimentation was a 0.045 in. (1.143 mm) diameter ER70S-6 carbon steel electrode. Shielding gases were mixed to 35 SCFH (16.52 l/min) using an OMEGA FL-6GP-40ST-40ST-40ST gas proportioning rotameter.

The main function of the water cooled copper cathode was to maintain an arc during experimentation. The design of the copper cathode allowed for passage of molten droplets from the

electrode to the calorimeter as shown in Figure 2.1. The flow rate of the water was monitored with a Kings 7520 7C-02 flow meter. Typical water flow rate was between 0.34 - 1.00 ± 0.02 USGPM (1.29 - 3.79 ± 0.076 l/min). Omega GKQSS-18G-12 K type thermocouples were used to measure the inlet and outlet temperature of the water with an accuracy of ± 0.4%.

A solid state high-purity copper calorimeter was used to calculate initial droplet temperature. The cylindrical calorimeter had a height of 35 mm (1.38 in.), diameter of 50.8 mm (2 in.) and was positioned 127 mm (5 in.) below the water cooled copper cathode. A solid state calorimeter was more desirable than water based calorimeters as there is less error due to no heat loss from water evaporation [2]. 10 Omega GKQSS-18G-12 K type thermocouples were used to measure the temperature of the calorimeter. Droplets that fell onto the calorimeter were weighed using an Adam PGW 4502e scale with an accuracy of ± 0.01 g (0.0022 lbs). Properties of pure copper and pure iron were used for the calorimeter and wire respectively [50]. With known properties of the copper and wire, known mass of the droplets, and known temperature increase in the calorimeter, the change in enthalpy was used to calculate the initial droplet temperature. Calibration tests using molten tin has shown that the accuracy of the enthalpy measurements varies by ± 1.1% when the final calorimeter temperature is kept below 187 °C (368.6 °F).

A known electrode extension allows for proper calculation of resistive heating into the wire electrode. Industrially used contact tips can have variance in the measured electrode extension distance due to unknown contact points within the contact tip [2]. To ensure that a constant electrode extension was maintained during testing, a custom contact tip was used as shown in Figure 2.2 [2]. The custom contact tip gives a known contact point used to measure the electrode extension during welding. A known electrode extension allows for more repeatable experimentation and can be used for future calculations. A tungsten indicator was set to the desired electrode extension distance. Voltage settings were adjusted during welding until the desired electrode extension was visually verified using the tungsten indicator and high speed camera. Current was controlled by varying wire feed speed with a resolution of 1 inch/min (0.0254 m/min). Voltage settings changed based on the wire feed speed value selected. All tests done in this research had an electrode extension of 12.5 mm (0.49 in.) and arc length of 12.5 mm (0.49 in.).

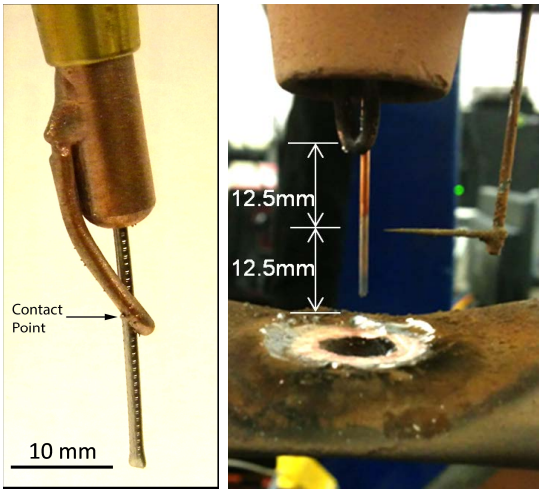

Fig. 2.2: Custom contact tip used during experimentation to determine exact contact point. A tungsten indicator was used to set an exact electrode extension visible in the high speed videos [2].

High speed videography was taken during experimentation to confirm that the desired metal transfer mode was achieved. A Phantom V210 high speed camera was used with a 850 nm long wave pass filter to capture the free-flight metal transfer. Voltage and current data acquisition was captured alongside the high speed videography to determine average welding parameters. A LEM LV 25-P voltage transducer and LEM HTA 600-S current transducer were used to capture voltage and current with an accuracy of $\pm 0.9\%$ and $\pm 1.0\%$ respectively. The analog signals from these transducers were captured with a National Instruments USB 6351 X series data acquisition device at 50,000 Hz. The high speed camera was connected with the National Instruments data acquisition device allowing synchronization of the high speed videos with the data acquisition. The synchronized high speed videos allowed for close monitoring of any changes found in experimentation.

The combination of the water cooled cathode, calorimeter, and data acquisition system were used to calculate overall thermal efficiency and heat distribution of the system. Overall heat input of the system was calculated with Ohms law utilizing average voltage and current readings. Heat input into the droplets and the cathode were calculated and added to compare with the overall heat input. Temperature differences in the water inlet and outlet reached steady state after approximately 20 seconds. Welding was maintain for approximately 30 seconds in the efficiency calculation tests to ensure steady state was reached.

2.3. Results

Droplet temperature was measured for pure Ar, 5% CO_2 - 95% Ar, and 10% CO_2 - 90% Ar shielding gases as a function of current and is summarized in Table 2.1. The pure Ar tests are shown in Figure 2.3 showing the changes in metal transfer mode as a function of current. The results of all droplet temperature measurements are shown in Figure 2.4. All shielding gases had a local minimum droplet temperature and showed a change in metal transfer mode. Experimentation was not extended to higher currents to avoid streaming or rotating metal transfer mode. The trend lines shown in Figure 2.3 and 2.4 are an estimate and were manually fitted. Current work aims at developing a modelled formula for objective fitting. The 5% CO_2 - 95% Ar tests had the lowest minimum droplet temperature at 2119 °C (3846.2 °F) with the pure Ar and 10% CO_2 - 90% Ar having a similar minimum droplet temperature of ∼2230 °C (4046 °F).

Table 2.1: Summary of droplet temperature utilizing different Ar - CO_2 blends

Shielding gas	Droplet temperature range (°C)	Transition temperature (°C)	Transition current (A)
Pure Ar	2050-2709	2254 ± 24	206 ± 2.0
5% CO_2 - 95% Ar	2039-2715	2119 ± 22	230 ± 2.3
10% CO_2 - 90% Ar	2223-2550	2223 ± 24	270 ± 2.7

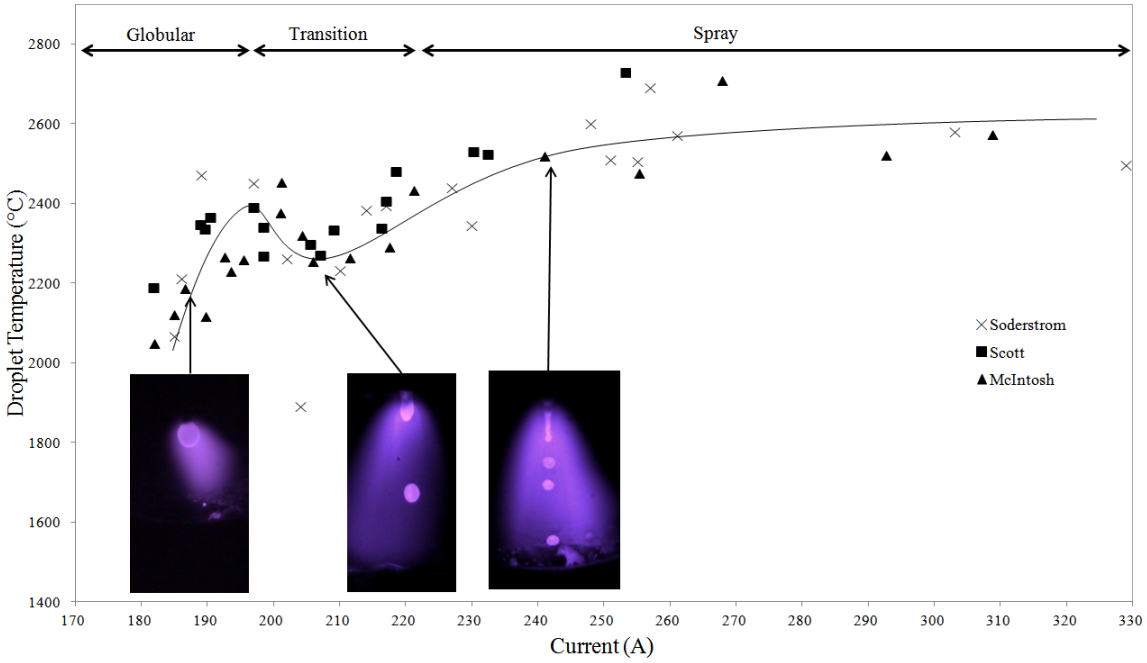

Fig. 2.3: Droplet temperature measurements in GMAW using a 0.045 in. (1.143 mm) diameter ER70S-6 carbon steel wire with pure Ar shielding gas [2, 3]. Photographs on the graph show metal transfer modes at different currents.

.

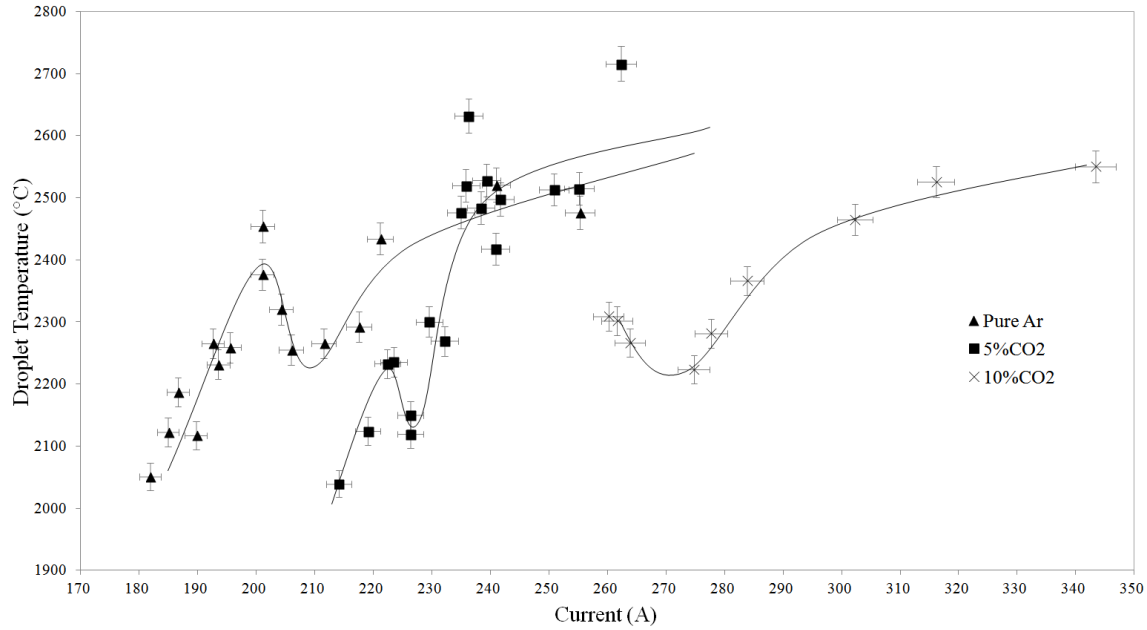

Fig. 2.4: Effect of Ar - CO_2 shielding gas blends on droplet temperature using a 0.045 in. (1.143 mm) ER70S-6 carbon steel wire. Electrode extension and arc length were both 12.5 mm (0.49 in.).

A higher concentration of CO_2 in the Ar - CO_2 blends was found to shift the transition zone to higher currents. The transition zone was located at approximately 206 A, 230 A, and 270 A in the pure Ar, 5% CO_2 - 95% Ar, and 10% CO_2 - 90% Ar tests respectively. Figure 2.5 shows the

difference in metal transfer modes between a pure Ar and 5% CO_2 - 95% Ar test. Both tests in Figure 2.5 have an average current of 241 ± 2 A, droplet temperature of ∼2500 ± 27 °C (4532 ± 48.6 °F), and resemble spray transfer. The tail in the pure Ar test is longer indicating easier droplet detachment.

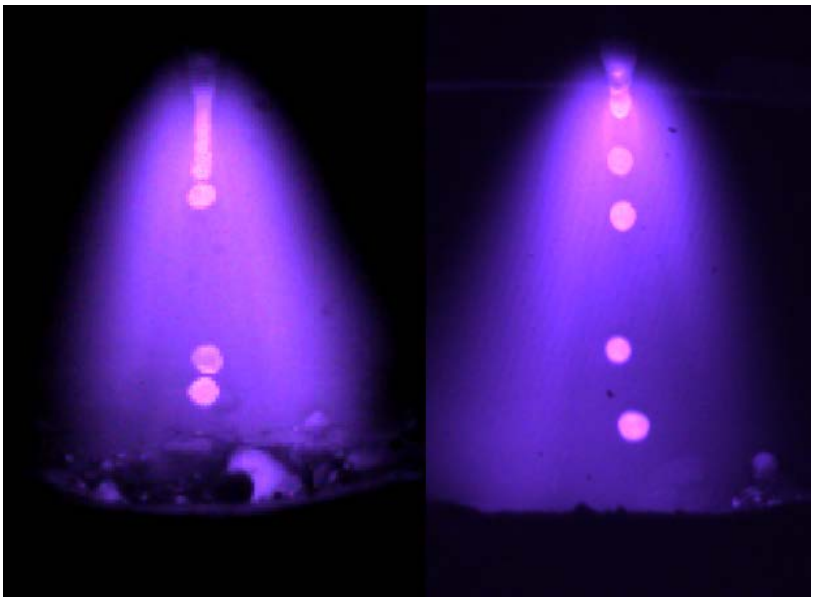

Fig. 2.5: Left - pure Ar. Right - 5% CO_2 - 95% Ar. Effect of increasing CO_2 concentration in Ar - CO_2 shielding gas blends on droplet formation. Tests have a measured droplet temperature of ∼2500 °C (4532 °F) and average current of 241A. High speed video shows the tail length in the pure Ar test is higher representing easier droplet detachment.

Thermal efficiency and heat distribution measurements were performed using 5% CO_2 - 95% Ar shielding gas as shown in Table 2.2 and Figure 2.6. Average overall thermal efficiency was 69.7 ± 3.7% and ranged between 60-78%. The remaining energy was lost due to vaporization, thermal radiation, and missed droplets. The thermal efficiency is broken up with approximately $\frac{2}{3}$ and $\frac{1}{3}$ of the energy being distributed to the cathode and the anode respectively. Efficiency was found to be the highest in the transition zone with similar efficiencies in globular and spray metal transfer mode.

Table 2.2: Summary of efficiency and heat distribution in 5% CO_2 - 95% Ar shielding gas experimentation. Values displayed are total heat input percentages and are an average of several tests (Note: values do not add up to exactly 100% due to test averaging).

Metal transfer mode	Thermal efficiency (%)	Cathode (%)	Anode (%)	Losses (%)
Overall	69.7 ± 3.7	47.2 ± 3.5	21.9 ± 1.0	30.3 ± 3.7
Globular	68.1 ± 3.8	47.4 ± 3.8	21.2 ± 1.0	31.9 ± 3.8
Transition	72.3 ± 3.9	50.7 ± 3.7	21.0 ± 0.9	27.7 ± 3.9
Spray	69.2 ± 3.6	45.8 ± 3.6	22.4 ± 1.0	30.8 ± 3.6

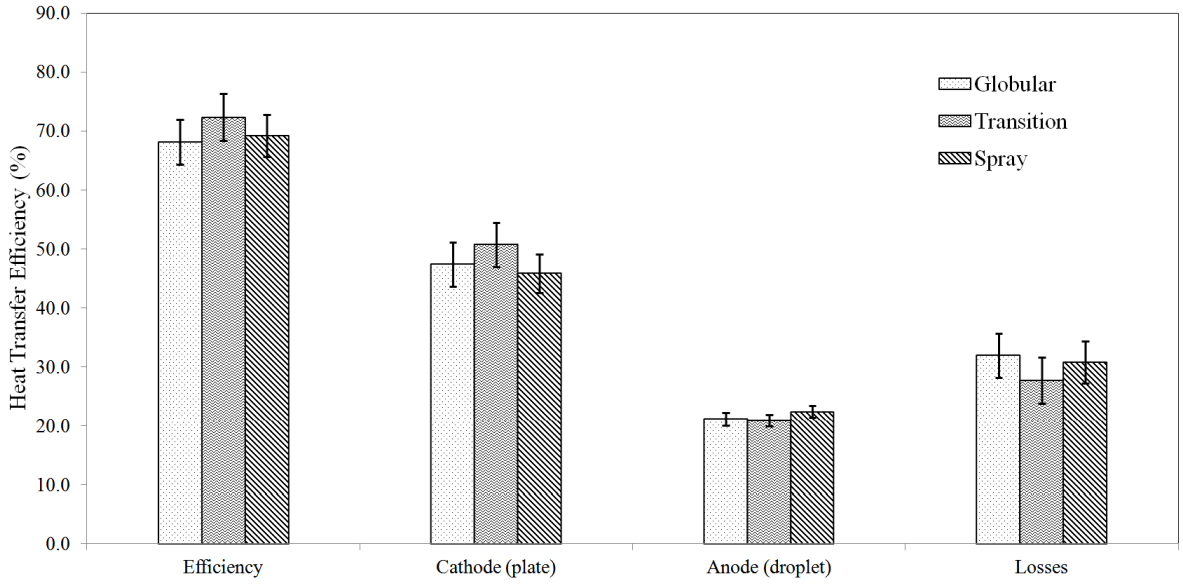

Fig. 2.6: Thermal efficiency and energy partition in the 5% CO_2 - 95% Ar shielding gas tests. (Note: values do not add up to exactly 100% due to test averaging)

2.4. Discussion

The results using pure Ar are in good agreement with recent work who measured droplet temperature between ~1900 °C - 2600 °C (3452 °F - 4712 °F) as shown in Table 2.1 and Figure 2.3 [40–44, 47]. A transition current of 206 A gave a minimum in droplet temperature of 2254 °C (4089.2 °F) and is in good agreement with findings by Soderstrom and Scott who observed the minimum at 205 A [2, 3, 45].

It is currently unknown if the minimum droplet temperature found is the actual minimum droplet temperature. As shown in Figure 2.3, Soderstrom found a minimum droplet temperature at significantly lower temperatures than that found in this paper [3]. Several attempts were made to find a droplet temperature minimum but obtaining data at an exact current was

difficult. Current could not be directly controlled as all welds were performed in constant voltage mode. The resolution of the wire feed speed was not sufficient enough to give the desired current near the minimum droplet temperature. High speed videography shows that the electrode extension is not constant during welding and can vary from the desired 12.5 mm (0.49 in.). Variations in electrode extension will change the current output during welding making repeatability difficult. Multiple experiments with identical welding parameters often resulted in slightly different results.

The calorimeter was placed 127 mm (5 in.) below the water cooled cathode to ensure that radiative heat was not a factor in measuring droplet temperature [3, 34]. Droplets would fall approximately 139.7 mm (5.5 in.). Literature has used various distances ranging from 70 mm to 300 mm (2.75 in. to 11.8 in.) [35, 36]. It is currently unknown if the distance from the electrode tip to the calorimeter is altering droplet temperature measurements due to heating from the plasma or cooling from atmospheric gases. The similarity in droplet temperature measurements utilizing different techniques such as pyrometry indicates that this distance is not influencing measurements but has yet to be fully determined [41–43, 47].

With Ar - CO_2 blends the transition current increases with higher concentrations of CO_2 and is most likely due to the different thermophysical properties of the CO_2 plasma [41, 48, 51–53]. At higher concentrations of CO_2 the arc becomes more constricted resulting in a higher energy density due to the increased current density, and increased Lorentz forces on the arc [53, 54]. A constricted arc leads to a decreased anode spot size which hinders droplet detachment and results in more thermal energy being distributed to the cathode [53]. The constricted arc described is seen in Figure 2.5 between pure Ar and 5% CO_2 - 95% Ar. Literature has similar findings showing that higher concentrations of CO_2 in Ar - CO_2 blends pushes the transition zone to higher currents [23, 48, 52]. The transition zone defined in this paper is the area of local minimum droplet temperature between globular and spray metal transfer. The transition zone is typically defined as the area where the droplet diameter is smaller than the electrode diameter [23, 48, 52]. Frequently, the transition zone is not well defined and can be a gradual change from globular to spray transfer over a wide range of currents [23].

As shown in Figure 2.7, higher concentrations of CO_2 in Ar - CO_2 blends pushes the droplet temperature curve to higher currents but does not appear to significantly shift the droplet

temperature curve to different temperatures. When at equivalent metal transfer modes between the three shielding gases, similar droplet temperatures can be found. In Figure 2.7 the top and bottom row of photos shows spray and transition metal transfer modes respectively between all three shielding gases tested. The photos in Figure 2.7 show that similar metal transfer modes and droplet temperatures are achieved despite different average currents. Droplet diameters of these tests were calculated based on volumetric welding rates and frequency of detachment seen in the high speed video. The results of the droplet diameter are summarized in Table 2.3. Determining the frequency of detachment proved challenging in parts of the 10% CO_2 - 90% Ar videos due to frequent explosions of the droplets as a result of the reactive CO_2. This inaccuracies in measurements may account for the larger droplet diameter in spray transfer in the 10% CO_2 - 90% Ar test. The results of Figure 2.7 and Table 2.3 indicates that at the same metal transfer mode, droplet temperature will not change significantly with increasing CO_2 in Ar - CO_2 blends. This suggests that with a small change in CO_2 concentration, droplet temperature can decrease while still maintaining a similar deposition rate.

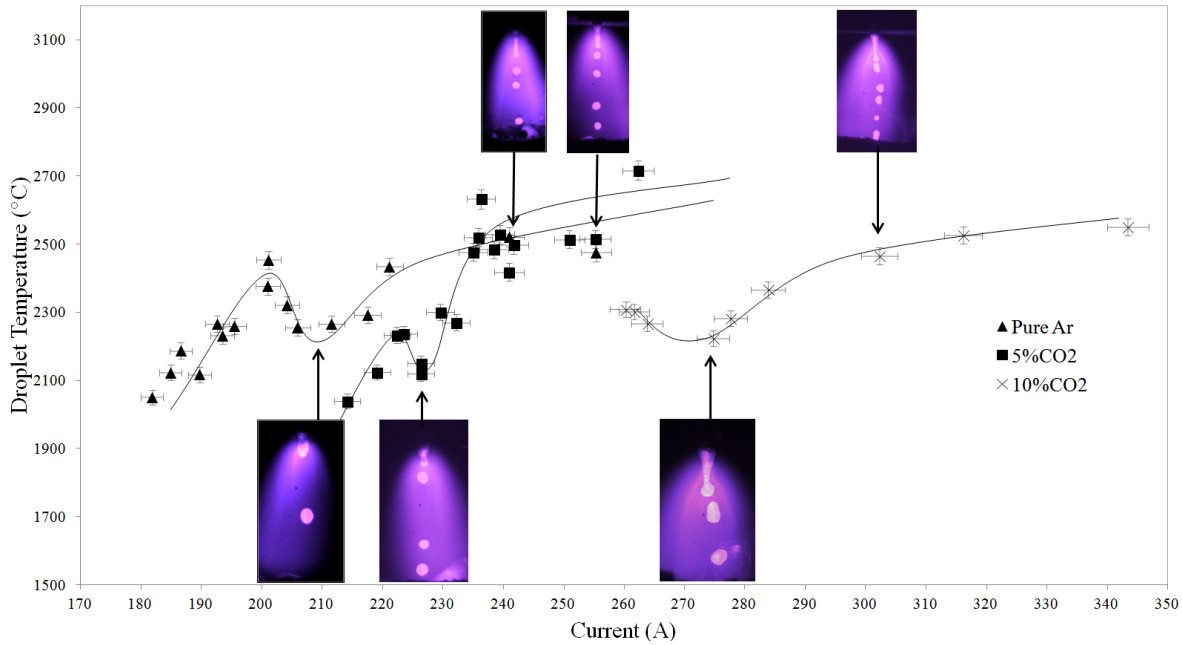

Fig. 2.7: Effect of Ar - CO_2 shielding gas blends on metal transfer using a 0.045 in. (1.143 mm) ER70S-6 carbon steel wire. The top row of photos shows spray metal transfer and the bottom row shows transition metal transfer for each shielding gas tested.

Experimentation was not performed with CO_2 concentrations higher than 10% due to spatter arising from repelled like metal transfer. Testing with 15% CO_2 - 85% Ar was performed and droplets were found to touch the cathode before falling onto the calorimeter. This invalided

Table 2.3: Droplet diameter measurements for the six tests highlighted in Figure 2.7.

Shielding gas	Droplet Diameter (mm) Transition	Spray
Pure Ar	0.874	0.754
5% CO_2 - 95% Ar	0.912	0.774
10% CO_2 - 90% Ar	0.921	0.837

all droplet temperature, efficiency, and heat distribution readings. Re-evaluation of the experimental setup is needed before further experimentation can commence at CO_2 concentrations higher than 10%.

As shown in Table 2.2, average overall efficiency with 5% CO_2 - 95% Ar shielding gas was found to be 69.7 ± 3.7% and within the reported range of 68-88% [3, 44, 55–59]. No apparent trend was found between efficiencies of different metal transfer modes. The average heat input for the cathode and anode was 46.9 ± 3.5% and 21.9 ± 1.0% of the total heat and was close to the reported range of 50-65% and 20-30% respectively [3, 44, 55]. Experimental calculations were performed using only the heat input in the cathode and captured droplets. Droplets occasionally missed the calorimeter due to spatter resulting in a lower efficiency and slightly skewed heat distribution. Additionally, less thermal radiation was captured by the system than a typical bead on plate due to the smaller surface area of the cathode. Experimental efficiency would be higher if these factors had been captured by the system.

2.5. Conclusions

A solid state calorimeter and a water cooled cathode were used to measure droplet temperature in free-flight metal transfer GMAW using three different shielding gases as shown in Table 2.1 and Figure 2.4. Droplet temperature measurements ranged between 2000 °C - 2700 °C (3632 °F - 4892 °F) depending on welding parameters and shielding gas selection. Results using pure Ar shielding gas are comparable with literature showing a minimum droplet temperature of 2200 °C (3992 °F) at the transition current between globular and spray metal transfer modes. It is currently unknown if the found minimum is the lowest possible temperature due to resolution in the welding current. A similar minimum in droplet temperature was found at 206 A, 230 A, and 270 A for pure Ar, 5% CO_2 - 95% Ar, and 10% CO_2 - 90% Ar shielding gas tests respectively. Testing with CO_2 concentrations higher than 10% was not performed due to a large quantity

of droplets landing on the cathode invalidating results.

As shown in Table 2.2 and Figure 2.6, average thermal efficiency was 69.7 ± 3.7% utilizing 5% CO_2 - 95% Ar shielding gas with 47.2 ± 3.5% and 21.89 ± 1.0% of the heat being distributed to the cathode and anode respectively. No apparent trend was found between different metal transfer modes in regards to thermal efficiency or heat distribution. Efficiency was within previous reported ranges but on the low end possibly due to missed droplets as spatter and not capturing some radiative energy in the cathode typically seen when welding plates.

Increasing concentrations of CO_2 in Ar - CO_2 blends increases the transition current between globular and spray metal transfer modes. Comparing different Ar - CO_2 blends at the same metal transfer mode indicates that CO_2 has no significant effect on droplet temperature as shown in Figure 2.7. Results show that modifying small amounts of CO_2 in the shielding gas can lower droplet temperature while still maintaining a similar deposition rate.

3. Experimental Measurements of Fall Voltages in Gas Metal Arc Welding

3.1. Introduction

The determination of fall voltages associated with welding arcs has been a great interest for researchers as these values lead to greater insight and comprehension of arc welding, including the effects of reversed/variable polarity. Numerous studies have measured or developed models relating plasmas and their respective fall voltages with results varying drastically between literature. Most research has explored looking at arc discharges between two pure metal electrodes (copper, tungsten, and graphite) with different types of plasmas (air, argon, or CO_2) [16, 60–65]. In relation to a welding system, this type of research is most similar to Gas Tungsten Arc Welding (GTAW) which involves a non-consumable thermionic tungsten cathode, non-thermionic anode, and inert plasma/shielding gas. Knowing the magnitude of fall voltages in GTAW aids in understanding electrode wear and heat inputs typically seen in welding systems.

Despite the extensive work performed in the GTAW system, substantially less research has been made in the determination of fall voltages associated with Gas Metal Arc Welding (GMAW) [66]. The addition of a non-thermionic cathode in conjunction with a continuously feeding melting anode has led to increased challenges in experimentation [18]. Understanding arc phenomenon in GMAW has often proved challenging due to unpredictable and unstable behaviour of the welding system during metal transfer. Models have been developed to assist in the comprehension of GMAW with many models related to metal transfer, droplet temperature, fume generation, efficiency, and heat distribution [3, 16, 18, 19, 25, 27]. These models often require a measurement of fall voltage and are frequently approximated with measurements found in GTAW due to their similarity [62, 67]. This similarity has led to reasonable approximations but is not necessarily accurate as the addition of a consumable anode, non-thermionic cathode, and different plasma/shielding gas composition in GMAW will lead to altering arc column properties and different fall voltages [16–18, 25, 27, 62, 68].

This paper explains how measurements of voltage loss, thermal efficiency, droplet temperature, and droplet diameter were experimentally obtained with possible explanations for the results. The measurement of the various fall voltage regions was either directly measured or inferred

based on experimental parameters and measurements. This is the first time all fall voltage regions have been simultaneously measured as a function of current. This was undertaken to get a complete understanding of the GMAW system for various welding parameters in a consistent manner. Experimental decisions and parameters were selected primarily for their relation to typical welding systems allowing greater insight into the GMAW system.

3.2. Background

When an electric discharge is present between two metallic electrodes, there is a large voltage loss associated very close to both the cathode and anode [16, 17]. The rapid reduction in temperature between the plasma and electrode surface results in insufficient thermal ionization and ion generation for proper electrical conductivity close to the anode/cathode [62]. A large potential is generated in these regions known as fall voltage regions or drop potential regions. These regions are in the order of 1-100 μm in thickness [16, 18, 53, 66, 69].

Earliest measurements of cathode and anode fall voltages began with Stark who utilized a probe allowing electron temperature measurements very close to a cathode or anode in a plasma [70]. These temperature measurements allowed for derivation of current density and overall fall voltage measurements. Stark's probe was greatly improved by Langmuir through the creation of the Langmuir probe allowing more accurate measurements [71, 72]. These probes were a fundamental basis for understanding plasmas as electron temperature, current density, and fall voltage could be determined. Further experiments were conducted utilizing Langmuir's probe in different types of plasmas and electrodes [73–76]. Results varied as cathode fall measurements obtained were between 5-15 V. These early experiments were conducted to gain further understand of plasmas and were not directly related to welding systems.

In relation to a typical welding system, the fall voltage regions are the primary contributing factor for heat inputs in both the cathode and anode [62]. With sufficient pressure, voltage, and current (typical of those found in a welding system) large heat inputs are obtained leading to subsequent melting of the cathode and anode. This is the fundamental basis for a successful welding system. In addition to the cathode and anode fall voltage, a typical welding system also has voltage loss associated with the contact tip, electrode, and arc column as shown in Figure 3.1.

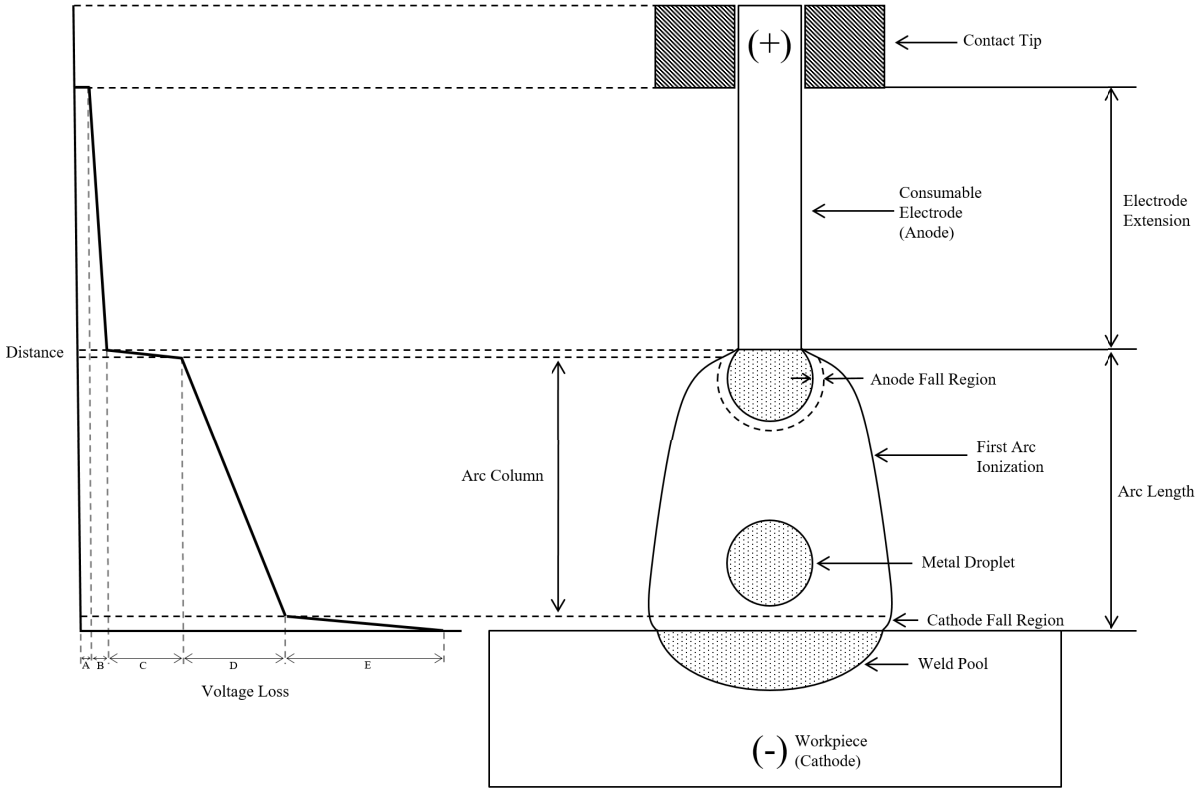

Fig. 3.1: Typical GMAW system and fall voltage regions. A: Contact tip voltage loss. B: Electrode extension voltage loss. C: Overall anode fall voltage. D: Overall arc column fall voltage. E: Overall cathode fall voltage.

Various systems have been utilized to determine fall voltages in GTAW such as probe sweeping, energy balance, and Langmuir's probe [65]. However, the addition of a consumable anode has led to increased difficulty in voltage potential measurements in GMAW. Other methods have been used to determine fall voltages for a GMAW system typically in the form of calorimeters, models, or arc analysis [16, 18, 61–66, 77–79]. Some methods are outlined below showing how voltage fall measurements were made at various regions in GMAW.

3.2.1. Cathode

The cathode fall region is the negative area of the GMAW system. To maintain a stable arc, multiple small cathode spots are created to generate a sufficient number of electrons. The cathode fall region in non-thermionic materials is less understood compared to thermionic materials. In thermionic cathodes, electrons are generated when the material reaches the thermal electron emission temperature [17]. These electrons are accelerated away from the cathode and ionize neutral atoms. These ions are then accelerated towards the cathode providing the cathode with heat from the ions kinetic and potential energy [80].

In non-thermionic materials, electron generation may be a result of oxide dissociation or reactions as cathode attachment spots are preferentially located at oxides [17]. Experiments have shown that a material free of any oxide material cannot sustain a stable arc [17]. Industrial welding systems will have the addition of O_2 or CO_2 in the shielding/plasma gas to avoid unstable arcing behaviour. The CO_2 addition generates an oxide layer in the weld pool which reduces the cathode work function and promotes increased stability [53]. Additionally, the higher arc plasma temperature, higher thermal conductivity of CO_2, and the reactions between the CO_2 and molten weld pool all contribute to more heat being contributed to the weld pool [53].

Literature has placed the overall cathode fall voltage in GMAW to be somewhere between 10-20 V [16, 66, 79, 81]. Lancaster estimated the overall cathode fall voltage to be approximately 10-20 V and estimated the overall cathode fall voltage to be approximately 15 V for a welding current of 118 A [16]. Jonsson theoretically derived the sum of the overall cathode and anode fall voltages to range between 13.32-14.93 V. At the time, Jonsson believed that the anode sheath voltage was very small or negative possibly due to the work of Pfender [66, 77]. Hajossy determined the overall cathode fall voltage of a GMAW system in different shielding gases by comparing the heat input, melting rate, and instantaneous resistance during short-circuit in direct current electrode negative (DCEN) [79]. The calculation used by Hajossy did not appear to consider overheating at the electrode surface. Utilizing Ar, CO_2, and air shielding gases, Hajossy found the overall cathode fall voltage of the GMAW system to be 13.9, 14.5, and 16.4 V respectively [79]. Huismann calculated deposition rates in DCEN with a cathode fall voltage of 11 V and found similar deposition rates as those from empirical values [82].

3.2.2. Anode

The anode fall region is the positive area which attracts electrons. Electrons transfer their kinetic and thermal energy to the anode during condensation result in heating of the anode [18]. Anode fall voltage is often calculated using an energy balance around the GMAW electrode as shown below [16, 18, 19, 78]:

$$(1+m)q = (\phi_{an} + \frac{3kT}{2e} + V_A)I \tag{3.1}$$

Where q is the overall energy transferred to the electrode from the arc, m is the portion of the

anode heat lost by radiation, ϕ_{an} is the work function of the anode material, k is Boltzmann's constant, T is the temperature of the electrons, e is electron charge, V_A is the anode sheath voltage, and I is the current [16]. Typical values of m are smaller than 1% [16]. $\frac{3kT}{2e}$ describes the thermal energy of electrons. Almost all literature reports the overall anode fall voltage as shown below:

$$V_{an} = \frac{q_{an}}{I} - V_{elec} - V_{cont} = \phi_{an} + \frac{3kT}{2e} + V_A \tag{3.2}$$

Where V_{an} is the overall anode fall voltage, q_{an} is the total anode heat input, V_{elec} is the electrode voltage loss, and V_{cont} is the contact tip voltage loss. This equation assumes m is negligible. The value of V_{an} typically varies from 4-9 V depending on welding parameters [18, 66, 77–79]. Lancaster has reported that the value of overall anode fall voltage may vary as much as 1-12 V but is calculated to be approximately 5.5 V [16]. Lancaster stated that the overall anode fall voltage does not vary with arc current below a critical value. Above this critical value, it is stated that the overall anode fall voltage will decrease [16]. In contrast, Nemchinsky calculated overall anode fall for aluminum and steel in GMAW and compared it with experimental values obtained by Waszink [18, 78]. Both Nemchinsky and Waszink found that the overall anode fall voltage increased with increasing current. Nemchinsky derived the overall anode fall voltage to be 8-9 V between 200-300 A while Waszink's experiments found the overall anode fall voltage to be 7-7.5 V between 200-300 A [18, 83]. Huismann calculated deposition rates in DCEP with an anode fall voltage of 5.5 V and found similar deposition rates as those determined with empirical findings [82]. Hajossy determined the overall anode fall voltage of a GMAW system in different shielding gases by comparing the overall heat input, deposition rate, and instantaneous resistance during short-circuit in direct current electrode positive (DCEP). Hajossy found that the overall anode fall voltage was 7.0 V in an argon arc and 4.9 V in a CO_2 arc [79].

3.2.3. Contact Tip

There is a voltage loss associated between the contact tip of the welding torch and the consumable electrode from the electrical contact resistance between the surfaces. This voltage loss will contribute to heating of the welding torch and electrode. A typical GMAW system will have

a constant contact resistance between the contact tip and consumable electrode when metal transfer is stable [84]. Literature has found the contact tip voltage drop by measuring the voltage difference between the contact tip and a tungsten probe pressed up against the moving electrode directly after leaving the contact tip [66, 83, 85]. This method was used by Waszink who measured a voltage drop of 0.1-0.3 V for currents of 100-250 A in a 1.2 mm (3/64 in.) diameter coppered steel electrode [83]. Jonsson found a slightly higher value of 1.3-1.7 V for currents of 200-325 A [66]. By extrapolation of Wilson's results, a contact tip drop of approximately 0.3-0.6 V was found for a current of 1200 A in Submerged Arc Welding (SAW) [85]. Luijendijk used a different approach to calculate contact tip voltage loss by measuring contact area and contact force of different wires [84]. Luijendijk's calculations found an average voltage loss of 0.5 V for a welding current of 250 A [84].

3.2.4. Electrode Extension

With current flowing through the consumable electrode in GMAW, ohmic heating must be considered. The wire will have an associated voltage loss resulting in joule heating proportional to the electrode extension. Many models have been developed to understand the effects of resistive heating in GMAW [7, 67, 78, 83, 85–87]. The potential of ohmic heating will vary depending on wire composition and many of these models attempt to be applicable to a wide range of materials.

Lehnhoff performed a comprehensive scaling analysis regarding heat transfer to calculate the rate of conduction and joule heating in a typical GMAW scenario from first principles [7]. The analysis took into consideration the non-linearity and changing resistivity properties for multiple materials. With the difficulty in measuring resistive heating in a GMAW system, this model will be used in this paper to determine the extent of voltage loss in the electrode extension [7]. Resistivity properties of the tested wire were utilized in this model [8].

Waszink derived the electrode extension fall potential to be approximately 2.5 V for an electrode extension of 10 mm in a 1.2 mm (0.063 in.) diameter mild steel wire [78]. Halmoy also derived the electrode extension voltage loss to be approximately 1-5 V for currents between 150-350 A in a 1.2 mm (0.047 in.) diameter steel electrode [39, 87]. Wilson experimentally found the voltage drop in the electrode extension at various distances in carbon steel in SAW [85]. Wilson's results showed that voltage drop increased with increasing electrode extension and was dependent on

wire diameter. Electrode extension voltage drop was between approximately 0.5-3.0 V for an electrode extension of 1-7 in. (25.4-177.8 mm) in a 0.3125 in. (7.94 mm) diameter electrode using SAW [85].

3.2.5. Arc Column

The plasma column is the region between the cathode and anode fall regions. This region is seen as the current carrying section of the arc and reaches temperatures of approximately 5,000-25,000 K (8,540-44,540 °F) [16, 17, 25–27]. These high temperatures result in large radiative energy losses in the arc column [18]. This heat loss is balanced by resistive heating in the arc to maintain the proper temperature and ionization. The continuous nature of the arc column has led researchers to approximate this region with a linear voltage drop as a function of arc length [16–18].

The arc column is often seen as being very similar in GTAW and GMAW as similar plasma/shielding gases are used [18]. The primary difference is the metallic vaporization associated with GMAW. The addition of a consumable anode increases metal vapors in the plasma leading to a change in the plasma's temperature, pressure, and composition [19, 62]. Typical GTAW plasma temperatures are approximately 15,000-25,000 K (17,540-44,540 °F) with GMAW plasma temperature being cooler at 5,000-15,000 K (8,540-26,540 °F) [16, 25–27]. This will change overall conductivity properties and arcing behaviour in the plasma making comparisons between GTAW and GMAW difficult.

Halmoy predicted the arc column voltage in GMAW by welding at a constant current and wire feed speed, changing the contact tip to work distance, and then measuring the change in arc length and electrode extension. Halmoy's findings showed that the arc fall voltage was a function of arc length. Above 200 A, the electric field in the arc column had a drop potential of 0.6 V/mm [87]. For a welding current of 200 A and arc length of 0, Halmoy measured the total voltage drop to be approximately 19 V [87]. With a zero arc length, this total voltage drop is the cumulative overall cathode and anode fall voltage.

3.3. Experimental Setup

The experimental setup is identical to that used by Scott and Chapuis as seen in Figure 3.2 [1, 2, 4]. The setup is broken up into several different components including a solid state

calorimeter, water cooled copper cathode, custom contact tip, and synchronized high speed videography with data acquisition. Cathode and anode heat inputs are measured independently. The experimental setup is limited to free-flight metal transfer modes with no capability of performing short-circuit waveforms.

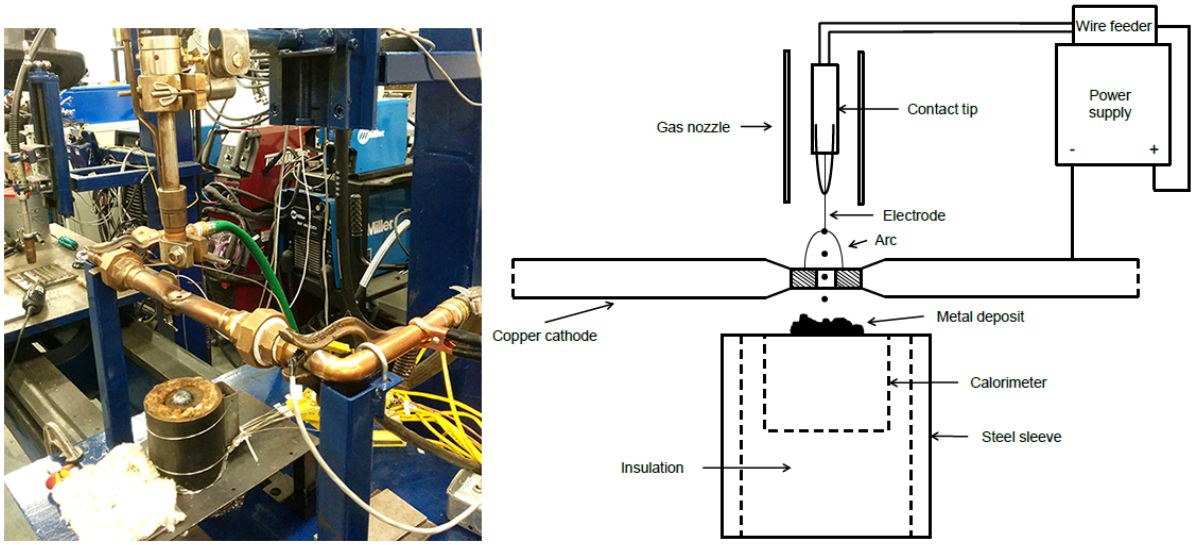

Fig. 3.2: Diagram showing the experimental setup of the solid state calorimeter and copper cathode (not to scale) [1, 2].

3.3.1. Welding Equipment

Welding was performed with a Lincoln Power Wave S500 and a Lincoln 84 Dual Feeder (program 5 weld set reference: Z153615). All welds were done in constant voltage (CV) mode in direct current electrode positive polarity (DCEP). A Tregaskiss Tough Gun I.C.E. water-cooled robotic MIG torch was used with a 0.045 in. (1.143 mm) diameter ER70S-6 carbon steel electrode. Shielding gas was mixed to 35 standard cubic feet per hour (16.52 l/min) using an OMEGA FL-6GP-40ST-40ST-40ST gas proportioning rotameter. 100% Ar and 95% Ar - 5% CO_2 shielding gas blends were used for experimentation.

3.3.2. Copper Cathode

The purpose of the water cooled copper cathode was to maintain an arc during experimentation. The copper cathode was designed to allow passage of liquid droplets from the electrode to the calorimeter as shown in Figure 3.2. Water is capable of flowing through the copper cathode without interference. Water flow rate was monitored with a Kings 7520 7C-02 flow meter with

typical flow rates of 0.33 ± 0.02 USGPM (1.25 ± 0.076 l/min). Omega GKQSS-18G-12 K type thermocouples were used to measure the inlet and outlet temperature of the water with an accuracy of ±0.4%. Temperature differences in the water inlet and outlet reached steady state after approximately 20 seconds with outlet water temperatures reaching ∼75 °C (167 °F). Welding was maintained for approximately 30 seconds to ensure steady state was reached. Overall cathode fall voltage and heat input were determined using:

$$V_{cat} = \frac{q_{cat}}{I} = \frac{(T_{out} - T_{in})\dot{m}C_w}{I} \tag{3.3}$$

Where V_{cat} is the overall cathode fall voltage, q_{cat} is the total cathode heat input, T_{out} is outlet temperature, T_{in} is the inlet temperature, $\dot{m}$ is the water mass flow rate, C_{w} is the specific heat capacity of water, and I is the current [88].

3.3.3. Calorimeter and Anode

A solid state high-purity copper calorimeter was used to measure anode heat input. Calorimeter dimensions were: height of 35 mm (1.38 in.), diameter of 50.8 mm (2 in.), and positioned 127 mm (5 in.) below the water cooled copper cathode. A solid state calorimeter was more desired than a water based calorimeters as there is no error associated with water evaporation [2]. 10 Omega GKQSS-18G-12 K type thermocouples were used to measure the temperature change of the calorimeter. Droplets that fell onto the calorimeter were weighed using an Adam PGW 4502e scale to an accuracy of ± 0.01 g (0.0022 lbs). Properties of pure copper and pure iron were used for the calorimeter and wire respectively when determining anode heat input and droplet temperature [50, 89]. Molten tin calibration tests have shown that the accuracy of the enthalpy measurements varied by ± 1.1% when the final calorimeter temperature was kept below 187 °C (368.6 °F). Overall anode fall voltage was then determined using equation 3.2.

3.3.4. Electrode Extension

A known electrode extension allows for proper calculation of resistive heating into the wire electrode. Normal industrial contact tips can have a small variance in the measured electrode extension distance as it is unclear where the last point of contact is [2, 84]. A custom contact tip was used which ensured a known contact point as shown in Figure 3.3 [2]. A tungsten indicator

was set to the desired electrode extension distance as shown in Figure 3.3. Voltage settings were adjusted during welding until the desired electrode extension was visually verified using the tungsten indicator and high speed camera. Current was controlled by varying Wire Feed Speed (WFS) with a resolution of 1 inch/min (0.0254 m/min). Voltage settings changed with WFS and were selected to maintain a consistent arc length between experiments. All tests done in this research had an electrode extension of approximately 12.5 mm (0.5 in.) and arc length of approximately 12.5 mm (0.5 in.).

A known electrode extension allows for easier repetition and is used to calculate the resistance and voltage loss with a scaling analysis produced by Lehnhoff and Mendez [7]. The voltage drop in the electrode extension can be determined using an energy balance:

$$V_{elec} I = H_{c_2} U A \tag{3.4}$$

Where H_{c_2} is the amount of joule heating gained by the electrode, U is the WFS, and A is the cross sectional area of the wire. Following Lehnhoff, H_{c_2} can be calculated as [7]:

$$H_{c_2} = H_c \widehat{H_{c_2}^{+*}} \tag{3.5}$$

Where H_c is the enthalpy variation between room temperature and just before melting of the electrode. $\widehat{H_{c_2}^{+*}}$ can be determined as:

$$\widehat{H_{c_2}^{+*}} = 2\left[\frac{e^{\frac{d}{M_1}} - 1}{b\left(1 - e^{\frac{d}{M_1}}\right) + d\left(1 + e^{\frac{d}{M_1}}\right)}\right] \tag{3.6}$$

$$M_1 = \frac{U H_c A^2}{L \rho_0 I^2}, \quad d = \sqrt{b^2 - 4a}, \quad b = \frac{\Delta\rho_1}{\rho_0} + 4\frac{\Delta\rho_2}{\rho_0}, \quad a = -4\frac{\Delta\rho_2}{\rho_0} \tag{3.7}$$

Where ρ is the electrical resistivity, $\Delta\rho_0$ is the maximum change in ρ from H_0 to H_m, $\Delta\rho_1$ is the change in ρ, $\Delta\rho_2$ is the relative curvature in $\rho(H)$, H is the enthalpy in the wire material, and L is the electrode stickout [7]. Resistivity properties of ER70S-6 were obtained and used for calculations as shown in Table 3.1 [8].

Table 3.1: Material parameters for ER70S-6 and experimental values used to determine electrode extension voltage loss [7, 8].

ρ_0x10^7 (Ωm)	ρx10^7 (Ωm)	$\Delta\rho_1$x10^7 (Ωm)	$\Delta\rho_2$x10^7 (Ωm)	T_m (K)	H_cx10^{-9} (Jm^{-3})	Ax10^6 (m^2)	Lx10^3 (m)
3.30	11.7	11.7	3.30	1740	7.33	1.03	12.5

3.3.5. Contact Tip

Contact voltage loss from the resistance at the contact tip and electrode was measured directly. A second tungsten bar maintained sliding contact with the steel electrode immediately after leaving the contact tip as shown in Figure 3.3. A torsional spring was attached to a tungsten electrode to ensure constant contact with the steel electrode. This approach is similar to the technique used by Wilson and Waszink [83, 85].

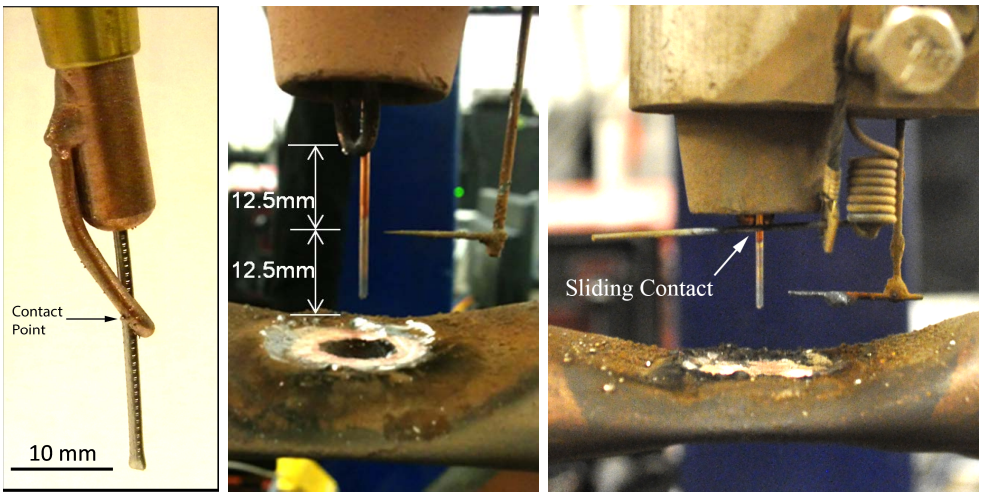

Fig. 3.3: Custom contact tip used during experimentation [2]. Left: Typical custom contact tip used in all experimentation. Centre: Tungsten bar referencing electrode extension shown in high speed videography. Right: Tungsten bar measuring contact tip voltage loss.

3.3.6. High Speed Videography

High speed video taken at 5000 frames per second was used to confirm that the desired metal transfer mode and electrode extension was achieved. A Phantom V210 high speed camera was utilized with a 850 nm long wave pass filter. Data acquisition was captured in synchronization with the high speed videography to determine welding parameters. A LEM LV 25-P voltage transducer and LEM HTA 600-S current transducer were used to capture total voltage and current with an accuracy of $\pm 0.9\%$ and $\pm 1.0\%$ respectively. Total voltage measurements were

performed between the welding torch and cathode. Voltage loss through the welding torch cable were not included in measurements. Analog signals from the transducers were captured with a National Instruments USB 6351 X series data acquisition unit at 50,000 Hz. The frequency of detachment was measured by counting 100 droplet detachments in its respective time frame for each test. Droplet diameter was determined through a volumetric balance by using the follow formula:

$$d_d = \left(\frac{3U(d_w)^2}{2f_d} \right)^{\frac{1}{3}} \tag{3.8}$$

Where d_{d} is the droplet diameter, d_{w} is the wire diameter, and f_{d} is the frequency of detachment.

3.3.7. Arc Column

The combination of the water cooled cathode, calorimeter, and data acquisition system were used to calculate voltage loss of the arc column. Arc column voltage loss was determined using:

$$V_{col} = V_{tot} - V_{cat} - V_{an} - V_{elec} - V_{cont} \tag{3.9}$$

Where V_{col} is the arc column voltage loss, and V_{tot} is the total welding voltage.

3.4. Results

Results are summarized in Table 3.2-3.3 and Figures 3.4-3.7. All average values presented are given with their standard deviation.

Table 3.2: Experimental measurements found for a 1.143 mm (0.045 in.) diameter ER70S-6 carbon steel electrode with an electrode extension of approximately 12.5 mm (0.5 in.) and arc length of 12.5 mm (0.5 in.).

Shielding Gas	Average Voltage (V)	Average Current (A)	Wire Feed Speed (inch/min)	Frequency of Droplet Detachment (Hz)	Droplet Diameter (mm)	Thermal Efficiency (%)	Droplet Temperature (K)	Cathode Fall Voltage (V)	Anode Fall Voltage (V)	Contact Tip Fall Voltage (V)	Electrode Extension Fall Voltage (V)	Arc Column Fall Voltage (V)
100% Ar	28.1	185.2	240	49	1.59	76.6	2448	13.98	5.66	0.40	1.50	6.59
100% Ar	28.1	192.3	240	77	1.37	72.0	2595	12.41	5.77	0.42	1.63	7.85
100% Ar	27.1	193.5	224	46	1.59	64.7	2504	10.49	4.89	0.42	1.73	9.58
100% Ar	28.1	200.6	242	74	1.39	69.9	2548	12.16	5.23	0.43	1.79	8.46
100% Ar	28.0	201.0	229	52	1.54	73.5	2650	13.27	4.99	0.43	1.87	7.42
100% Ar	29.9	207.5	230	159	1.06	66.7	2600	12.95	4.56	0.45	2.01	9.96
100% Ar	30.2	214.0	240	140	1.12	63.4	2634	11.97	4.63	0.46	2.10	11.06
100% Ar	30.2	223.9	250	277	0.91	68.6	2523	13.91	4.06	0.48	2.27	9.50
100% Ar	29.6	225.4	260	271	0.93	66.2	2631	12.17	4.71	0.49	2.25	10.02
100% Ar	30.3	227.2	260	290	0.91	66.4	2652	12.74	4.60	0.49	2.29	10.16
100% Ar	30.2	236.8	270	430	0.80	68.1	2714	13.02	4.56	0.51	2.46	9.61
100% Ar	30.6	247.3	280	434	0.81	66.5	2706	12.95	4.22	0.53	2.66	10.24
100% Ar	31.8	256.8	290	477	0.80	64.2	2755	12.86	4.18	0.56	2.84	11.40
100% Ar	32.2	266.2	300	511	0.79	63.7	2655	13.27	3.65	0.58	3.01	11.67
95% Ar - 5% CO2	32.5	214.1	245	128	1.17	62.3	2312	13.90	3.84	0.46	2.02	12.22
95% Ar - 5% CO2	32.1	219.1	265	159	1.11	78.0	2397	18.13	4.42	0.47	2.02	7.08
95% Ar - 5% CO2	32.9	222.4	255	126	1.19	64.0	2506	14.23	4.20	0.48	2.15	11.84
95% Ar - 5% CO2	32.0	223.5	267	257	0.95	76.1	2509	17.12	4.63	0.48	2.10	7.65
95% Ar - 5% CO2	32.1	226.3	265	286	0.92	76.0	2393	17.69	4.03	0.49	2.18	7.71
95% Ar - 5% CO2	32.3	226.3	265	259	0.95	70.8	2423	16.14	4.08	0.49	2.18	9.45
95% Ar - 5% CO2	32.7	229.5	265	236	0.98	66.5	2573	14.59	4.40	0.50	2.25	10.97
95% Ar - 5% CO2	33.8	232.2	255	259	0.93	60.4	2542	13.69	3.83	0.50	2.38	13.39
95% Ar - 5% CO2	32.6	235.0	265	378	0.83	69.1	2749	14.94	4.67	0.51	2.38	10.07
95% Ar - 5% CO2	32.5	235.8	270	421	0.81	71.2	2793	15.50	4.79	0.51	2.37	9.36
95% Ar - 5% CO2	32.8	236.3	275	397	0.83	73.8	2905	15.94	5.37	0.51	2.35	8.58
95% Ar - 5% CO2	32.5	238.4	270	435	0.80	74.7	2757	16.62	4.71	0.52	2.43	8.24
95% Ar - 5% CO2	32.6	239.4	270	439	0.80	68.3	2801	14.60	4.71	0.52	2.46	10.35
95% Ar - 5% CO2	32.8	240.9	275	466	0.79	68.0	2691	14.85	4.47	0.52	2.46	10.47
95% Ar - 5% CO2	32.9	241.6	275	471	0.79	64.5	2771	13.55	4.67	0.52	2.48	11.66
95% Ar - 5% CO2	33.3	250.9	295	458	0.81	70.9	2786	15.79	4.70	0.54	2.58	9.70
95% Ar - 5% CO2	33.9	255.1	305	546	0.77	69.1	2788	15.41	4.81	0.55	2.63	10.46
95% Ar - 5% CO2	34.4	262.3	315	655	0.74	71.4	2989	15.97	5.30	0.57	2.75	9.83

Table 3.3: Average fall voltage and standard deviation as shown in Figures 3.4 and 3.5. Current ranged between 185-266 A. Some values were found to change with current. For a complete table of experimental results see Table 3.2.

Voltage Loss Area	Symbol	Average Fall Voltage (V)	
		100% Ar	95% Ar - 5% CO2
Average Voltage	V_{tot}	29.6 ± 1.5	32.8 ± 0.6
Cathode	V_{cat}	12.7 ± 0.9	15.5 ± 1.3
Anode	V_{an}	4.7 ± 0.6	4.5 ± 0.4
Contact Tip	V_{cont}	0.48 ± 0.05	0.51 ± 0.03
Electrode	V_{elec}	2.17 ± 0.46	2.34 ± 0.21
Arc Column	V_{col}	9.5 ± 1.5	9.9 ± 1.7

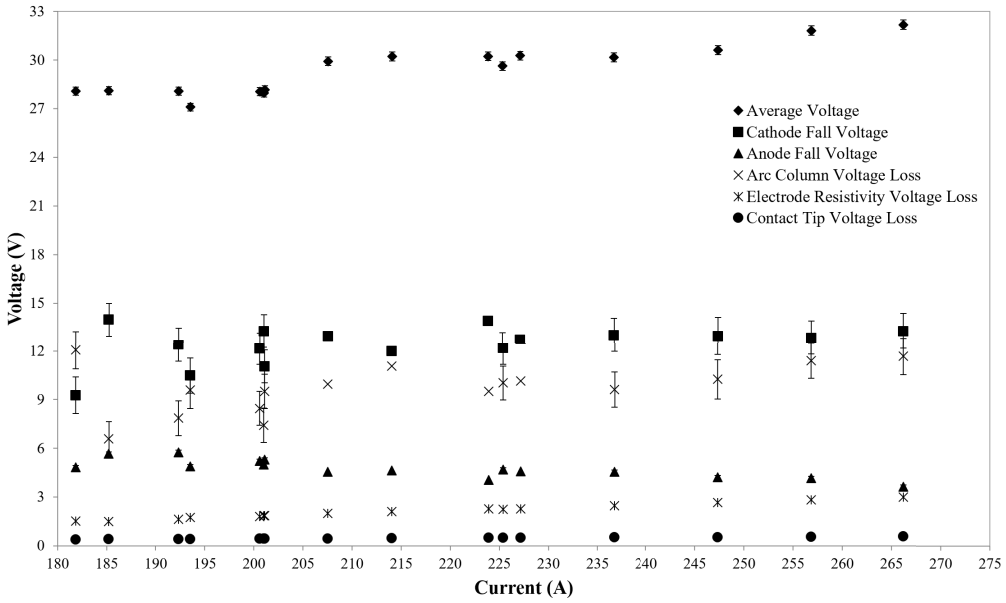

Fig. 3.4: Fall voltage measurements associated with 100% Ar shielding gas blend.

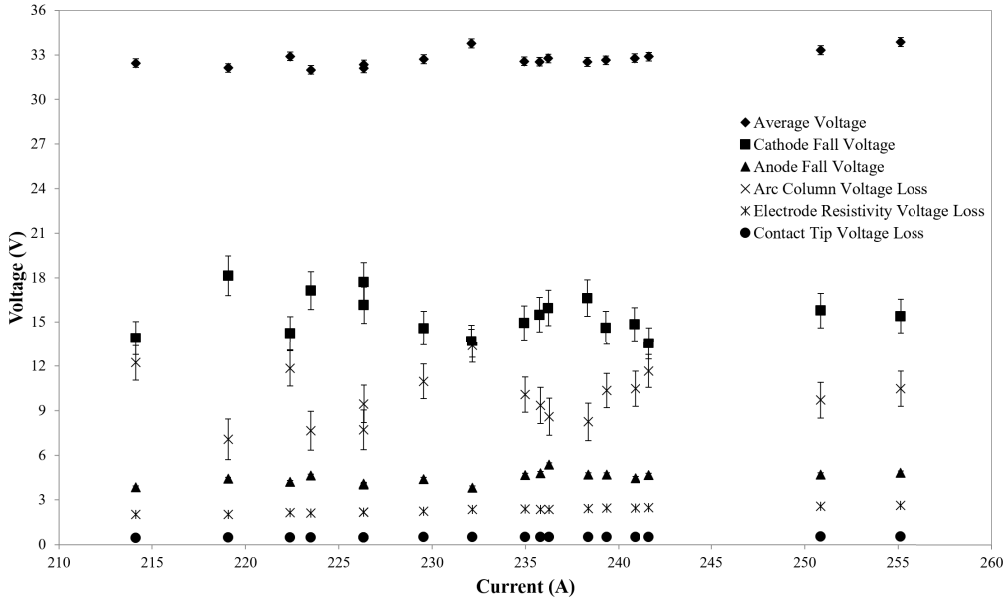

Fig. 3.5: Fall voltage measurements associated with 95% Ar - 5% CO_2 shielding gas blend.

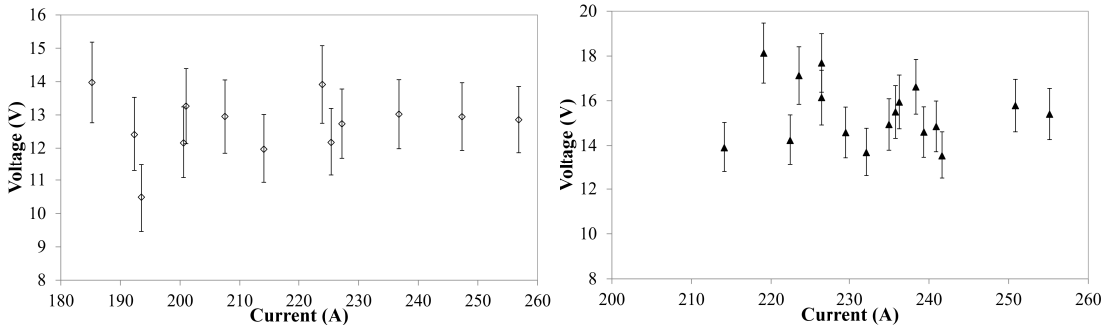

Fig. 3.6: Cathode fall voltage utilizing 100% Ar (left) and 95% Ar - 5% CO_2 (right) shielding gas blends.

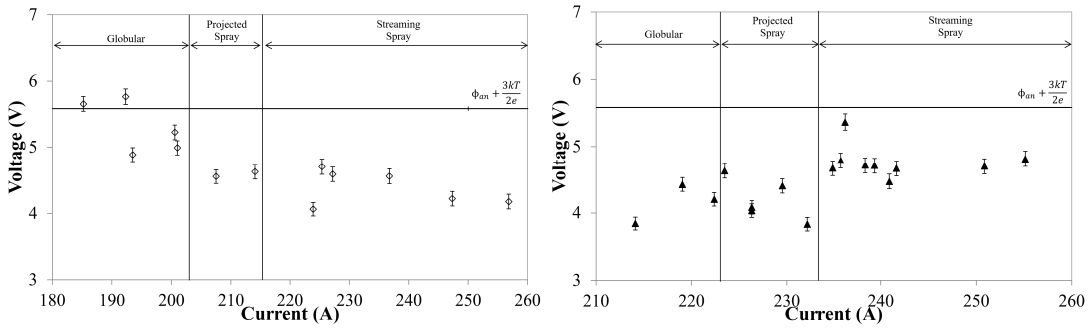

Fig. 3.7: Anode fall voltage utilizing 100% Ar (left) and 95% Ar - 5% CO_2 (right) shielding gas blends. Transitions between metal transfer modes are shown. Metal transfer modes were distinguished using droplet diameter, wire diameter, and high speed videography.

3.4.1. Cathode

Average overall cathode fall voltage was 12.7 ± 0.9 V and 15.5 ± 1.3 V for 100% Ar and 95% Ar - 5% CO_2 respectively as shown in Figure 3.6 and Table 3.3. Large experimental uncertainties were found in the overall cathode fall voltage due to the precision of the flow meter. The trend in the 100% Ar tests indicate that overall cathode fall voltage is independent from current. This trend was similarly proposed by literature but was never experimentally verified [18, 90, 91].

No trend was apparent in 95% Ar - 5% CO_2 overall cathode fall voltage results as these tests appeared to have a higher variance when compared to 100% Ar. The addition of CO_2 shielding gas increased spatter causing metal droplets to occasionally touch the cathode. At CO_2 concentrations ≥10%, steady state could not be reached as the cathode hole would become plugged or liquid metal would begin falling onto the calorimeter after contacting the cathode. This invalidated cathode and anode heat input results before steady state could be completed. Spatter with 95% Ar - 5% CO_2 shielding gas persisted but was much less influential compared to concentrations of ≥10% CO_2. 95% Ar - 5% CO_2 experiments were deemed acceptable as steady state could be reached, no cathode hole plugging occurred, no droplets appeared to contact the cathode before reaching the calorimeter, and the overall anode fall voltage measurements were consistent with those found in 100% Ar.

3.4.2. Anode

Average overall anode fall voltage was 4.7 ± 0.6 V and 4.5 ± 0.5 V for 100% Ar and 95% Ar - 5% CO_2 respectively as shown in Figure 3.7 and Table 3.3. Observing the results of 100% Ar and 95% Ar - 5% CO_2 simultaneously, overall anode fall voltage appears to be constant with

current. The transition through globular, project spray, and streaming spray did not have a clear effect on overall anode fall voltage as shown in Figure 3.7. The change in metal transfer mode between globular and projected spray was determined by comparing the wire diameter of 1.143 mm (0.045 in.) to the droplet diameter calculated using equation 3.8. If the droplet was larger than the wire diameter, metal transfer mode was globular. Significantly less experiments were performed in the globular regime due to the increased spatter associated with this metal transfer. The change between projected spray and streaming spray was apparent in the high speed videography.

Utilizing equation 3.2, an electron temperature of 6,000 K (10340 °F), and work function of 4.81 V for iron, overall anode fall voltage can be compared to the anode sheath voltage as shown in Figure 3.7 [16, 25–27, 92]. Average anode sheath voltage was determined to be on the order of -0.98 V. It was assumed that the electron temperature would not change with welding parameters.

3.4.3. Thermal Efficiency

Comparing the cathode and anode heat inputs with the overall heat input, thermal efficiency can be calculated. Typical thermal efficiencies range between 68-88%, is dependent on welding parameters, and dependent on joint configuration [3, 44, 55–59, 93]. Average thermal efficiency in experimentation was 69%. No apparent trend was found between efficiencies of different metal transfer modes. Comparing the heat input ratio between the cathode and anode, results indicate that approximately 67% and 33% of the captured heat was distributed to the cathode and anode respectively.

3.4.4. Contact Tip

Average contact tip voltage loss was 0.48 ± 0.05 V and 0.51 ± 0.03 V for 100% Ar and 95% Ar - 5% CO_2 respectively. Average resistance was 2.16 ± 0.50 $m\Omega$. Only a few experiments successfully measured contact tip voltage loss as the heat from the arc would melt the measuring device, or sliding contact was lost. It was assumed that the voltage loss in the contact tip would have a constant resistance for all welding parameters [84, 94]. This assumption was used to calculate the contact tip voltage loss for experiments where contact tip measurements were

unsuccessful. Contact tip resistance for all successful tests were averaged and was used to calculate voltage loss for unsuccessful experiments.

3.4.5. Electrode Extension

Average voltage loss due to resistivity in the electrode extension was 2.17 ± 0.46 and 2.34 ± 0.21 V for 100% Ar and 95% Ar - 5% CO_2 respectively. Electrode extension voltage loss was calculated using equation 3.4 with an electrode extension of 12.5 mm (0.5 in.). Initial testing showed that the electrode extension was not constant during welding with electrode extension variations of approximately ±0.5-1.0 mm. Welding parameters were selected so the average electrode extension was at the referenced 12.5 mm (0.5 in.) tungsten probe. Actual values of WFS and current were used in equation 3.4 to calculate voltage loss. The continuous change in electrode extension altered the instantaneous welding voltage and current leading to some variation in measurements.

3.4.6. Arc Column

Average arc column voltage loss was 9.5 ± 1.5 V and 9.9 ± 1.7 V for 100% Ar and 95% Ar - 5% CO_2 respectively. Arc column voltage loss was calculated using equation 3.9 with an arc length of 12.5 mm (0.5 in.). Arc column potential ranged between 0.52-1.05 V/mm with an average of 0.77 ± 0.12 V/mm. Arc column voltage loss appeared to linearly increase with current when using 100% Ar as shown in Figure 3.4. It could not be determined what trend was apparent when using 95% Ar - 5% CO_2 as variations were within experimental error.

3.5. Discussion

Results indicate that cathode, anode, and arc column are the dominant voltage loss regions with contact tip and electrode extension voltage loss being less significant. All results are comparable with those found in literature as summarized in Table 3.4.

Table 3.4: Comparison of GMAW fall voltages with literature.

Author	Shielding Gas	Overall Cathode Fall Voltage V_{cat} (V)	Overall Anode Fall Voltage V_{an} (V)	Anode Sheath Voltage V_A (V)	Contact Tip Voltage Loss V_{cont} (V)	Electrode Extension Voltage Loss V_{elec} (V)	Arc Column Potential V_{pot} (V/mm)
Lancaster [16]	100% Ar	15	5.5	1.5-2.0	-	-	1.0
Pfender [77]	100% Ar	-	-	(-3.4) - (-2.1)	-	-	-
Jonsson [66]	100% Ar	Sum = 13.3-14.9		-	1.3-1.7	0.5-1.0	1.0
Huismann [82]	100% Ar	11	5.5	-	-	-	0.8
Hajossy [79]	100% Ar	13.9	7.0	-	-	-	-
Hajossy [79]	100% CO2	14.5	4.9	-	-	-	-
Nemchinsky [18, 67]	100% Ar	-	8-9	-	-	-	-
Waszink [78, 83]	100% Ar	-	7-7.5	-	0.1-0.3	2.5	-
Wilson [85]	100% Ar	-	-	-	0.3-0.6	0.5-3.0	-
Shimizu [94]	100% Ar	-	-	-	0.4-0.55	-	-
Halmoy [39, 87]	100% Ar	-	-	-	-	1-5	0.6
McIntosh	100% Ar	12.7	4.7	-0.89	0.48	2.17	0.75
McIntosh	95%Ar - 5%CO2	15.5	4.5	-1.05	0.51	2.34	0.78

3.5.1. Cathode

Steel cathodes were used in experimentation to reproduce typical industrial cathode materials. Experimentation with steel cathodes could not be completed as insufficient thermal conductivity resulted in premature melting of the cathode prior to steady state. The similarity in work functions between copper and steel has led to comparable measurements as the differences in work function will have a minimal effect [1–3, 34–36, 43, 45]. Work function has a slight variation with crystalline orientation. Considering the (111) plane orientation, the work function for copper and steel are 4.94 V and 4.81 V respectively [92]. It would be expected that overall cathode fall voltage values would differ by 0.13 V between copper and steel. This difference is within experimental error and will likely have a minimal effect on results.

Overall cathode fall voltage was higher in experiments with 95% Ar - 5% CO_2 shielding gas as small amounts of spatter needed to be removed from the cathode. This small amount of spatter will inadvertently and artificially increase the cathode heat input. If the spatter had been collected at the time of experimentation, the increase in overall cathode fall voltage could be determined. It is estimated that for a 30 s test, 1-3 g of spatter was collected on the cathode. If the spatter has the same heat content as the droplets collected, the spatter would increase overall cathode fall voltage by approximately 0.5-1.5 V. If the excess spatter that landed on

the cathode had been collected, the additional heat input could have been more accurately predicted.

The large differences in overall cathode fall voltage between 100% Ar and 95% Ar - 5% CO_2 shielding gas blends indicates that shielding gas may be affecting the cathode fall voltage region. However, the spatter associated with the 95% Ar - 5% CO_2 shielding gas tests made conclusions difficult as it is unclear how much overall cathode fall voltage was increased.

Radiative heat from the arc column is lost and will contribute to heating of the cathode. This radiative heat will lead to slightly higher overall cathode fall voltages in all experiments. It is currently unclear how much of this radiative heat was captured by the cathode.

3.5.2. Anode

It is currently unclear if the distance from the electrode tip to the top the calorimeter is altering measurements [3, 34–36]. Previous work suggests this free flight distance does not affect measurements significantly but requires further investigation [2–4]. Energy measurements obtained were used to estimate droplet temperature. Droplet temperatures found were comparable with other non-intrusive methods such as pyrometry [2, 3, 41–45, 47].

Accurately determining voltage losses in the electrode extension and contact tip will directly influence overall anode fall voltage as shown in equation 3.2. Heat generated at the contact tip will be unevenly distributed between the contact tip and electrode. It was assumed that all heat generated at the contact tip will contribute to anode heating as the amount of heat distribution could not be determined. This will lead to a slightly low value of overall anode fall voltage.

Equation 3.2 does not account for evaporation. Droplet surface temperatures has been shown to be at or above boiling point [41]. Fumes from an ER70S-6 electrode have shown to be primarily composed of iron and manganese [3]. Using the enthalpy of vaporization of iron and manganese with fume formation rates, evaporation was calculated to increase overall anode fall voltage by approximately 0.05-0.45 V depending on welding parameters [14, 15]. Further investigation is still required to properly determine the extent of energy lost during experimentation. If evaporation and contact tip heat distribution were properly determined and incorporated, average overall anode fall voltage is believed to be closer to 5.1-5.5 V and will be more comparable with some literature [16, 82].

As shown in Figure 3.7, the values of thermal energy and work function were used to determine the anode sheath voltage of -0.98 V. This value is similar to Pfenders value of anode sheath voltage [77]. The work function of (111) pure iron and polycrystalline pure manganese are 4.81 and 4.1 V respectively [92]. Although the electrode is primarily composed of iron, the low concentration of Mn in the ER70S-6 electrode can lower the anode work function. Cathode and anode spots have been shown to preferentially form at locations with a lower ionization potential as these locations are easier to emit and condense electrons [16]. This difference in work function could increase calculated anode sheath voltage by 0.71 V. If evaporation and contact tip heat distribution are also considered, anode sheath voltage will be substantially closer to 0. This is why some researchers do not consider anode sheath voltage in equation 3.2 [18, 78].

3.5.3. Thermal Efficiency

A thermal efficiency of 69% was found in experimentation and is slightly low compared to previous measurements of thermal efficiency [44, 55–59, 93]. These previous measurements were primarily performed by welding directly on a plate calorimeter giving no capability of separating between cathode and anode heat inputs. The higher surface area of a plate calorimeter will yield a higher thermal efficiency as the larger surface area can absorb more radiative heat from the arc column. The small surface area of the cathode in this study does not permit large amounts of radiative absorption leading to a lower overall thermal efficiency. Models of the energy distribution in GMAW indicates that thermal efficiency is 68% when the cathode and anode do not receive radiative energy from the arc [68].

3.5.4. Contact Tip

Contact tip voltage loss will lead to heating of the welding torch and electrode. Temperature measurements in the water cooled torch was not used to determine heat inputs into the welding torch. Radiative heat from the arc will contribute to heating of the welding torch leading to an overestimation of heat input. The use of the custom contact tip and tungsten probe allowed for greater precision in contact tip voltage loss and overall anode fall voltage calculations. When the tungsten voltage probe was further away from the contact point, contact tip voltage measurements were shown to increase slightly due to electrode extension voltage loss.

3.5.5. Electrode Extension

Average voltage loss by resistivity in the electrode extension was 2.27 ± 0.34 V and is comparable with other literature who utilized similar currents, wire diameter and electrode extensions as shown in Table 3.4. Lehnhoff's model was greatly dependent on resistivity properties of the electrode. Resistivity properties of ER70S-6 were used over pure iron as the alloying elements will cause the resistance to be substantially higher [7, 8]. Any overestimation in the resistivity properties will greatly change electrode extension voltage loss.

3.5.6. Arc Column

The average arc column fall potential was measured to be 0.77 ± 0.12 V/mm. Equipment resolution, unwanted spatter, and propagation of errors resulted in experimental error being higher than desired. It was expected that the fall voltage of the 95% Ar - 5%CO_2 tests would be higher than 100% Ar as the dissociation of CO_2 requires additional energy. However, this conclusion could not be determined as arc column fall voltage variations were within experimental error.

As shown in Figure 3.4, arc column voltage loss appears to linearly increase with current. The increasing anode evaporation will decrease arc column temperatures and electrical conduction [25, 27, 68]. Further amounts of energy will be required for proper ionization and temperatures resulting in an increasing voltage loss.

Radiative heat from the arc column is lost and will contribute to heating of the cathode, anode, and welding torch. Approximately 13-33% of the total arc column energy is lost as radiative heat depending on welding parameters and arc length [16, 44, 93]. It is unclear how much of this heat was distributed to the cathode and anode. Arc column voltage was obtained by the difference in total voltage and the other voltage loss regions as shown in equation 3.9. This methodology will lead to a slight underestimation of the arc column fall voltage as the overall cathode fall voltage is overestimated and the overall anode fall voltage is underestimated.

3.6. Conclusions

A solid state calorimeter and a water cooled cathode were used to infer fall voltages in GMAW using a ER70S-6 carbon steel electrode with 100% Ar and 95% Ar - 5%CO_2 shielding gas

blends. Experimental current ranged between 185-266 A and extended through globular, projected spray, and streaming spray metal transfer modes. Arc length and electrode extension were both constant at approximately 12.5 mm (0.5 in.). The cathode, anode, contact tip, electrode extension, and arc column voltage losses measured were comparable with those found in literature.

The dominant voltage loss came from the cathode, anode, and arc column with the contact tip and electrode extension being less significant. Average overall cathode fall voltage was 12.7 $\pm$ 0.9 V and 15.5 $\pm$ 1.3 V for 100% Ar and 95% Ar - 5% CO_2 respectively. Overall cathode fall voltage was independent of current and is the first time to be experimentally verified. Average overall anode fall voltage was 4.7 $\pm$ 0.6 V and 4.5 $\pm$ 0.4 V for 100% Ar and 95% Ar - 5% CO_2 respectively. Overall anode fall voltage was independent of current and metal transfer mode and is slightly underestimated as evaporation was not measured. Droplet temperature measurements are comparable with other non-intrusive measuring methods helping the validity of calorimeter measurements.

Contact tip voltage loss was assumed to have a constant resistance across all welding parameters. Utilizing a tungsten probe, average contact tip voltage loss and resistance was measured to be 0.49 $\pm$ 0.04 V and 2.16 $\pm$ 0.5 $m\Omega$ respectively. Based on the work of Lehnhoff, average electrode extension voltage loss was 2.27 $\pm$ 0.34 V. Arc column fall voltage potential was 0.77 $\pm$ 0.12 V/mm and is the first time to be measured with this technique.

The experiments performed in this study gave consistent measurements when spatter was not an issue. Welding parameters were representative of a typical GMAW system and gave nearly all voltage loss measurements allowing a more comprehensive understanding of a GMAW arc. The results found in this study will assist various models giving greater insight in metal transfer, droplet temperature, fume formation, and heat distribution in the GMAW system.

4. Fall Voltages in Advanced Waveform Aluminum GMAW

4.1. Introduction

Waveform development has grown considerably over the past few decades with numerous waveforms existing to reduce vapours or heat input. In relation to Gas Metal Arc Welding (GMAW) of aluminum, various companies have changed these waveforms tailored to specific situations attempting to alleviate the difficulty in welding aluminum consumables. Small changes in waveforms can change metal transfer behaviour substantially and require thorough understanding to properly assess industrial feasibility.

With the wide industrial use of pulse-like waveforms, numerous studies have heavily investigated pulse waveforms primarily to optimize metal transfer, spatter, and heat input [95, 96]. These studies have shown that small changes in pulsing parameters can result in large variations in metal transfer behavior. While many studies have focused on optimizing welding parameters, fewer studies have focused on droplet energy content with even less on overall fall voltage measurements [18, 45, 97, 98]. With a close connection between metal transfer, deposition rates, energy distribution, and overall fall voltage, a proper understanding of the aluminum GMAW system is needed.

This paper explains how measurements of fall voltage, thermal efficiency and droplet heat content were experimentally obtained for five different waveforms in aluminum GMAW. It is believed that this was the first time that cathode fall voltage measurements were concurrently measured with other voltage losses for aluminum GMAW. This was undertaken to get a complete understanding of the aluminum GMAW system for various welding waveforms. Numerous comparisons between aluminum and steel were made as little comparative literature exists for aluminum [5]. Experimental decisions and parameters were selected primarily for their relation to typical welding systems allowing greater insight into the aluminum GMAW system.

4.2. Background

In welding, there is a large voltage loss associated very close to both the cathode and anode [16, 17]. The rapid reduction in temperature between the arc and cathode/anode surface creates a small boundary layer with a large thermal gradient which has insufficient energy for thermal

ionization [62]. This boundary layer will not have sufficient ions for proper electrical conductivity resulting in a large resistance and voltage loss. This boundary is known as a fall voltage region, drop potential region, or space charge zone and is present at both the cathode and anode surfaces. These regions can be determined with the Debye length and are approximately 0.05-100 μm in thickness depending on electron density and temperature [16, 18, 28, 53, 66, 69, 99].

A common assumption amongst researchers is that the fall voltage regions are the primary factor for heating in both the cathode and anode with convection, conduction, and radiation having a small impact [62]. This assumption is the basis for inferring the overall fall voltage measurements in this paper. In addition to the overall cathode and anode fall voltage, a typical welding system also has voltage loss associated with the torch/ground cables, contact tip, electrode, and arc column.

Numerous studies have found overall fall voltages in GMAW using various systems such as calorimeters, energy balances, models, and arc analysis [16, 18, 28, 65, 66, 78]. Overall fall voltages have three main components: a voltage associated with the non-equilibrium plasma in front of the electrode (the "sheath voltage"), the work function of the electrode material, and the energy associated with evaporation and condensation of electrons. These three components are captured by the following equations [16, 18, 28, 78]:

$$V_{cat} = \frac{q_{cat}}{I} = V_C - \phi_{cat} - \frac{3kT}{2e} \tag{4.1}$$

$$V_{an} = \frac{q_{an}}{I} - V_{elec} - V_{cont} = V_A + \phi_{an} + \frac{3kT}{2e} \tag{4.2}$$

Where V_{cat} is the overall cathode fall voltage, V_{an} is the overall anode fall voltage, q_{cat} is the total cathode heat input, q_{an} is the total anode heat input, I is the current, V_{elec} is the electrode extension voltage loss, V_{cont} is the contact tip voltage loss, V_C is the cathode sheath voltage, V_A is the anode sheath voltage, ϕ_{cat} is the work function of the cathode material, ϕ_{an} is the work function of the anode material, k is Boltzmann's constant, T is the electron temperature and e is electron charge [16]. If an arc temperature of 6,000 K is assumed, the thermal energy of electrons is approximately 0.78 V [25–27]. The choice of 6,000 K is based on the temperature at which Ar plasma starts to show significant electrical conductivity [11]. The work function has

a slight variation with crystalline orientation; considering the (111) plane, the work functions for pure copper, pure iron and pure aluminum are 4.94 V, 4.81 V and 4.26 V respectively [92].

Previous to this work, a very limited amount of research has been performed in the determination of overall cathode and anode fall voltage in aluminum systems. Experimental measurements have primarily focused on steel systems with a heavy emphasis on the determination of overall anode fall voltage for droplet heat content, vapourization rates, and deposition rates. Various values of fall voltages are summarized in Table 4.1. Some literature has measured sheath fall voltage directly while others have measured overall fall voltage.

Table 4.1: Comparison of some published GMAW fall voltages.

Author	Electrode Material	Shielding Gas	Overall Cathode Fall Voltage V_{cat} (V)	Overall Anode Fall Voltage V_{an} (V)	Cathode Sheath Voltage V_C (V)	Anode Sheath Voltage V_A (V)	Contact Tip Voltage Loss V_{cont} (V)	Electrode Extension Voltage Loss V_{elec} (V)	Arc Column Potential V_{pot} (V/mm)
McIntosh [5]	Steel	100% Ar	12.7	4.7	18.44	-0.89	0.48	2.17	0.75
McIntosh [5]	Steel	95%Ar - 5%CO2	15.5	4.5	21.20	-1.05	0.51	2.34	0.78
Lancaster [16]	Steel	100% Ar	15	5.5	-	1.5-2.0	-	-	1.0
Pfender [28, 65]	Steel	100% Ar	-	-	11.5	(-3.4) - (-2.1)	-	-	-
Jonsson [66]	Steel	100% Ar	Sum = 13.3-14.9		-	-	1.3-1.7	0.5-1.0	1.0
Huismann [100]	Steel	100% Ar	11	5.5	-	-	-	-	0.8
Hajossy [79]	Steel	100% Ar	13.9	7.0	-	-	-	-	-
Hajossy [79]	Steel	100% CO2	14.5	4.9	-	-	-	-	-
Nemchinsky [18, 67]	Steel	100% Ar	-	8-9	-	-	-	-	-
Waszink [78, 83]	Steel	100% Ar	-	7-7.5	-	-	0.1-0.3	2.5	-
Wilson [85]	Steel	100% Ar	-	-	-	-	0.3-0.6	0.5-3.0	-
Shimizu [94]	Steel	100% Ar	-	-	-	-	0.4-0.55	-	-
Halmoy [39, 87]	Steel	100% Ar	-	-	-	-	-	1-5	0.6
Fu [97]	Aluminium	100% Ar	-	4.5	-	-	-	-	-
Lu [98]	Aluminium	100% Ar	-	5-7	-	-	-	-	-
Nemchinsky [18, 67]	Aluminium	100% Ar	-	6.8-7.5	-	-	-	-	-

Five different types of waveforms were utilized in this paper. These waveforms were constant voltage (CV) and advanced waveforms: constant power, pulse, constant current (CC) pulse, and pulse on pulse. Examples of the advanced waveforms are summarized in Figure 4.1.

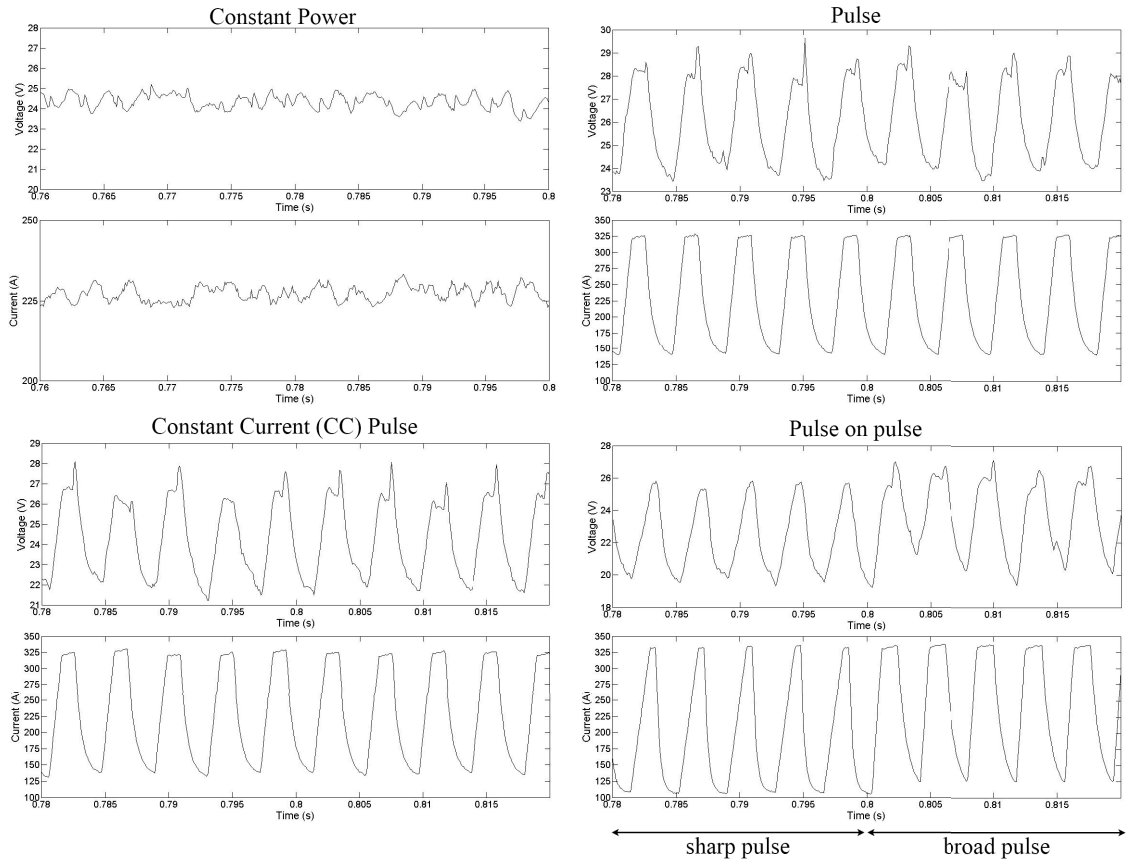

Fig. 4.1: Typical signals of the advanced waveforms used in experimentation.

All advanced waveforms used in experimentation maintained a constant average deposition rate. Constant power is a waveform which varies voltage and current simultaneously to maintain a constant heat input into the workpiece. All pulse waveforms vary current between a peak and background current to force droplet detachment with Lorentz forces. Pulse and CC pulse waveforms are very similar but will either prioritize a CV or CC setting. The pulse on pulse waveform varies the waveform shape to change arc length during welding giving the final weld bead a Gas Tungsten Arc Weld like appearance.

4.3. Experimental Setup

All welding was performed with a Lincoln Power Wave S500 and a Lincoln 84 Dual Feeder. A 25 ft. (7.62 m), #2 (35 mm^2) Lincoln Magnum PRO AL G450A K3355-2 torch was utilized with 5 ft (1.5 m) of grounding cables. All welds were done on a 1.2 mm (3/64 in.) 4043 aluminum consumable in direct current electrode positive polarity (DCEP). Pure Ar shielding gas was mixed to 40 standard cubic feet per hour (SCFH) (18.88 L/min) utilizing an Alicat

MCP-50SLPM-D gas flow controller.

Experimentation consisted of welding with five waveforms using weld set reference Z153615. These waveforms were CV (program 71), Powermode (constant power - program 40), pulse (program 72), CC pulse (program 69), and pulse on pulse (program 99). These waveforms were selected based on the chosen power supply and commercially available waveforms associated with this power supply. Voltage settings were adjusted for each waveform in an attempt to have similar arc lengths between each waveform. Arc lengths were manually determined for each test as discussed below. Each test was repeated three times for repeatability and statistical variance.

The calorimetry setup is identical to that used by McIntosh and Scott as seen in Figure 4.2 [2, 4, 5]. For a detailed explanation of the experimental setup see the work by McIntosh or Scott [2, 4, 5].

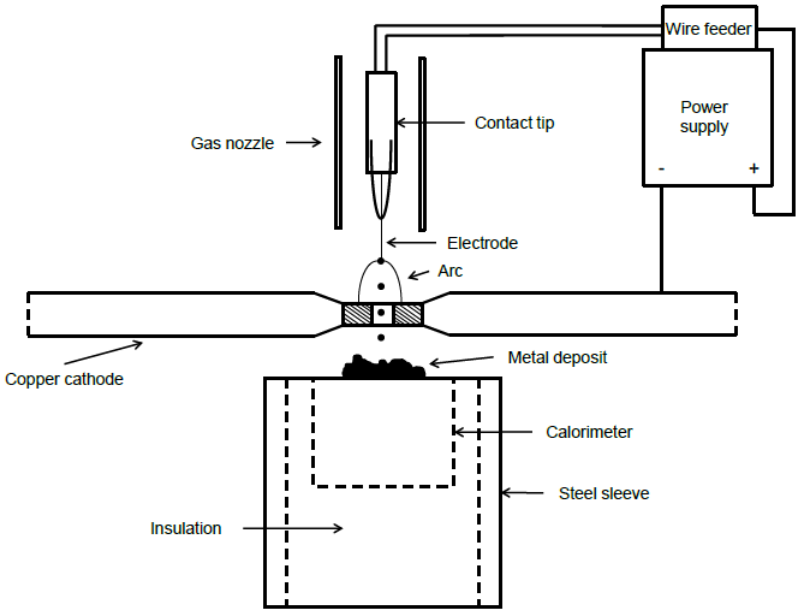

Fig. 4.2: Diagram showing the experimental setup of the solid state calorimeter and copper cathode (not to scale) [2, 4, 5].

The setup consists of several components including a solid state calorimeter, water cooled copper cathode, synchronized high speed videography, and data acquisition. These components provide measurements of the cathode and anode heat inputs independently. The experimental setup is limited to free-flight metal transfer modes with no capability of performing short-circuit

waveforms. Properties of pure copper and aluminum LM25 were used for the calorimeter and wire respectively [50, 89].

4.3.1. Data Acquisition

Current and voltage data was synchronized with the high speed videography at 100 kHz over 2.8 s to determine average and instantaneous welding parameters. Total voltage measurement were performed between the welding torch and plate and did not include voltage losses through the torch cable.

A secondary data acquisition was obtained through the Lincoln Power Wave S500 power supply utilizing the Lincoln Weldview software. Data was acquired at 60 kHz for 8.2 s. This data acquisition included the voltage loss through the welding torch cables/leads. Wire feeding rate could be measured with this data acquisition and was used for the volumetric melting rates. Voltage loss in the torch cables was determined based on the difference in overall voltage between the two data acquisition systems.

4.3.2. Droplet Diameter

The frequency of detachment was measured by manually counting droplets. High speed videography was used to count 100 droplets in their respective time frame. FFT analysis of current and voltage signals were found to be consistent with manual counting when parameters were within a one drop per pulse (ODPP) condition. It was found that some of the tests had multiple drops per pulse (MDPP), invaliding the FFT results. For consistency between experiments, all frequency of detachment measurements were found by manually counting 100 droplets in their respective time frame.

4.3.3. Arc Length

A typical definition of arc length would be the distance from the tip of the welding electrode to the adjacent surface of the weld pool [101]. No cathode material existed directly beneath the electrode eliminating the validity of this definition for the calorimetry setup. Instead, arc length was determined to be the shortest distance between the edge of the cathode hole and the electrode solid-liquid interface as shown in Figure 4.3.

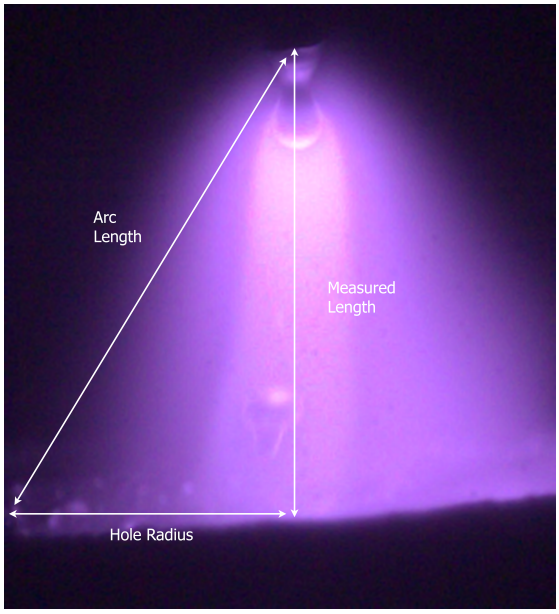

Fig. 4.3: High speed video was used to find measured length during calorimetry experiments. Arc length was then calculated based on a 5 mm (0.20 in.) radius hole.

The electrodes solid-liquid interface was used as one point for arc length measurements based on the work of Egerland and Schnick [27, 68, 101]. During droplet growth, a high concentration of metal vapour growths directly below the droplet, lowering temperature and electrical conductivity of the plasma in this localized region [27]. These vapours lead to a colder inner arc column region which is visible in Figure 4.3 as a brighter inner arc [27]. This localized region inhibits current flow leading to anode spots being preferentially located higher up the droplet. The relatively hotter outer arc will have a higher electrical conductivity, temperature, and current density. As seen in Figure 4.3, the outer arc column attaches as high as the solid-liquid interface. These findings show that the solid-liquid interface should be used for arc length measurements as this is a better representation of current flow and anode spot attachment [68]. Anode spots will still exist on the bottom of the droplet but will be fewer in number comparatively.

Egerland found that measurements were far more consistent amongst researchers when using the electrode solid-liquid interface [101]. The conventional definition of arc length is subjective to error from the time dependent measurements while measurements from the solid-liquid interface were found to be substantially less variable [101].

Arc length was determined through simple trigonometry between the measured length and cathode hole radius of 5 mm (0.20 in.) as shown in Figure 4.3. High speed video was taken at

10,000 frames per second and used to determine metal transfer mode, arc length, and electrode extension. The varying nature of the GMAW process resulted in changes in the electrode extension and arc length. To account for these variations, maximum and minimum measured electrode extension was determined over a 2.8 second period. These values were averaged to give an average electrode extension and measured length during testing.

4.3.4. Aluminum Plate Welding

A small number of tests were conducted on aluminum plates to verify that metal transfer, droplet detachment frequency, and droplet diameter were comparable between the calorimeter and industrial settings. An exact replicate of the welding parameters could not be completed on both the calorimetry setup and aluminum plate. Arc length and voltage values associated with the calorimetry setup was slightly higher than typical welding parameters in the aluminum plate tests. An increased arc length provided a wider and more stable arc in the calorimetry setup. Only CV was compared between experimental systems. Bead on plate welds were performed on wire brushed 6061 grade aluminum in the 1G (PA) position with a travel speed of 30 inch/min (0.76 m/min).

4.4. Results

Heat distribution was measured for five different aluminum GMAW waveforms as shown in Table 4.2. Overall voltage losses for the cathode, anode, contact tip, electrode extension, arc column, and cable/leads were found as shown in Table 4.3. For clarity, average results are summarized in Figure 4.4. Experimentation with an Al-Mg (5356) aluminum consumable could not be conducted due to increased spatter associated with the high levels of Mg in this wires composition [102, 103]. Tests with an Al-Mg wire was conducted and resulted in plugging of the cathode hole giving incomplete results. Since no comparative literature could be found measuring overall cathode and anode fall voltages, results of aluminum GMAW are shown alongside carbon steel for comparison purposes [5].

Table 4.2: Experimental welding parameters and heat distribution of various waveforms utilizing a 1.2 mm (3/64 in.) 4043 aluminum consumable in pure Ar shielding gas. All tests were repeated three times. Uncertainty values shown are standard deviations between tests. Arc length and electrode extension add up to slightly more than the CTWD because they are not aligned, as shown in Figure 4.3.

Waveform	Average Voltage (V)	Average Current (A)	Wire Feed Rate (inch/min)	Contact Tip to Work Piece Distance (mm)	Electrode Extension (mm)	Actual Arc Length (mm)	Arithmetic Instantaneous Power (W)	Anode Heat Input (W)	Cathode Heat Input (W)	Thermal Efficiency (%)
CV	26.5 ± 0.0	166.5 ± 1.1	274.8 ± 0.3	25.4	12.7 ± 1.6	13.7 ± 1.5	4420 ± 28	1051 ± 7	1797 ± 219	64.4 ± 4.7
Constant Power	26.4 ± 0.2	166.1 ± 0.9	274.2 ± 0.2	25.4	11.9 ± 0.9	14.4 ± 0.8	4386 ± 5	1050 ± 8	1668 ± 43	62.0 ± 1.0
Pulse	25.0 ± 0.1	149.4 ± 0.8	274.8 ± 0.6	25.4	10.7 ± 1.0	15.5 ± 1.0	3971 ± 8	1020 ± 6	1677 ± 164	67.9 ± 4.2
Pulse on pulse	25.4 ± 0.5	152.3 ± 1.1	273.7 ± 0.5	25.4	13.5 ± 0.5	12.9 ± 0.5	4107 ± 62	1032 ± 20	1714 ± 72	66.9 ± 2.8
CV	26.9 ± 0.0	228.6 ± 1.9	399.9 ± 0.1	15.9	7.1 ± 0.5	10.1 ± 0.5	6150 ± 48	1597 ± 5	2458 ± 88	66.0 ± 1.8
Constant power	24.5 ± 0.1	226.0 ± 1.2	400.1 ± 0.9	15.9	11.0 ± 0.4	7.0 ± 0.3	5541 ± 3	1565 ± 13	2420 ± 26	71.9 ± 0.7
Pulse	26.0 ± 0.3	229.5 ± 2.2	400.0 ± 0.0	15.9	8.1 ± 1.2	9.3 ± 1.0	6099 ± 9	1530 ± 47	2539 ± 185	66.7 ± 2.2
CC Pulse	24.9 ± 0.3	227.2 ± 0.2	399.1 ± 0.4	15.9	10.0 ± 1.2	7.8 ± 0.9	5802 ± 77	1568 ± 47	2510 ± 81	70.3 ± 2.1
Pulse on pulse	22.3 ± 0.9	220.3 ± 0.2	400.0 ± 0.0	15.9	14.2 ± 0.6	5.3 ± 0.2	5153 ± 108	1541 ± 9	2391 ± 103	76.3 ± 1.0
Overall Average	25.3 ± 2.4	196.2 ± 20.0	344.1 ± 38.6	15.9	11.0 ± 2.5	10.7 ± 3.5	5070 ± 819	2975 ± 80	2131 ± 397	68.1 ± 4.8

Table 4.3: Fall voltage values for various waveforms utilizing a 1.2 mm (3/64 in.) 4043 aluminum consumable in pure Ar shielding gas. Uncertainty values shown are standard deviation.

Waveform	Average Current (A)	Overall Cathode Fall Voltage (V)	Overall Anode Fall Voltage (V)	Contact Tip Voltage Loss (V)	Electrode Extension Voltage Loss (V)	Overall Arc Column Fall Voltage (V)	Arc Potential (V/mm)	Torch Cable/Leads Voltage Loss (V)
CV	166.5 ± 1.1	10.79 ± 1.25	5.78 ± 0.01	0.47 ± 0.003	0.06 ± 0.01	9.45 ± 1.26	0.69 ± 0.08	1.35 ± 0.11
Constant Power	166.1 ± 0.9	10.04 ± 0.24	5.80 ± 0.03	0.47 ± 0.002	0.05 ± 0.00	10.04 ± 0.32	0.70 ± 0.07	1.58 ± 0.18
Pulse	149.4 ± 0.8	11.22 ± 1.04	6.36 ± 0.04	0.43 ± 0.002	0.04 ± 0.00	6.99 ± 1.11	0.45 ± 0.05	1.49 ± 0.19
Pulse on pulse	152.3 ± 1.1	11.25 ± 0.52	6.29 ± 0.13	0.43 ± 0.003	0.05 ± 0.00	7.36 ± 0.81	0.57 ± 0.06	1.96 ± 0.59
CV	228.6 ± 1.9	10.76 ± 0.46	6.29 ± 0.04	0.65 ± 0.005	0.04 ± 0.00	9.16 ± 0.47	0.91 ± 0.07	1.52 ± 0.24
Constant power	226.0 ± 1.2	10.71 ± 0.15	6.22 ± 0.08	0.64 ± 0.003	0.07 ± 0.00	6.88 ± 0.17	0.98 ± 0.06	1.62 ± 0.17
Pulse	229.5 ± 2.2	11.07 ± 0.78	5.97 ± 0.21	0.65 ± 0.006	0.05 ± 0.01	8.26 ± 0.63	0.90 ± 0.16	1.86 ± 0.22
CC Pulse	227.2 ± 0.2	11.05 ± 0.36	6.19 ± 0.20	0.65 ± 0.001	0.06 ± 0.01	6.93 ± 0.60	0.89 ± 0.04	1.94 ± 0.28
Pulse on pulse	220.3 ± 0.2	10.86 ± 0.47	6.29 ± 0.05	0.63 ± 0.001	0.08 ± 0.00	4.42 ± 0.60	0.83 ± 0.10	1.07 ± 0.36
Overll Average	196.2 ± 34.2	10.86 ± 0.76	6.13 ± 0.24	0.56 ± 0.097	0.06 ± 0.01	7.72 ± 1.78	0.77 ± 0.19	1.60 ± 0.36

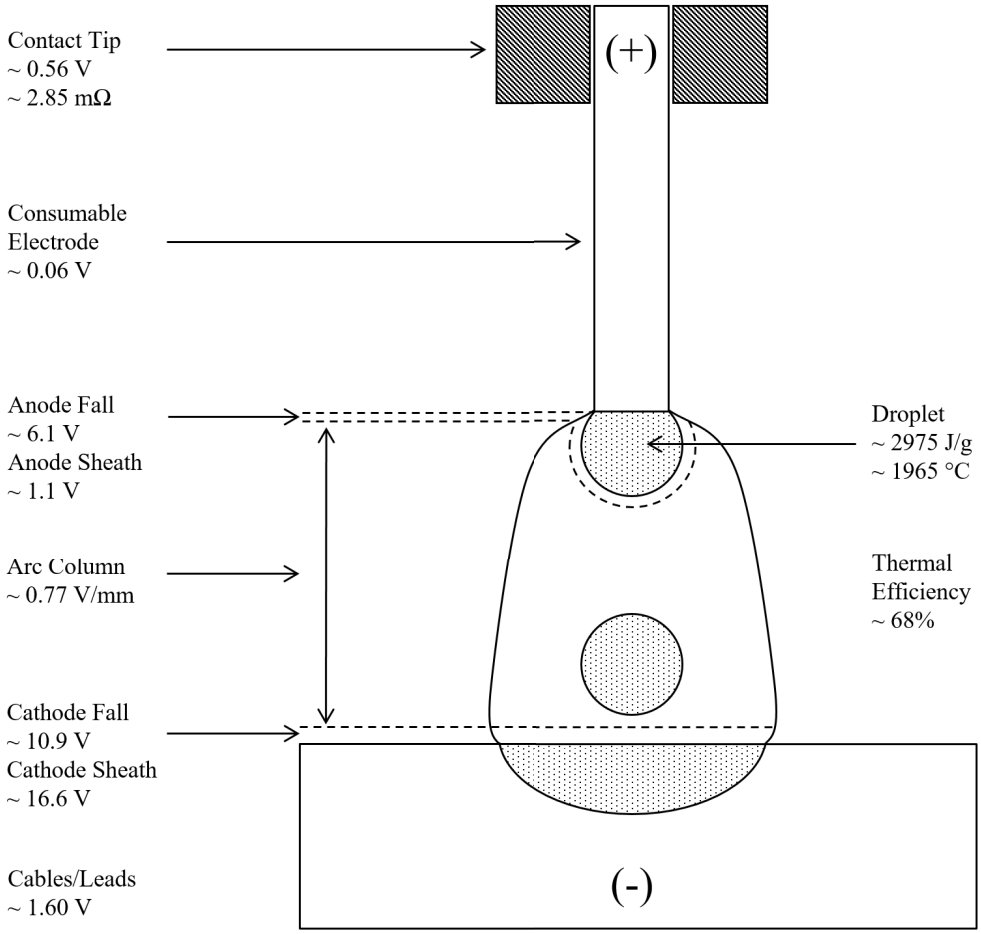

Fig. 4.4: Summary of results in aluminum GMAW for a 1.2 mm (3/64 in.) 4043 aluminum consumable using pure Ar shielding gas. Results will be dependent on welding parameters with all values representing an average.

4.4.1. Cathode

Overall cathode fall voltage ranged between 9.53 V and 12.49 V with an average of 10.86 ± 0.76 V. Results between the different waveforms and currents indicate that the overall cathode fall voltage is the same between tests as shown in Figure 4.5. Utilizing Equation 4.1 average cathode sheath voltage was calculated to on the order of 16.57 ± 0.76 V . Based on previous work, cathode fall voltage is approximately constant with current [5].

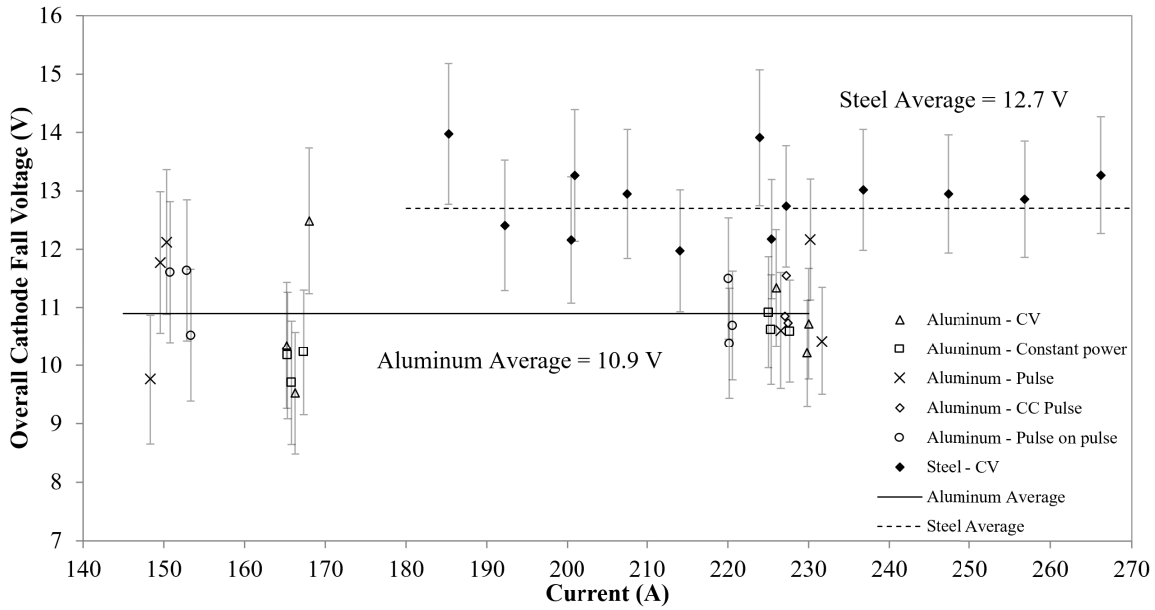

Fig. 4.5: Overall cathode fall voltage as a function of current for a 1.143 mm (0.045 in.) ER70S-6 steel electrode and a 1.2 mm (3/64 in.) 4043 aluminum electrode. Shielding gas was 100% Ar for both electrodes.

4.4.2. Anode and Droplet Heat Content

Overall anode fall voltage ranged between 6.47 V and 5.67 V with an average of 6.13 ± 0.24 V. Utilizing Equation 4.2 average anode sheath voltage was calculated to be on the order of 1.10 ± 0.24 V. Anode fall voltage was dependent on waveform selection and was predominantly different between pulse and non-pulse waveforms. Pulse waveforms were shown to have a higher overall anode fall voltage at lower currents. Based on previous work, anode fall voltage is approximately constant with current [5, 18, 78].

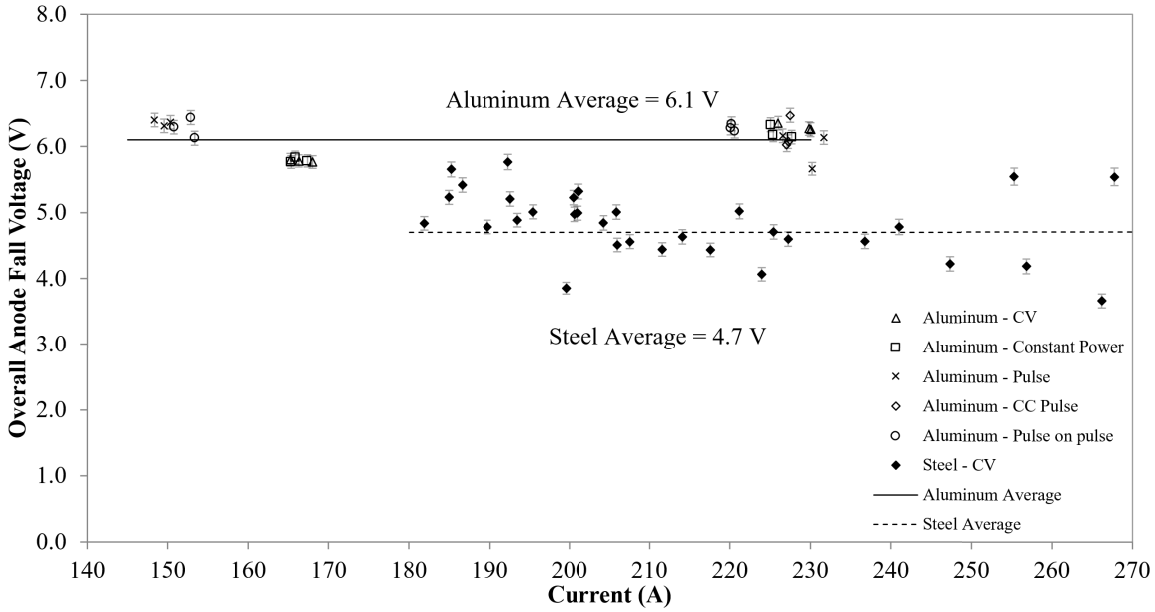

Fig. 4.6: Overall anode fall voltage as a function of current for a 1.143 mm (0.045 in.) ER70S-6 steel electrode and a 1.2 mm (3/64 in.) 4043 aluminum electrode. Shielding gas was 100% Ar for both electrodes. Trends are for CV only.

Overall droplet heat content and droplet temperature was measured for five different waveforms as shown in Table 4.4. Droplet heat content ranged between 2832 J/g and 3159 J/g with results comparable to those found in literature [3, 35, 38, 97, 98, 104]. This heat content correlated to a droplet temperature range of 1812 °C and 2139 °C. Average overall droplet heat content for pulse waveforms was lower than non-pulse waveforms. Repeated tests showed that this variance is not significant at the currents tested.

Table 4.4: Droplet heat content and temperature for various waveforms in a 1.2 mm (3/64 in.) 4043 aluminum consumable using pure Ar shielding gas. Uncertainty values shown are standard deviation.

Waveform	Average Current (A)	Frequency of Detachment Based on Waveform (Hz)	Frequency of Detachment Based on Videos (Hz)	Drops per pulse	Droplet Diameter (mm)	Droplet Heat Content (J/g)	Droplet Temperature (°C)
CV	166.5 ± 1.1	102 ± 39	163 ± 4	-	1.12 ± 0.01	2957 ± 19	1959 ± 25
Constant Power	166.1 ± 0.9	74 ± 0	152 ± 6	-	1.14 ± 0.01	2955 ± 23	1946 ± 17
Pulse	149.4 ± 0.8	170 ± 1	174 ± 3	1.03 ± 0.02	1.09 ± 0.01	2870 ± 16	1896 ± 26
Pulse on pulse	152.3 ± 1.1	195 ± 2	212 ± 10	1.09 ± 0.05	1.02 ± 0.02	2903 ± 56	1944 ± 36
CV	228.6 ± 1.9	74 ± 0	381 ± 2	-	0.95 ± 0.00	3089 ± 9	2043 ± 14
Constant power	226.0 ± 1.2	81 ± 5	376 ± 11	-	0.96 ± 0.01	3027 ± 25	1977 ± 19
Pulse	229.5 ± 2.2	240 ± 4	342 ± 7	1.43 ± 0.05	0.99 ± 0.01	2959 ± 90	1942 ± 97
CC Pulse	227.2 ± 0.2	241 ± 0	316 ± 28	1.31 ± 0.12	1.02 ± 0.03	3032 ± 91	2012 ± 91
Pulse on pulse	220.3 ± 0.2	263 ± 0	341 ± 10	1.29 ± 0.04	0.99 ± 0.01	2981 ± 18	1970 ± 14
Average	196.2 ± 20.0	160 ± 75	273 ± 91	1.23 ± 0.16	1.03 ± 0.07	2975 ± 80	1965 ± 63

4.4.3. Thermal Efficiency

Comparing the cathode and anode heat inputs with the average instantaneous power, thermal efficiency was calculated as shown in Table 4.2. Thermal efficiency ranged between 60 % and 77 % with an average of 68.1 ± 4.8 %. This thermal efficiency was slightly low compared to previously reported ranges of 68% to 88% [55–58, 93, 105, 106].

Comparing thermal efficiencies between waveforms indicate that pulse waveforms have a slightly higher thermal efficiency than non-pulse waveforms. These results are similar to those found in literature [93]. These results were within experimental uncertainties indicating that this variance is not significant. Comparing the overall heat input between the cathode and anode, results indicate that approximately 67% and 33% of the captured heat was distributed to the cathode and anode respectively [4].

4.4.4. Contact Tip

Average contact tip voltage loss and resistance was 0.56 ± 0.10 V and 2.85 ± 0.54 $m\Omega$ respectively. 10 experiments successfully measured contact tip voltage loss as radiative heat from the arc melted the measuring setup, or sliding contact was lost. These 10 experiments consisted of at least 1 measurement from all 5 waveforms as shown in Figure 4.7. It was assumed that the voltage loss in the contact tip would have a constant resistance for all welding parameters and waveforms [84, 94]. This assumption was used to calculate the average contact tip resistance from all successful experiments. This average resistance was then used to calculate voltage loss for all experiments.

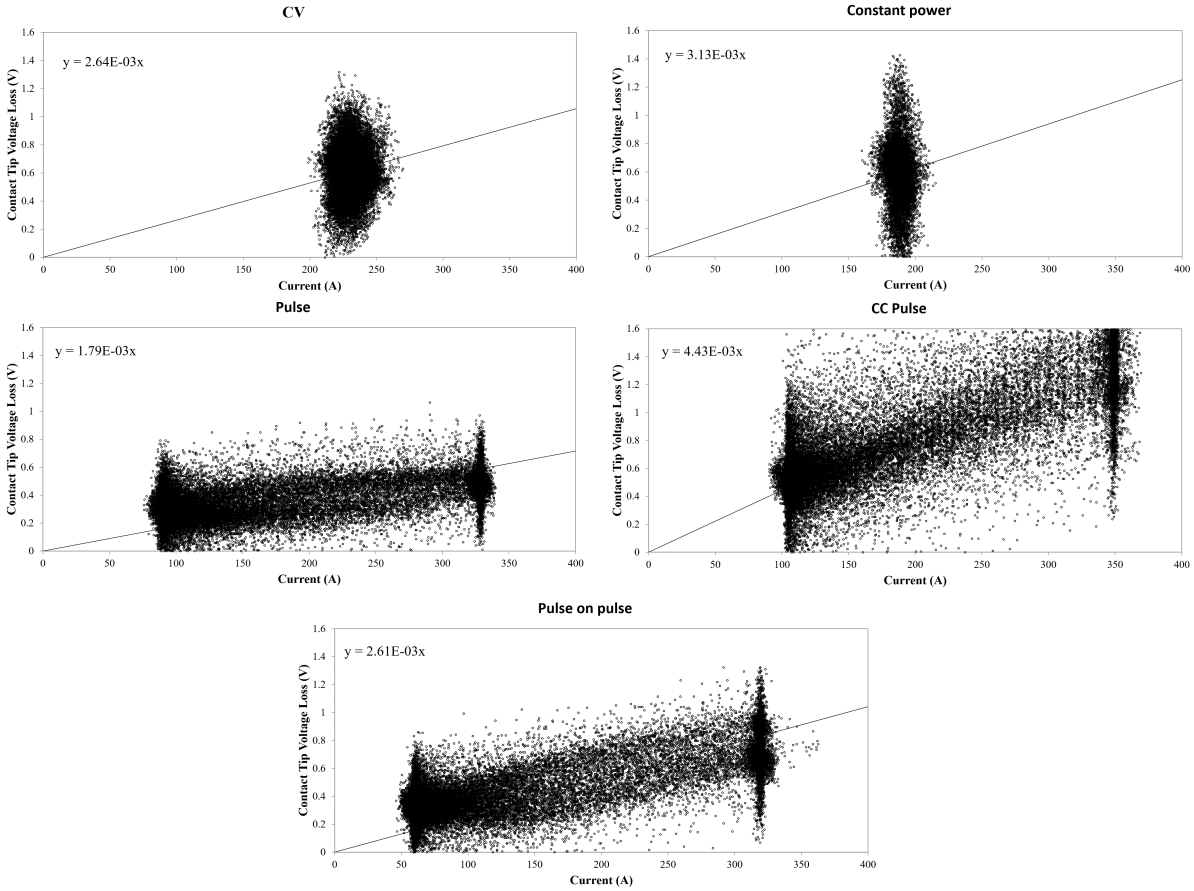

Fig. 4.7: Overall contact tip voltage loss waveform tests in a 1.2 mm (3/64 in.) 4043 aluminum electrode. Voltage loss is proportion to current indicating a constant resistance. Average resistance was used in all calculations.

4.4.5. Electrode Extension

Average electrode extension voltage loss was calculated to be 0.06 ± 0.01 V. High speed videography showed that electrode extension was not constant during welding with electrode extension variations of approximately 0.5 mm to 2.0 mm. Based on the waveform behaviour, the pulse on pulse waveform had the largest variation in electrode extension ranging upwards of 4 mm. Despite the varying electrode extension behaviour, voltage loss in the electrode extension was negligible compared to the other voltage losses indicating that Ohmic heating is not significant.

4.4.6. Arc Column

Arc column potential was determined for each test based on the arc length as shown in Figure 4.3. Average arc column potential was 0.77 ± 0.19 V/mm and appeared to be dependent on current as shown in Figure 4.8. A linear trend was approximated based on previous findings in

steel electrodes [5].

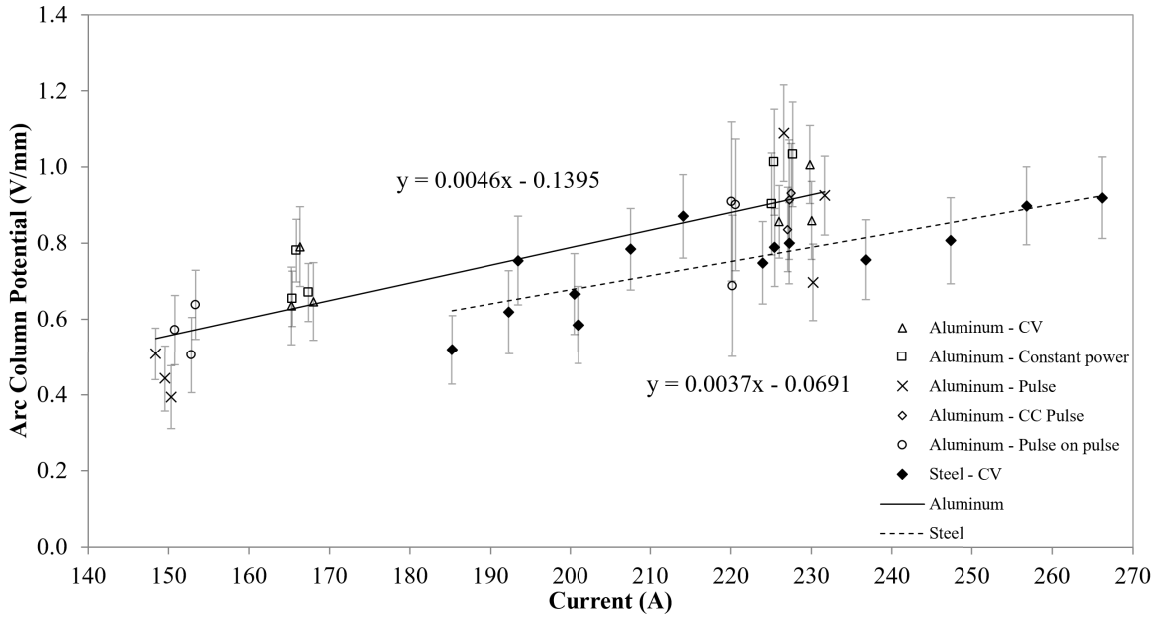

Fig. 4.8: Overall arc column potential as a function of current for a 1.143 mm (0.045 in.) ER70S-6 steel electrode and a 1.2 mm (3/64 in.) 4043 aluminum electrode. Shielding gas was 100% Ar for both electrodes. Trends are for CV only.

4.4.7. Torch Cables

Averaging voltage loss through the welding torch and cables was 1.60 ± 0.36 V. Average voltage potential through the torch cable/leads was 0.17 ± 0.05 V/m. Voltage loss in the welding leads was slightly higher for pulse-like waveforms from the increased impedance. This voltage difference between pulse and non-pulse waveforms was approximately 0.2 V to 0.4 V. Average resistance for CV was 7.4 ± 1.1 $m\Omega$ and is dependent on torch design.

4.4.8. Aluminum Plate Welding and Detachment Frequency

A small number of tests were conducted on 6061 aluminum plates with results summarized in Table 4.5. Results indicate that the calorimeter is representative of typical metal transfer mode and droplet diameter when arc length is sufficiently large in aluminum plate welding. A short arc length was shown to have a lower frequency of detachment without a substantially change in current. When welding on an aluminum plate, the short arc appeared to have plasma above the solid-liquid interface as shown in Figure 4.9.

Table 4.5: A comparison of the calorimetry setup with industrial plate welding.

Waveform	Cathode Setup	Instantaneous Voltage (V)	Instantaneous Current (A)	Instantaneous Electrode Extension (mm)	Instantaneous Arc Length (mm)	Average Frequency of Detachment (Hz)	Average Droplet Diameter (mm)
CV	Calorimeter	26.7	228.6	6.9	8.98	381	0.955
CV	6061 Al Plate	23.6	231.6	10.6	5.24	391	0.947
CV	6061 Al Plate	22.4	227.1	13.0	3.10	293	1.042

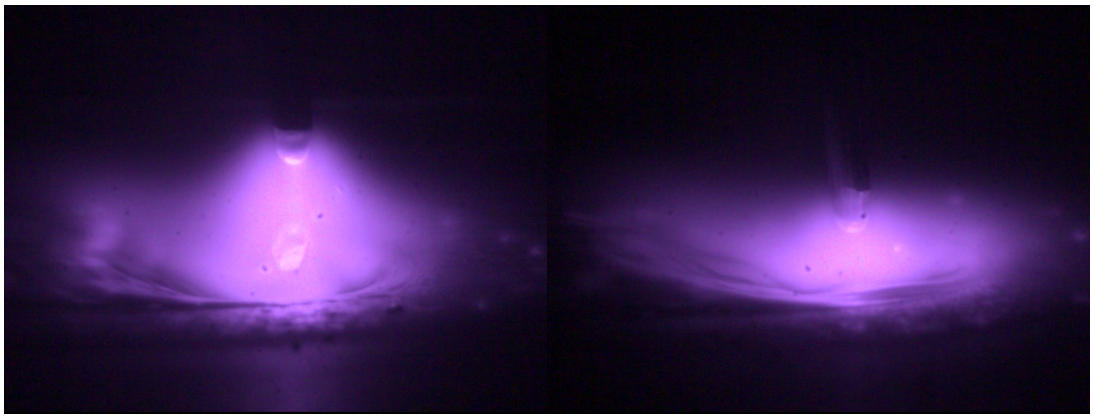

Fig. 4.9: Comparison of arc column appearance with a long (left) and short (right) arc length. Arc column appears to be interacting with the solid electrode in short arc tests. Welds were a 1.2 mm (3/64 in.) 4043 aluminum consumable on a 6061 aluminum plate. See Table 4.5 for details.

4.4.9. Voltage and Deposition Estimation

As shown in Figures 4.5 - 4.8, the trendlines associated with aluminum can be used to estimate the voltage at any given welding current. These trends were used to predict the voltage loss for a pulse waveform and compared with actual results. As shown in Figure 4.10, background and peak current are approximately 150 A and 325 A respectively. Instantaneous voltage was calculated based on instantaneous current and arc length as summarized in Table 4.6.

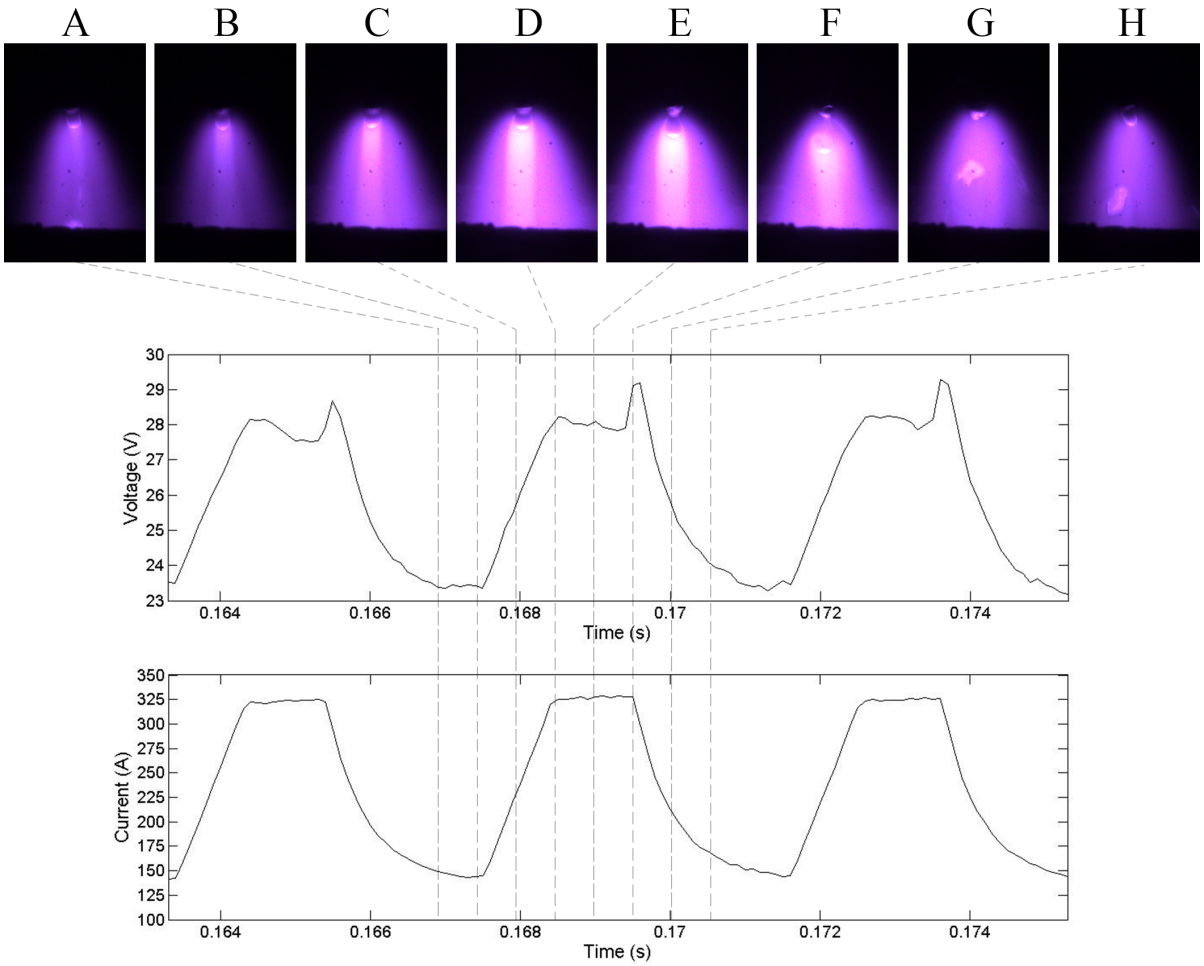

Fig. 4.10: Pulse experiment showing instantaneous voltage, current, arc length, and metal transfer during testing. Values were used to estimated instantaneous voltage from results as shown in Table 4.6.

Table 4.6: Estimation of instantaneous voltage based on trendlines found in cathode, anode, contact tip, electrode extension, and arc column fall voltages. Arc length was constant at 9.4 mm for each estimation based from Figure 4.10.

Image	Instantaneous Voltage (V)	Instantaneous Current (A)	Estimated Overall Cathode Voltage (V)	Estimated Overall Anode Voltage (V)	Estimated Contact Tip Voltage Loss (V)	Estimated Electrode Voltage Loss (V)	Estimated Arc Column Voltage Loss (V)	Estimated Instantaneous Voltage (V)
A	23.4	148	10.86	6.13	0.42	0.029	5.09	22.5
B	23.4	145	10.86	6.13	0.41	0.029	4.96	22.4
C	26.0	239	10.86	6.13	0.68	0.049	9.06	26.8
D	28.2	326	10.86	6.13	0.93	0.070	12.80	30.8
E	28.1	328	10.86	6.13	0.93	0.070	12.89	30.9
F	29.1	327	10.86	6.13	0.93	0.070	12.88	30.9
G	25.8	213	10.86	6.13	0.61	0.043	7.90	25.5
H	24.1	170	10.86	6.13	0.48	0.034	6.05	23.6

With knowledge of the thermophysical properties of the wire, overall anode fall voltage, electrode voltage, contact tip voltage loss, and droplet heat content, deposition rates can be calculated

as shown in Figure 4.11 [6]. These results correlate well with electrode diameters ≥0.045 inch. (1.143 mm) and begin to deviate at electrode diameters ≤0.035 inch. (0.89 mm) [6].

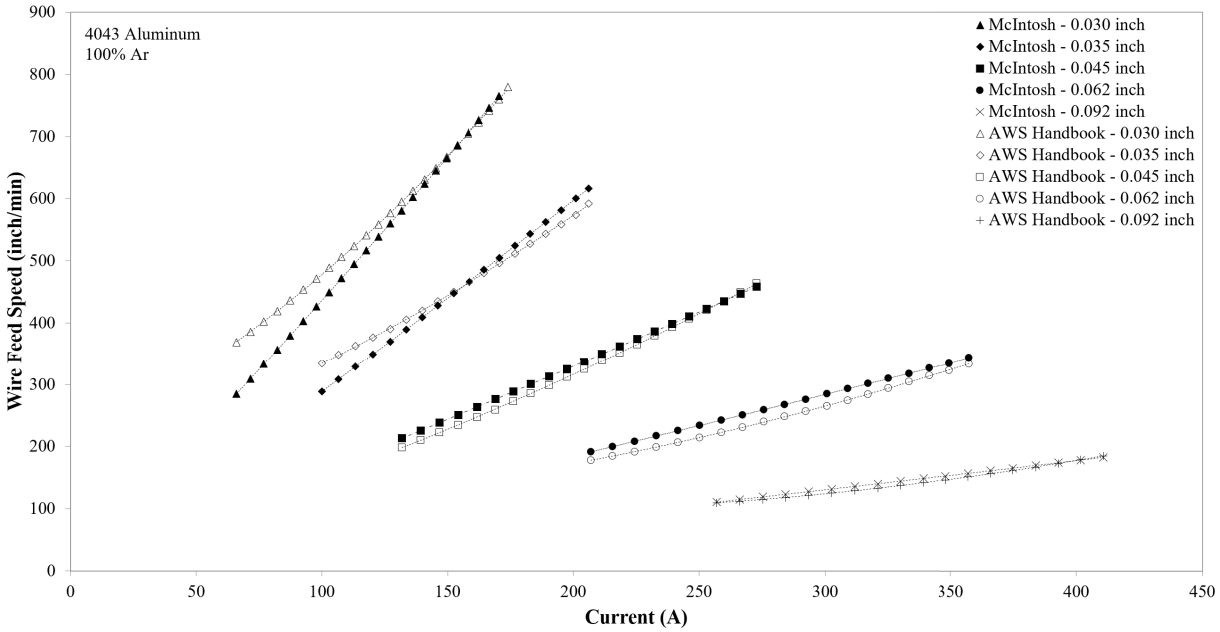

Fig. 4.11: Deposition rates of a 4043 electrode at various diameters for CV [6]. Deposition rates were determined with fall voltage values and droplet heat contents in Tables 4.3-4.4

4.5. Discussion

4.5.1. Cathode

Experiments utilizing pulse waveforms and high average currents were found to have MDPP and increased spatter. The increased deposition rates and Lorentz forces would cause an electromagnetic kink instability pushing a secondary droplet in undesired directions as spatter. This spatter would contaminate the cathode which inadvertently and artificially increased the cathode heat input. Attempts were made to remove this small amount of spatter after welding with no success. Spatter was found to be bonded to the cathode and could only be removed with abrasive materials. It was estimated that 0.5 g to 2.0 g was found on the cathode after a 30 second test. This amount of spatter would increase overall cathode fall voltage by approximately 0.4 V to 1.0 V.

Testing with nearly identical welding parameters yielded an average overall cathode fall voltage of 10.9 V and 12.7 V for aluminum and steel respectively when using identical equipment, shielding gas, and cathode material. As shown in Equation 4.1, the overall cathode fall voltage

should not be dependent on the anode material and should only be dependent on the cathode work function and thermal energy of the elections [16, 66, 79]. Shielding gas composition has been shown to affect overall anode and cathode fall voltage values when using identical electrodes and cathodes, but has yet to be fundamentally explained [79]. It is possible for the cathode to be contaminated with electrode condensation and spatter yielding a possible difference in the cathode work function of 0.13 V to 0.68 V, but is not significant enough to account for observed results.

Using an electron temperature of 6,000K, cathode sheath voltage was calculated to be on the order of 16.57 ± 0.76 V and 18.44 ± 0.88 V for aluminum and steel electrodes respectively [5]. These cathode sheath values should be nearly identical to each other. The temperature of an aluminum arc has shown to be substantially higher when compared to a carbon steel arc. Temperature measurements of the inner arc in aluminum GMAW and carbon steel GMAW are approximately 19,000 K and 7,000 K respectively [16, 25, 27, 33, 37, 68]. If the electron temperature is assumed to be the temperature of the inner arc, the cathode sheath voltage can be recalculated as 18.26 ± 0.76 V and 18.57 ± 0.88 V for aluminum and steel respectively. These recalculated values are substantially closer, are within standard deviations, and do not appear statistically different. These calculations indicate that the arc's temperature could be influencing overall cathode fall voltage.

4.5.2. Anode and Droplet Heat Content

The distance from the electrode tip to the top the calorimeter could be influencing droplet heat content [3, 34–36]. The calorimeter location was picked to minimize calorimeter heating from the welding arc while also minimizing droplet travel distance [2]. Numerous factors could be influencing droplet heat content including radiation, convection, and oxidation. Droplet interactions with the atmosphere and arc may be cooling or heating the droplet. Oxidation of the droplet was found to occur above the calorimeter leading to a slight increase in heat content but is likely negligible based on previous literature [97]. Prior work on the calorimetry setup suggests that the calorimeter distance does not affect measurements significantly as droplet temperatures are consistent with non-intrusive methods such as pyrometry [2, 4, 5].

When comparing similar measuring methods, overall anode fall voltage values were comparable with literature [18, 97, 98]. Overall anode fall voltage appeared to be dependent on waveform

selection at lower currents. At the transition region, vapourization rates in pulse waveforms have been shown to be lower and extending over a larger range of currents when compared to non-pulse waveforms [14]. The transition point for a 1.2 mm aluminum consumable is approximately 135 A [107]. The low current pulse experiments could be within the transition region and could have a lower amount of vapourization. With a lower amount of vapourization occurring for the same deposition rate, a higher amount of total anode energy is captured by the calorimetry system for these pulse waveforms. This implies that pulse waveforms will have a higher overall anode fall voltage when compared to non-pulse waveforms at these low currents. If more of the total anode energy input is captured by these low current pulse waveform experiments, these experiments will be a better representation of overall anode fall voltage as less energy is lost from metallic vapourization.

Metallic vapourization of the anode will cause cooling of the anode surface and will not be captured by the calorimetry system. Fume formation rates in a 4043 aluminum electrode is approximately 0.03 g/min to 0.35 g/min at 170 A [108]. If this vapourization mass loss is assumed to be all metallic aluminum and the droplet surface is assumed to be at boiling temperatures, evaporative heat losses will account for an increase of 0.04 V to 0.37 V in overall anode fall voltage and anode sheath voltage [15, 41]. As shown in Equation 4.2, vapourization of the electrode was not considered which lead to a low measurement of the overall anode fall voltage and anode sheath fall voltage. Vapourization rates will increase at higher currents decreasing the measured overall anode fall voltage at these currents.

As shown in Figure 4.6, the difference in the average overall anode fall voltage between aluminum and steel is approximately 1.3 V. Anode sheath voltage for an ER70S-6 steel electrode is believed to approximately -0.3 V when using an electron temperature of 6,000 K to 7,000 K and a work function of 4.10 V for pure manganese [92]. Pure manganese was used as the work function for ER70S-6 steel as cathode and anode spots have been shown to preferentially form at locations with a lower ionization potential [16]. Utilizing an electron temperature of 6,000 K and 19,000 K, average anode sheath voltage is on the order of 1.10 $\pm$ 0.24 V and -0.58 $\pm$ 0.24 V for a 4043 aluminum electrode. If evaporation is accounted for in both the ER70S-6 and 4043 electrodes, anode sheath voltage will increase by approximately 0.1 V to 0.5 V and is believed to be 0 V.

4.5.3. Thermal Efficiency

Thermal efficiency was within previously reported ranges but is slightly low [44, 55–58, 93, 105]. These previous measurements were performed by welding directly on a plate calorimeter giving no capability of separating between cathode and anode heat inputs. The higher surface area of a plate calorimeter will yield a higher thermal efficiency as the larger surface area can absorb more radiative heat from the arc column. The small surface area of the cathode in this study does not permit large amounts of radiative absorption leading to a lower overall thermal efficiency. Additionally, modelling of the energy distribution in GMAW indicates that thermal efficiency is 68% when the cathode and anode do not receive radiative energy from the arc [68]. This value is near identical to that found in this paper implying that a minimal amount of radiative energy was captured by the calorimetry system or that some energy was lost in experimentation.

Thermal efficiency appears to be affected by arc length as shown in Table 4.2. An increase in arc length resulted in more energy needed to properly ionize the arc [106]. The excess arc column energy is lost and is not captured by the calorimetry system.

4.5.4. Contact Tip

The tungsten bar measured contact tip voltage loss immediately after leaving the contact tip. A small amount of ohmic heating will take place before voltage measurements occur, but will be negligible in aluminum GMAW. Contact tip voltage loss was assumed to be proportional to current and independent from waveform selection. It is currently unclear what the affect of waveform selection has on contact tip voltage loss.

4.5.5. Electrode Extension

Average voltage loss by resistivity in the electrode extension was negligible compared to the other measurements. The resistivity of 4043 aluminum will be higher than pure aluminum because of additional alloying elements. By using the resistivity properties of pure aluminum in Lehnhoff's model, electrode extension resistance and voltage loss were slightly underestimated [7]. However, even if the resistivity properties of 4043 aluminum were used, the voltage loss will still be minimal compared to other measurements.

4.5.6. Arc Column

Approximately 13% to 33% of the total energy of the arc column is lost as radiative heat depending on welding parameters and arc length [16, 44, 93]. Some of this heat will contribute to heating of the cathode. This will lead to a slight underestimation of the arc column potential as the cathode will be slightly overestimated due to the increased radiative heat from the arc.

Temperature measurements of the inner arc in aluminum GMAW and carbon steel GMAW are approximately 19,000 K and 7,000 K respectively [16, 33, 37]. The higher arc temperatures in aluminum will require more joule heating to maintain proper ionization and temperatures when compared to carbon steel. This results in aluminum having a higher average arc column potential compared to steel.

4.5.7. Torch Cables

The two data acquisition systems took data during steady state but were not synchronized with each other. The unsynchronized data can result in variations for the pulse on pulse waveform as this waveform changes between a sharp and broad peak at a frequency of approximately 4 Hz. Since data was only accumulated for 2.8 seconds, voltage differences between these data acquisition systems can change based on when data was taken.

4.5.8. Aluminum Plate Welding and Detachment Frequency

Comparing droplet detachment frequency between the calorimeter and aluminum plate experiments yielded slight differences. A sufficiently long arc length appeared to be representative of metal transfer mode on the calorimeter but not a short arc length. There are slight variations in electrode extension and current in experimentation but are insignificant to change metal transfer. Ohmic heating has been shown to have negligible effects with varying electrode extension in aluminum welding. Small changes in current will not greatly influence metal transfer behavior with the exception of the transition between globular and spray metal transfer. Experimentation was well above the transition current as the transition point for a 1.2 mm aluminum consumable is approximately 135 A [107]. These results indicate that something besides Lorentz forces and surface tension are influencing metal transfer.

As shown in Figure 4.9, there appears to be a change in the plasma appearance between and

long and short arc. The high speed videography shows that the short arc may be interacting with the electrode above the solid-liquid interface. During droplet growth, the increasing metal vapour concentration below the droplet will change arcing behaviour as anode spots will begin to be preferentially located higher up the electrode. This effect may be increased in short arc lengths as the electrode approaches the impingement point of the weld pool. Interactions between the electrode, weld pool, and metal vapours could change current density over a larger and wider area leading to cathode spots being located farther away and anode spots located further up the electrode.

Fu observed a similar phenomenon which was described as the intrinsic self-regulating effect of arc length [97]. Arc roots were observed climbing up the electrode which would change overall heat input behavior and droplet heat content. This phenomenon was attributed to the difference between the electric field intensity of the arc column and the bottom of the electrode [97]. He noted that this phenomenon was much more apparent in 5356 aluminum possibly from the increased metallic vaporization of these consumables [102, 103]. These results suggest that further work is required exploring the behaviour of short and long arcs in aluminum GMAW.

4.5.9. Voltage and Deposition Estimation

When estimating overall voltage loss in the GMAW system, results are comparable with those found in experimentation. Estimations begin to deviate at higher currents and is likely from an overestimation at extrapolated values.

Arc length was considered to be constant during the analysis in Table 4.6 and Figure 4.10 based on the definition of arc length used in this paper. The pulse waveform in Figure 4.10 shows that the voltage increases by approximately 1.3 V during droplet detachment. A constant arc length does not capture this detachment event which contradicts the constant arc length methodology used in Table 4.6 and reconfirms that anode spots exist on the bottom of the droplet. This methodology of measuring arc length relies on the temperature differences between the inner and outer arc column. Welding with a 4043 electrode results in a relatively high inner arc column temperature of 19,000 K leading to increased current density at the bottom of the droplet [16, 33, 37]. Electrodes with higher vapourization rates will benefit more from this definition of arc length as they are less likely to see a voltage increase during droplet detachment. These results confirm the difficulty of characterizing arc length with a single parameter.

As shown in Figure 4.11, results correlate well with larger diameter electrodes indicating that the measurements of overall anode fall voltage are correct. Deposition rates begin to deviate at smaller diameter electrodes. Extrapolation of literature curves indicate that deposition rates of ≥200 inch/min (84.7 mm/s) are achieved at 0 A with smaller diameter electrodes [6]. Deposition rates should be 0 inch/min at 0 A. The empirical values used to generate the literature curve could have had additional unconsidered factors affecting deposition rates but is currently unclear [6].

4.6. Conclusions

A solid state calorimeter and a water cooled cathode were used to determined energy partitions in aluminum GMAW with a 1.2 mm (3/64 in.) 4043 electrode. Fall voltage, thermal efficiency, and droplet heat content were determined for five waveforms including CV, constant power, pulse, CC pulse, and pulse on pulse. Experimental decisions and parameters were selected primarily for their relation to typical welding systems allowing greater insight into the aluminum GMAW system.

Overall cathode fall voltage was 10.86 ± 0.8 V and independent from current. This is believed to be the first time that overall cathode fall voltage was determined for an aluminum GMAW system. Based on prior steel experimentation, overall cathode fall voltage results are 1.8 V lower than expected based on the work functions of aluminum and steel. These results suggest that overall cathode fall voltage may be dependent on the arc's temperature and will need to be considered in future work. Overall anode fall voltage was 6.13 ± 0.24 V, independent on current, dependent on waveform selection, and was comparable with previous literature. Pulse waveforms were shown to have a slightly higher anode fall voltage at lower currents possibly from a lower amount of vapourization. Droplet temperature ranged between 1812 °C and 2139 °C with an average thermal efficiency of 68.1 ± 4.8 %. Both droplet temperature and thermal efficiency appeared to be dependent on waveforms but variations were not statistically significant at the currents tested. Average contact tip voltage loss and resistance was measured to be 0.56 ± 0.10 V and 2.85 ± 0.54 $m\Omega$ respectively. Utilizing the work of Lehnhoff, average electrode extension voltage loss was 0.06 ± 0.01 V and was insignificant compared to other measurements. Arc column fall voltage potential was 0.77 ± 0.19 V/mm and appeared to be dependent on current. Average voltage loss through the torch cable/leads was 1.60 ± 0.36 V

and will depend on torch/cable dimensions and design.

The trends found in these various voltage loss regions gave the capability of measurement total voltage loss and deposition rates at any current. Voltage loss predictions were found to be reasonable at tested currents but begin to deviate at extrapolated values. Calculated deposition rates were very comparable with empirical values and indicate that values of anode fall voltage are correct. Comparative tests between the calorimetry setup and an aluminum plate indicate that the calorimeter is representative of metal transfer mode when arc length is sufficiently large. Welding with short arc lengths were shown to have a slower detachment freqeuncy and a different plasma appearance.

The experiments performed in this study gave consistent measurements and were representative of typical aluminum GMAW welding parameters. The results will assist future models to determine deposition rates, heat input, and fume emission for varying current, waveform, and polarity giving a more complete understanding of the aluminum GMAW system.

5. Conclusions and Future Work

5.1. Conclusions and Summary Findings

Cathode and anode energy partitions were concurrently measured in GMAW, giving increased insight and prediction capabilities. Utilizing a solid state calorimeter and water cooled cathode, fall voltages and droplet temperatures associated with a 1.143 mm ER70S-6 carbon steel and 1.2 mm 4043 aluminum consumable were tested as a function of current. Different types of Ar - CO_2 shielding gases were utilized within steel experimentation. Different waveforms were selected during aluminum testing including CV, constant power, pulse, CC pulse, and pulse on pulse waveforms. Both steel and aluminum experiments were performed over a range of currents. Secondary voltage losses at the contact tip and electrode stickout were measured with a tungsten probe and determined with Lehnhoff's model respectively.

Droplet temperatures were found for a 1.143 mm ER70S-6 carbon steel electrode utilizing 100% Ar, 5% CO_2 - 95% Ar, and 10% CO_2 - 90% Ar shielding gases. Temperatures ranged between 2000 °C and 2700 °C with a temperature minimum at the transition point between spray and globular metal transfer. Increasing amounts of CO_2 were shown to shift this temperature minimum to higher current levels while maintaining a similar droplet temperature curve. Results suggest that at any given current, shielding gas composition can be finely adjusted to give a minimum in droplet temperature and fume emission while maintaining deposition rates.

Overall cathode and anode fall voltage measurements were concurrently inferred for a 1.143 mm ER70S-6 carbon steel electrode utilizing 100% Ar and 5% CO_2 - 95% Ar shielding gas. Overall cathode fall voltage was independent from current and averaged at 12.7 V and 15.5 V for 100% Ar and 5% CO_2 - 95% Ar respectively. This is believed to be the first time that cathode fall voltage was experimentally verified to be independent from current. Spatter associated with increasing amounts of CO_2 shielding gas caused large variations in the 5% CO_2 - 95% Ar experiments. Overall anode fall voltage was independent of current and averaged at 4.7 V and 4.5 V for 100% Ar and 95% Ar - 5% CO_2 respectively. Metal transfer did not appear to significantly change the anode fall voltage. Anode sheath voltage was determined to be on the order of -0.89 V and -1.05 V for 100% Ar and 95% Ar - 5% CO_2 respectively. If the work function of pure manganese was used and evaporation considered, anode sheath voltage

is believed to be closer to 0. Average contact tip voltage loss and resistance was 0.49 V and 2.16 $m\Omega$ respectively for both shielding gases. Electrode extension voltage loss averaged at 2.17 V and 2.34 V for 100% Ar and 95% Ar - 5% CO_2 respectively utilizing a model produced by Lehnhoff. Arc column potential averaged at 0.77 V/mm and appeared to be dependent on current when using 100% Ar. Arc column potential trends associated with 95% Ar - 5% CO_2 shielding gas could not be concluded as variations were within experimental error.

Fall voltage measurements were concurrently inferred for a 1.2 mm 4043 aluminum electrode utilizing CV, constant power, pulse, CC pulse, and pulse on pulse waveforms. Overall cathode fall voltage averaged at 10.4 V, was independent from current, and it may be the first time cathode fall voltage measurements were made with an aluminum electrode. Comparing the CV steel and aluminum electrode results, the difference in overall cathode fall voltages was 1.8 V when using an identical cathode, power supply, and shielding gas. These results suggest that anode vapourization could be changing the arcs composition, temperature and overall cathode fall voltage. Average overall anode fall voltage was 6.13 V, was independent of current, and slightly dependent on waveform selection. Pulse waveforms were shown to have a slightly higher anode fall voltage at lower currents possibly from a lower amount of vapourization. Average contact tip voltage loss and resistance was 0.56 V and 2.85 $m\Omega$ respectively. Average electrode extension voltage loss was 0.06 V and was insignificant compared to other measurements. Average arc column fall voltage potential was 0.77 V/mm and appeared to be dependent on current. Voltage loss predictions in pulse aluminum GMAW were found to be comparable in the current ranges tested but begin to deviate at extrapolated values. Calculated deposition rates were comparable with other literature indicating that the value of anode fall voltage is correct.

The experiments performed in this thesis gave consistent measurements and were representative of typical GMAW welding parameters. The inferred fall voltages found in both steel and aluminum can be used to predict total voltage loss, depositions rates, heat inputs, and vapourization rates for varying current, waveform, and polarity giving a more complete understanding of the aluminum GMAW system.

5.2. Future Work

- Droplet temperature measurements were comparable with non-intrusive techniques utilized in other literature. Properly determining the amount of heat gained or lost before

landing on the calorimeter will help validate the experimental setup. This work has been started in the Appendix C but is still incomplete.

- Overall anode fall voltage measurements found did not account for vapourization at the anode surface. The amount of vapourization can be substantial in streaming spray transfer resulting in significant anode cooling. Properly determining vapourization rates in conjunction with other results will allow heat loss at the anode surface to be calculated.
- Experimental work has shown that overall cathode fall voltage may be dependent on plasma composition and temperature. Experimentation with different amounts of Mn in steel will change the amount of Mn vapourization and should change arc temperature, arc column potential, overall cathode fall voltage, and overall anode fall voltage. Testing with a pure iron electrode and a high Mn (>2 wt%) electrode is recommended.
- Experimental measurements were performed over a narrow current range. Experimentation over a wider range of currents and metal transfer modes will reduce the amount of extrapolation required increasing prediction accuracy.

6. References

[1] Chapuis, J., K. M. Scott, S. Guest, E. J. Soderstrom, and P. F. Mendez (2012). Droplet Calorimetry and High Speed Videography Of Free Flight Metal Transfer in Gas Metal Arc Welding. *CWA Journal*.

[2] Scott, K. M. (2011). Heat Transfer and Calorimetry of Tubular Ni/WC Wires Deposited with GMAW. MSc. Thesis. University of Alberta.

[3] Soderstrom, E. J. (2009). *Gas Metal Arc-Welding Electrode Heat-and-Mass Transfer Mechanisms*. Ph. D. thesis, Colorado School of Mines.

[4] McIntosh, C., J. Chapuis, and P. F. Mendez (2016). Effect of Ar-CO2 Gas Blends on Droplet Temperature in GMAW. *Welding Research Supplement 95*(8), 273s–279s.

[5] McIntosh, C. and P. F. Mendez (2017). Experimental Measurements of Fall Voltages in Gas Metal Arc Welding. *Welding Research Supplement*.

[6] American Welding Society (2001). *Welding Handbook - Welding Processes, Part 1* (9th ed.), Volume 2.

[7] Lehnhoff, G. R. and P. F. Mendez (2011). Scaling of Non-Linear Effects in Heat Transfer of a Continuously Fed Melting Wire. *International Journal of Heat and Mass Transfer 54*(11-12), 2651–2660.

[8] Guest, S. (2014). *Depositing Ni-WC Wear Resistant Overlays with Hot-Wire Assist Technology*. Ph. D. thesis, University of Alberta.

[9] Murphy, A. B. and C. J. Arundell (1994). Transport coefficients of argon, nitrogen, oxygen, argon-nitrogen, and argon-oxygen plasmas. *Plasma Chemistry and Plasma Processing 14*(4), 451–490.

[10] Murphy, A. B. (1995). Transport coefficients of air, argon-air, nitrogen-air, and oxygen-air plasmas. *Plasma Chemistry and Plasma Processing 15*(2), 279–307.

[11] Murphy, A. B. (1997). Transport Coefficients of Helium and Argon-Helium Plasmas. *IEEE Transactions on Plasma Science 25*(5), 809–814.

[12] Murphy, A. B. and E. Tam (2014). Thermodynamic properties and transport coefficients of arc lamp plasmas: argon, krypton and xenon. *Journal of Physics D: Applied Physics 47*(29), 295202.

[13] Lide, D. R. (2003). *Handbook of Chemistry and Physics* (84th ed.).

[14] Quimby, B. J. and G. D. Ulrich (1999). Fume Formation Rates in Gas Metal Arc Welding. *Welding Research Supplement* (April), 142–149.

[15] Dean, J. A. (1999). *Lange's Handbook of Chemistry* (15th ed.). McGraw Hill, New York.

[16] Lancaster, J. F. (1984). *The Physics of Welding* (Second ed.).

[17] Correy, T. B. (1982). *What Makes an Electric Welding Arc Perform its Required Functions*. Pacific Northwest Laboratory, U.S. Department of Energy.

[18] Nemchinsky, V. A. (1994). Plasma Parameters Near a Small Anode in a High-Pressure Arc (Gas Metal Arc Welding). *Journal of Chemical Information and Modeling 53*, 160.

[19] Mendez, P. F., N. T. Jenkins, and T. W. Eagar (2000). Effect of Electrode Droplet Size on Evaporation and Fume Generation in GMAW. In *Proceedings of the Gas Metal Arc Welding for the 21st Century*, Miami. American Welding Society.

[20] Deam, R. T., S. W. Simpson, and J. Haidar (2000). A Semi-Empirical Model of the Fume. *Journal of Physics D: Applied Physics 1393*.

[21] Bosworth, M. R. and R. T. Deam (2000). Influence of GMAW Droplet Size on Fume Formation Rate. *Journal of Physics D: Applied Physics 33*, 2605–2610.

[22] Bingul, Z., G. E. Cook, and a. M. Strauss (2001). Dynamic model for electrode melting rate in gas metal arc welding process. *Science and Technology of Welding and Joining 6*(1), 41–50.

[23] Wang, F., W. K. Hou, S. J. Hu, E. Kannatey-Asibu, W. W. Schultz, and P. C. Wang (2003). Modelling and Analysis of Metal Transfer in Gas Metal Arc Welding. *Journal of Physics D: Applied Physics 36*, 1143–1152.

[24] Pires, I., L. Quintino, and R. M. Miranda (2007). Analysis of the Influence of Shielding Gas Mixtures on the Gas Metal Arc Welding Metal Transfer Modes and Fume Formation Rate. *Materials and Design 28*(5), 1623–1631.

[25] Schnick, M., U. Füssel, M. Hertel, A. Spille-Kohoff, and A. B. Murphy (2009). Metal Vapour Causes a Central Minimum in Arc Temperature in Gas Metal Arc Welding Through Increased Radiative Emission. *Journal of Physics D: Applied Physics 43*, 022001.

[26] Murphy, A. B. (2010). The Effects of Metal Vapour in Arc Welding. *Journal of Physics D: Applied Physics 43*(43), 434001.

[27] Schnick, M., U. Fuessel, M. Hertel, M. Haessler, A. Spille-Kohoff, and A. B. Murphy (2010). Modelling of Gas-Metal Arc Welding Taking into Account Metal Vapour. *Journal of Physics D: Applied Physics 43*, 434008.

[28] Pfender, E. and J. Heberlein (2007). Heat Transfer Processes and Modeling of Arc Discharges. *Advances in Heat Transfer 40*, 345–450.

[29] Dennis, J. H., P. J. Hewitt, C. A. Redding, and D. Workman (2001). A Model for Prediction of Fume Formation Rate in Gas Metal Arc Welding (GMAW), Globular and Spray Modes, DC Electrode Positive. *The Annals of occupational hygiene 45*(2), 105–113.

[30] Pires, I., L. Quintino, R. M. Miranda, and J. F. P. Gomes (2006). Fume Emissions during Gas Metal Arc Welding. *Toxicological & Environmental Chemistry 88*(3), 385–394.

[31] Jenkins, N. T., P. F. Mendez, and T. W. Eagar (2005). Effect of Arc Welding Electrode Temperature on Vapor and Fume Composition. *Trends in Welding Research, Proceedings of the 7th International Conference*.

[32] Mohan, S., S. P. Sivapirakasham, P. Bineesh, and K. K. Satpathy (2014). Strategies for Controlling Welding Fumes at the Source - A Review. *Applied Mechanics and Materials 592-594*, 2539–2545.

[33] Haidar, J. (1999). An Analysis of Heat Transfer and Fume Production in Gas Metal Arc Welding. III. *Journal of Applied Physics 85*(7), 3448–3459.

[34] Pokhodnya, I. K. and A. M. Suptel (1967). The Heat Contents of the Droplets of Electrode Metal in Gas Shielded Arc Welding. *Avtomat. Svarka* (No 2), 19–21.

[35] Ozawa, M. and T. Morita (1963). The Measurement of Heat Quantity in Melted Metals. *Journal of the Japan Welding Society 32*, 52–59.

[36] Ando, K. and K. Nishiguchi (1969). Mechanism of Formation of Pencil-Point-like Wire Tip in MIG Arc Welding. In *IIW Doc. 212-156-68*. International Institute of Welding.

[37] Acinger, K., L. Sipek, and E. Smars (1970). Temperature, Metal Vapour Density, and Energy Balance in an Argon Shielded Welding Arc with Iron Electrodes. *Electron Physics Divison: Stockholm*.

[38] Jelmorini, G., G. W. Tichelaar, and G. J. P. M. Van Den Heuvel (1977). Droplet Temperature in Arc Welding. In *IIW Doc. 212-411-77*. International Institute of Welding.

[39] Halmoy, E. (1979). Wire Melting Rate, Droplet Temperature, and Effective Anode Melting Potential. In *Arc Physics and Weld Pool Behaviour*, London, UK, pp. 49–59. The Welding Institute.

[40] Hu, J. and H. L. Tsai (2007). Heat and Mass Transfer in Gas Metal Arc Welding. Part II: The Metal. *International Journal of Heat and Mass Transfer 50*(5-6), 808–820.

[41] Tanaka, M., K. Waki, S. Tashiro, K. Nakata, E. Yamamoto, K. Yamazai, and K. Suzuki (2009). Visualizations

of 2D Temperature Distribution of Molten Metal in Arc Welding Process. *Transactions of JWRI 38*(2), 1–4.

[42] Yamazaki, K., E. Yamamoto, K. Suzuki, F. Koshiishi, K. Waki, S. Tashiro, M. Tanaka, and K. Nakata (2010). The Measurement of Metal Droplet Temperature in GMA Welding by Infrared Two-Colour Pyrometry. *Welding International 24*(2), 81–87.

[43] Siewert, E., J. Schein, and G. Forster (2013). Determination of Enthalpy, Temperature, Surface Tension and Geometry of the Material Transfer in PGMAW for the System Argon-Iron. *Journal of Physics D: Applied Physics 46*(22), 224008.

[44] Haelsig, A., M. Kusch, and P. Mayr (2015). Calorimetric Analyses of the Comprehensive Heat Flow for Gas Metal Arc Welding. *Welding in the World 59*(2), 191–199.

[45] Soderstrom, E. J., K. M. Scott, and P. F. Mendez (2011). Calorimetric Measurement of Droplet Temperature in GMAW. *Welding Journal 90*(4), 77S–84S.

[46] Iordachescu, D. and L. Quintino (2008). Steps Toward a New Classification of Metal Transfer in Gas Metal Arc Welding. *Journal of Materials Processing Technology 202*(1-3), 391–397.

[47] Yamazaki, K., E. Yamamoto, K. Suzuki, and F. Koshiishi (2007). In-Situ Measurement of Metal Droplet Temperature in Gas Metal Arc Welding by Two-Color Pyrometry. *International Institute of Welding*, Doc. 212–1103–07.

[48] Zielinska, S., S. Pellerin, F. Valensi, K. Dzierzega, K. Musiol, C. de Izarra, and F. Briand (2008). Gas Influence on the Arc Shape in MIG-MAG Welding. *The European Physical Journal Applied Physics 43*(1), 111–122.

[49] Zielinska, S., K. Musiol, K. Dzierżęga, S. Pellerin, F. Valensi, C. de Izarra, and F. Briand (2007). Investigations of GMAW Plasma by Optical Emission Spectroscopy. *Plasma Sources Science and Technology 16*(4), 832–838.

[50] Mills, K. C. (2002). Recommended Values of Thermophysical Properties for Selected Commercial Alloys. Woodhead Publishing Ltd and ASM International.

[51] Baker, B. H., N. Crevis, J. A. Lucey, and F. W. Lunau (1961). Mild Steel Welding with Argon/CO2 Mixtures. *British Welding Journal April*.

[52] Haidar, J. and J. Lowke (1997). Effect of CO2 Shielding Gas on Metal Droplet Formation in Arc Welding. *IEEE Transactions on Plasma Science 25*(5), 931–936.

[53] Wang, H. X., W. P. Sun, S. R. Sun, A. B. Murphy, and Y. Ju (2014). Two-temperature chemical-nonequilibrium modelling of a high-velocity argon plasma flow in a low-power arcjet thruster. *Plasma Chemistry and Plasma Processing 34*(3), 559–577.

[54] Nemchinsky, V. A. (1996). The Effect of the Type of Plasma Gas on Current Constriction at the Molten Tip of an Arc Electrode. *Journal of Physics D: Applied Physics 29*, 1202–1208.

[55] Herschel, S. B. (1993). Transfer of Heat and Mass to the Base Metal in Gas Metal Arc Welding. *ASM Handbook Volume 6*, 25–29.

[56] Dupont, J. N. and A. R. Marder (1995). Thermal Efficiency of Arc Welding Processes. *Welding Research Supplement* (December), 406s–416s.

[57] Pépe, N., S. Egerland, P. A. Colegrove, D. Yapp, A. Leonhartsberger, and A. Scotti (2011). Measuring the Process Efficiency of Controlled Gas Metal Arc Welding Processes. *Science and Technology of Welding and Joining 16*(5), 412–417.

[58] Joseph, A., D. Harwig, D. F. Farson, and R. Richardson (2003). Measurement and Calculation of Arc Power and Heat Transfer Efficiency in Pulsed Gas Metal Arc Welding. *Science and Technology of Welding*

and Joining 8(6), 400–406.

[59] Hälsig, A. (2014). *Energetic Accounting for Arc Welding Processes*. Ph. D. thesis, Chemnitz University of Technology.

[60] Busz-Peuckert, G. and W. Finkelnburg (1956). For Anode Mechanism of Thermal Argon Arc. *für physik*, 244–251.

[61] Wilkinson, J. B. and D. R. Milner (1960). Heat Transfer From Arcs. *British Welding Journal*, 115–128.

[62] Quigley, M. B. C., P. H. Richards, D. T. Swift-Hook, and A. E. F. Gick (1973). Heat Flow to the Workpiece From a TIG Welding Arc. *Journal of Physics D: Applied Physics 6*(18), 2250–2258.

[63] Yokomizu, Y., T. Matsumura, R. Henmi, and Y. Kito (1996). Total Voltage Drops in Electrode Fall Regions of SF6, Argon and Air Arcs in Current Range from 10 to 20 000 A. *Journal of Physics D: Applied Physics 29*(5), 1260–1267.

[64] Hemmi, R., Y. Yokomizu, and T. Matsumura (2003). Anode-Fall and Cathode-Fall Voltages of Air Arc in Atmosphere Between Silver Electrodes. *Journal of Physics D: Applied Physics 36*(9), 1097–1106.

[65] Heberlein, J., J. Mentel, and E. Pfender (2010). The Anode Region of Electric Arcs: a Survey. *Journal of Physics D: Applied Physics 43*(2), 023001.

[66] Jonsson, B. Y. P. G. (1995). The Influence of Oxygen Additions on Argon-Shielded Gas Metal Arc Welding Processes. *Welding Research Supplement* (February), 48–58.

[67] Nemchinsky, V. A. (1998). Heat Transfer in an Electrode During Arc Welding with a Consumable Electrode. *Journal of Physics D: Applied Physics 31*(6), 730–736.

[68] Schnick, M., M. Hertel, U. Fuessel, and D. Uhrlandt (2013). Energy Balance in MIG Arcs. *Journal of Physics D: Applied Physics 46*.

[69] Slepian, J. (1926). Theory of Current Transference at the Cathode of an Arc. *Physical Review 27*(4), 407–412.

[70] Stark, J., T. Retschinsky, and A. Schaposchnikoff (1905). Studies on the Arc. *Annalen Der Physik 18*(212), 213–251.

[71] Langmuir, I. and H. Mott-Smith (1924). Studies of Electric Discharges in Gases at Low Pressures. *General Electric Review*.

[72] Mott-Smith, H. M. and I. Langmuir (1926). The Theory of Collectors in Gaseous Discharges. *Physical Review 28*(4), 727–763.

[73] Nottingham, W. B. (1928). Probe Neasurements in the Normal Electric Arc. *Journal of the Franklin Institute 206*(1), 43–55.

[74] Mackeown, S. S. (1929). The Cathode Drop in an Electric Arc. *Physical Review 34*(4), 611–614.

[75] Lamar, E. S. and K. T. Compton (1931). Potential Drop and Ionization at Mercury Arc Cathode. *Physical Review 37*(9), 1069–1076.

[76] Mason, R. C. (1931). The Cathode Fall of an Arc. *Physical Review 38*(1929).

[77] Pfender, E. (1980). Energy Transport in Thermal Plasmas. *Pure and Applied Chemistry 52*, 1773–1800.

[78] Waszink, J. H. and G. J. P. M. Van Den Heuvel (1982). Heat Generation and Heat Flow in the Filler in GMA Welding. *Welding Journal 61*(8), 269–280.

[79] Hajossy, R. and I. Morva (1994). Cathode and anode falls of arcs with fusible electrodes. *Journal of Applied Physics 27*, 2095–2101.

[80] Nemchinsky, V. A. (2003). Current Density at the Refractory Cathode of a High-Current High-Pressure Arc (Two Modes of Cathode Spot Attachment). *Journal of Physics D: Applied Physics 36*, 3007–3013.

[81] Hamilton, D. J. and A. E. Guile (1968). Ionization in the Cathode-Fall Region of Moving Arcs. *British Journal of Applied Physics 1*, 335–342.

[82] Huismann, G. (2016). Melting behaviour of wire electrodes acting as cathodes or anodes in GMAW. *Trends in Welding Research*, 1–7.

[83] Waszink, J. H. and G. J. P. M. Van Den Heuvel (1979). Measurements and Calculations of the Resistance of the Wire Extension in Arc Welding. In *The Welding Institute, Int. Conf. Arc Physics and Weld Pool Behaviour*, pp. 227–239.

[84] Luijendijk, T., J. D. de Zeeuw, and M. P. Sipkes (1996). Calculation of the Electrical Resistance Between Contact Tube and Welding Wire During GMA Welding Based on Measurement of the Contact Force. *International Journal for the Joining of Materials*.

[85] Wilson, L. J., G. E. Claussen, and C. E. Jackson (1956). The Effect of I2R Heating on Electrode Melting Rate. *Welding Research Supplement*, 1s – 8s.

[86] Lesnewich, A. (1958). Control of Melting Rate and Metal Transfer in Gas-Shielded Metal-Arc Welding Part I Control of Electrode Melting Rate. *Welding Journal 37*(8), 343–353.

[87] Halmoy, E. (1990). Current-Voltage Process Characteristics in Gas Metal Arc Welding. *International Institute of Welding*, Doc. 212–773–90.

[88] Liley, P. E. (2005). Thermophysical Properties of Ice/Water/Steam from -20C to 50C. *International Journal of Mechanical Engineering Education 32*(4), 45–50.

[89] White, G. and M. L. Minges (1997). Thermophysical Properties of Some Key Solids: An Update. *International Journal of Thermophysics 18*(5).

[90] Heberlein, J. V. and E. Pfender (1977). Investigation of the Anode Boundary Layer of an Atmospheric Pressure Argon Arc. *IEEE Transactions on Plasma Science 5*(3), 171–180.

[91] Nemchinsky, V. A. and L. N. Peretts (1977). Anode Sheath in a High-Pressure, High-Current Arc. *Soviet Physics. Technical Physics 22*.

[92] Haynes, W. M. (2011). *CRC Handbook of Chemistry and Physics* (95th ed.).

[93] Haelsig, A. and P. Mayr (2013). Energy Balance Study of Gas-Shielded Arc Welding Processes. *Welding in the World 57*(5), 727–734.

[94] Shimizu, H., K. Itoh, N. Masaie, T. Kurokawa, and M. Ushio (2006). Feedability of wires during metal active gas welding. *Science and Technology of Welding and Joining 11*(1), 81–93.

[95] Kim, Y. S. and T. W. Eagar. (1993). Metal Transfer in Pulsed Current Gas Metal Arc Welding. *Welding Journal 72*(July), 279–287.

[96] Praveen, P., M. J. Kang, and Y. K. D. V. Prasad (2006). Behaviour Of Metal Transfer Modes In Pulse Gas Metal Arc Welding Of Aluminum. In *Advanced Materials Processing Technologies Conference*.

[97] Fu, X.-S., M. Ushio, and F. Matsuda (1983). Melting Characteristics of Some Steel and Aluminum Alloy Wires in GMA Welding. *Japanese Welding Research Institute 12*, 167–173.

[98] Lu, M. J. and S. Kou (1989). Power Inputs in Gas Metal Arc Welding of Aluminum - Part 1. *Welding Journal* (September), 382s–388s.

[99] Chen, F. F. (1984). *Introduction to Plasma Physics and Controlled Fusion* (Second ed.).

[100] Huismann, G. (2013). Arc voltages on the GMAW process with and without current pulse, estimation of the dynamics for argon 18%CO2 shielding gas. In *IIW Doc.212-1287-13*. International Institute of Welding.

[101] Egerland, S. (2015). A Contribution to Arc Length Discussion. *Soldagem & Inspecao 20*(3), 367–380.

[102] Woods, R. A. (1979). Metal Transfer in Aluminium Alloys. *Welding Journal 02*, 59–66.

[103] Reisgen, U., O. Mokrov, A. Zabirov, I. Krivtsun, V. Demchenko, O. Lisnyi, and I. Semenov (2013). Task of volumetrical evaporation and behaviour of droplets in pulsed MIG welding of AlMg alloys. *Welding in the World 57*(4), 507–514.

[104] Maruo, H. (1984). Heat Contents and Temperature of Metal Droplets in Pulsed MIG Welding. *Japan Welding Society 2*, 573–578.

[105] Lu, M. J. and S. Kou (1989). Power Inputs in Gas Metal Arc Welding - Part 2. *Welding Journal* (November), 452s–456s.

[106] Bosworth, M. R. (1991). Effective Heat Input in Pulsed Current Gas Metal Arc Welding with Solid Wire Electrodes. *Welding Journal* (5).

[107] Lowke, J. J. (2009). Physical basis for the transition from globular to spray modes in gas metal arc welding. *Journal of Physics D: Applied Physics 42*, 135204.

[108] Castner, H. R. (1996). Fume Generation Rates for Stainless Steel, Nickel and Aluminum Alloys. *Welding Research Supplement 75*(12), 393s–401s.

[109] McBride, B. J., S. Gordon, and M. A. Reno (2001). Thermodynamic Data for Fifty Reference Elements. *Nasa Technical Paper 3287/Rev1*.

[110] Mendez, P. F., M. A. Ramirez, G. Trapaga, and T. W. Eagar (2001). Order-of-Magnitude Scaling of the Cathode Region in an Axisymmetric Transferred Electric Arc. *Metallurgical and Materials Transactions B 32B*(June), 547–554.

Appendix A: Experimental Equipment

This appendix will provide a more complete outline of the equipment used but will have repeated information from sections 2.2 and 3.3. The calorimeter itself was heavily developed by Scott who designed, tested, and calibrated the experimental setup [2]. This appendix will attempt to emphasize equipment that was different from Scott while still giving a complete understanding of the setup. For a detailed breakdown of the calorimeter only, see the work of Scott [2].

A.1. Calorimeter

A solid state ultra-high purity copper calorimeter was used to measure the droplet heat content. The calorimeter dimensions were: height of 35 mm (1.38 in.), diameter of 50.8 mm (2 in.), and positioned 127 mm (5 in.) below the water cooled copper cathode. The position of the calorimeter was intended to minimize heat input from arc radiation and minimize droplet travel distance. A distance of 127 mm (5 in.) was chosen based on the work of Ozawa, Ando, Jelmorini and Lu [35, 36, 38, 98]. A solid state calorimeter was more desired than a water based calorimeters as there is no error associated with water evaporation [2].

Initial setup on the calorimeter assumed that there would be a thermal gradient present in the calorimeter [2]. This thermal gradient would complicate calculations as enthalpy would become time dependent. 10 Omega GKQSS-18G-12 K type thermocouples were used to measure the temperature change of the calorimeter and were specifically placed throughout the calorimeter for use of a second order polynomial [2]. The location of these thermocouples allowed the user to determine the thermal gradient in the calorimeter allowing for more precise calculations. Repeated testing has shown that the thermal gradient in the calorimeter is not significant compared to the thermal contact resistance between the droplet and calorimeter. The calorimeter was surrounded with insulating material to maintain an adiabatic system as the thermal boundary layers equalized. Thermocouple data was taken at 10 Hz. The locations of these thermocouples is shown in Figure A.1 and had a heating and cooling cycle as shown in Figure A.2.

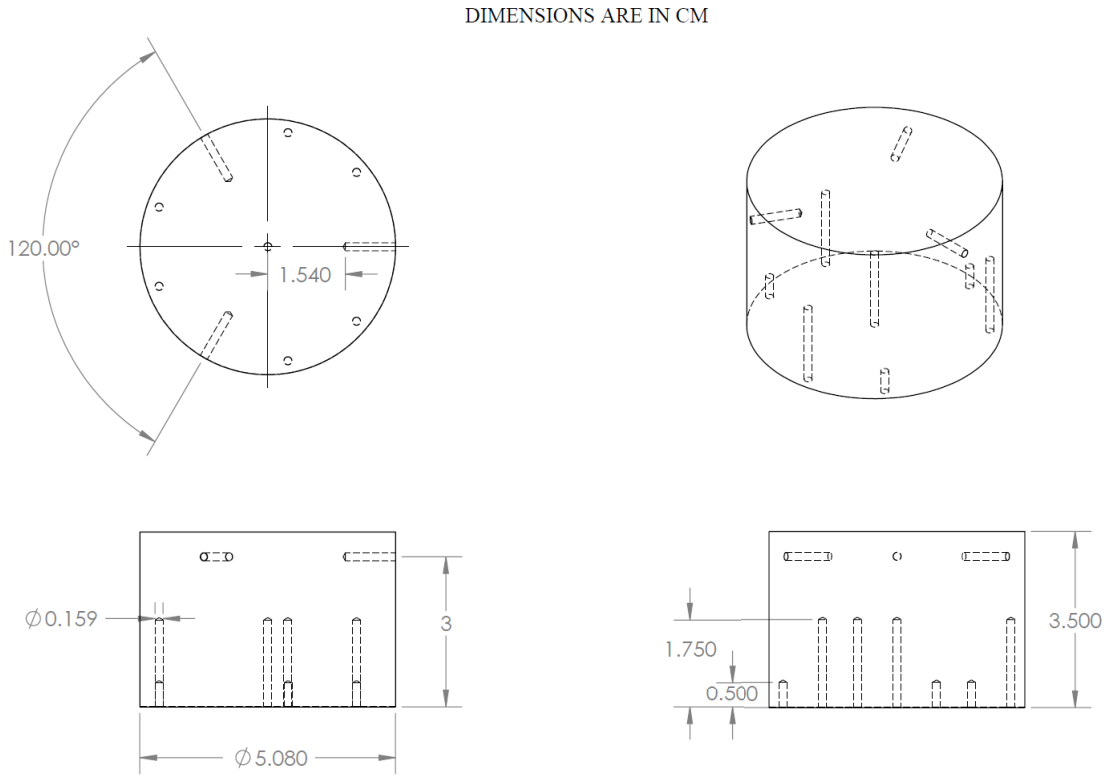

Fig. A.1: Placement of thermocouples on calorimeter [2].

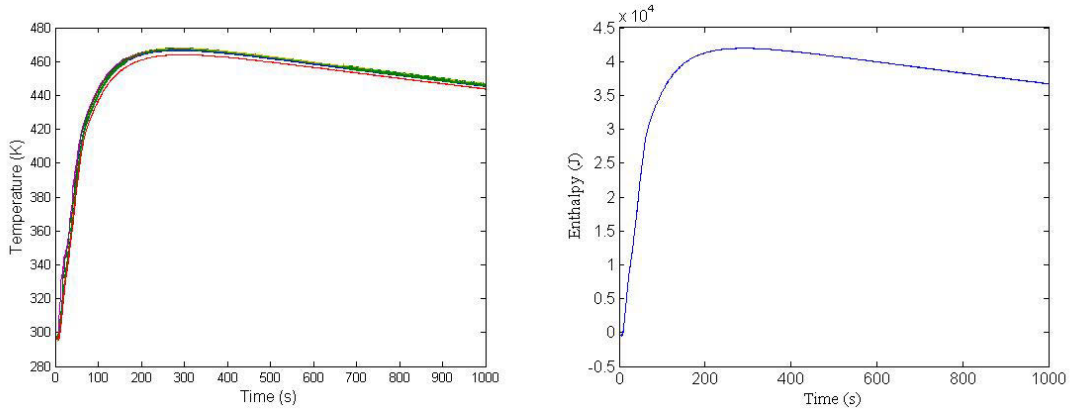

Fig. A.2: Temperature increase and decrease of thermocouples. Data was collected for 1000 s to determine how adiabatic the system was.

The calorimeter was calibrated utilizing liquid tin at a known temperature. The thermophysical properties of pure tin are well tabulated and were used to determine the accuracy of the calorimeter [109]. A linear function was used in order to improve accuracy as outlined by Scott [2]. After calibration, enthalpy measurements varied by ± 1.1% when the final calorimeter temperature was kept below 187 °C (368.6 °F) [2].

Droplets that fell onto the calorimeter were weighed using an Adam PGW 4502e scale to an

accuracy of ± 0.01 g (0.0022 lbs). Properties of pure copper and pure iron were used for the calorimeter and wire respectively [50, 89]. The properties were used to determine overall enthalpy of both the calorimeter and droplets as outlined in section E.1.

A.2. Copper Cathode

The purpose of the water cooled copper cathode was to maintain an arc during experimentation without melting. The copper cathode was designed to allow passage of liquid droplets from the electrode to the calorimeter as shown in Figure A.3.

Fig. A.3: Copper cathode used in experimentation

The hole of the copper cathode was approximately 10 mm (0.39 in.) in diameter. Water is capable of flowing through the copper cathode without interference. 2 Omega GKQSS-18G-12 K type thermocouples were used to measure the inlet and outlet temperature of the water at 10 Hz with an accuracy of ±0.4%. Water flow rate was monitored with a Kings 7520 7C-02 flow meter with typical flow rates of 0.33 ± 0.02 USGPM (1.25 ± 0.076 l/min). Temperature differences between the inlet and outlet was approximately 30 °C to 40 °C. Water temperatures of 80 °C or higher were undesired as boiling could occur within the copper cathode. Boiling would

change the thermal and viscous boundary layer within the copper pipe changing the convection coefficient. Temperature differences in the water reached steady state after approximately 20 seconds. Welding was maintained for approximately 30 seconds to ensure steady state was reached as shown in Figure A.4.

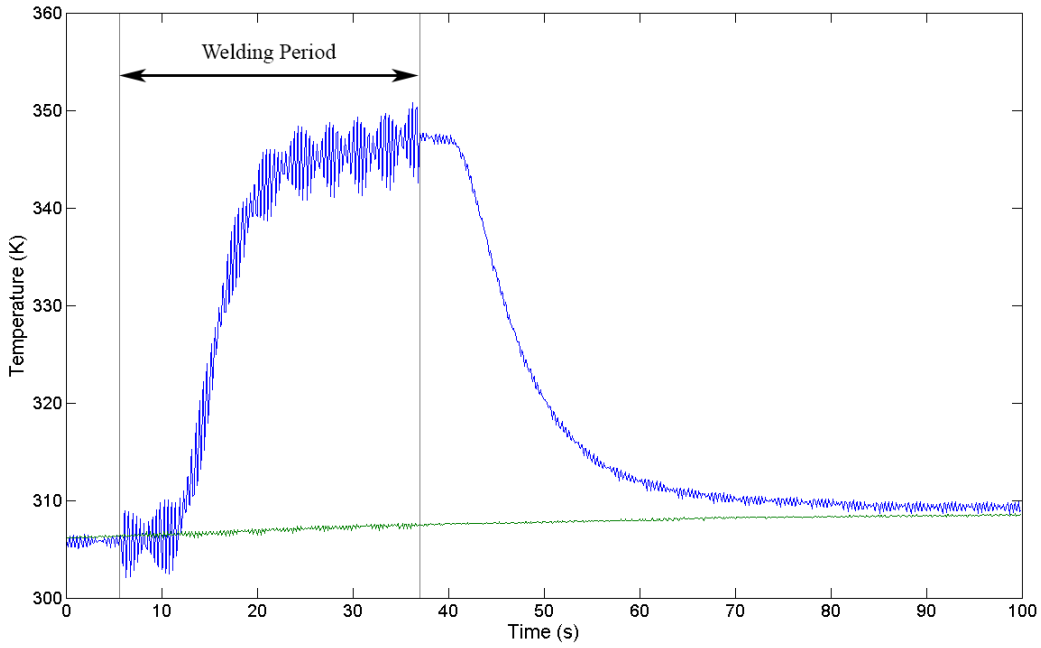

Fig. A.4: Water temperatures in the inlet and outlet of the copper cathode.

In order to initiate an arc between the copper cathode and electrode, a sacrificial metallic substance was used. Steel wool or aluminium foil were used to start the arcing process with steel or aluminium electrodes respectively. These sacrificial substances would often be vaporized or be blown away from the cathode upon arc initiation. These sacrifical metallic substances could contaminant the cathode changing the work function of the cathode slightly but is not likely to be substantial.

A.3. Contact Tip and Contact Tip Voltage Loss

The contact resistance between the contact tip and electrode will have an associated voltage loss. This voltage loss was measured with a tungsten bar as shown in Figures A.5-A.6. This approach is similar to that used by other researchers [83, 85]. There will also be a contact resistance between the tungsten bar and electrode as shown in Figure A.7 and A.8.

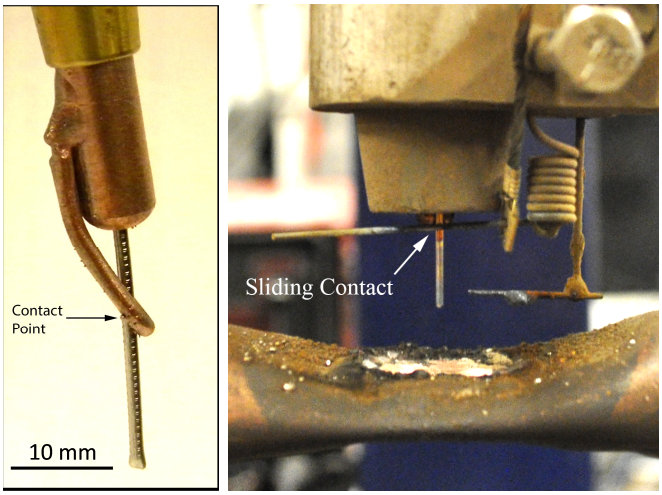

Fig. A.5: Left: Custom contact tip used in steel electrodes [2]. Right: Tungsten bar measuring contact tip voltage loss in steel electrodes.

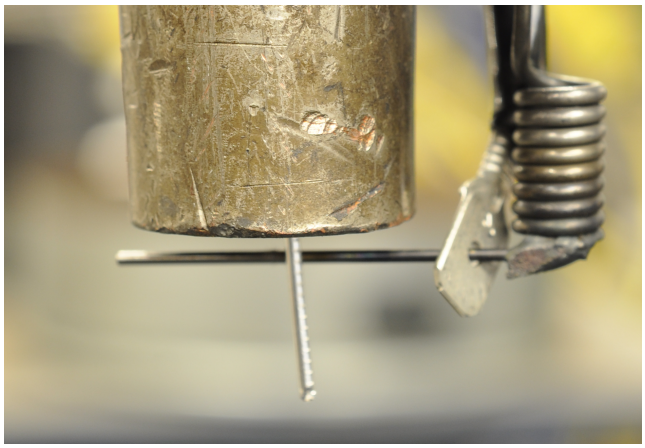

Fig. A.6: Tungsten probe used to measure contact tip voltage loss in aluminum electrode.

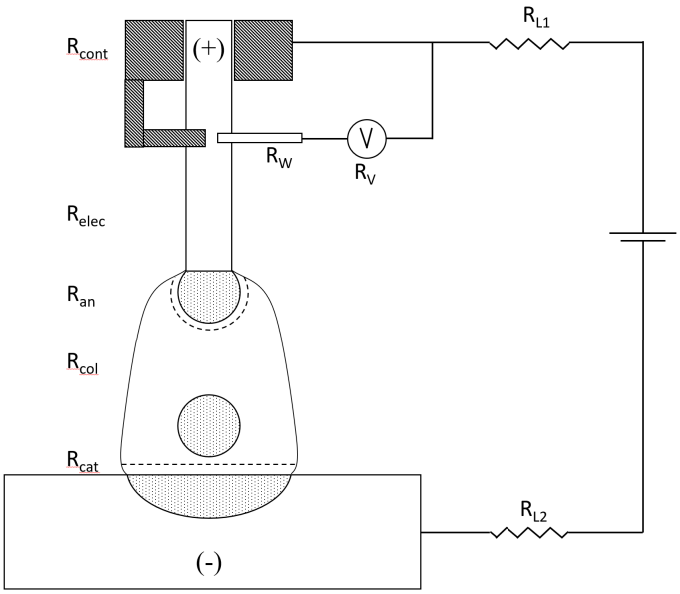

Fig. A.7: Typical GMAW system with important areas of resistance labelled. A tungsten probe was used to measure voltage loss associated with the contact tip. This diagram is only valid for constant voltage. Reactance was not considered in this diagram but will contribute to some voltage loss.

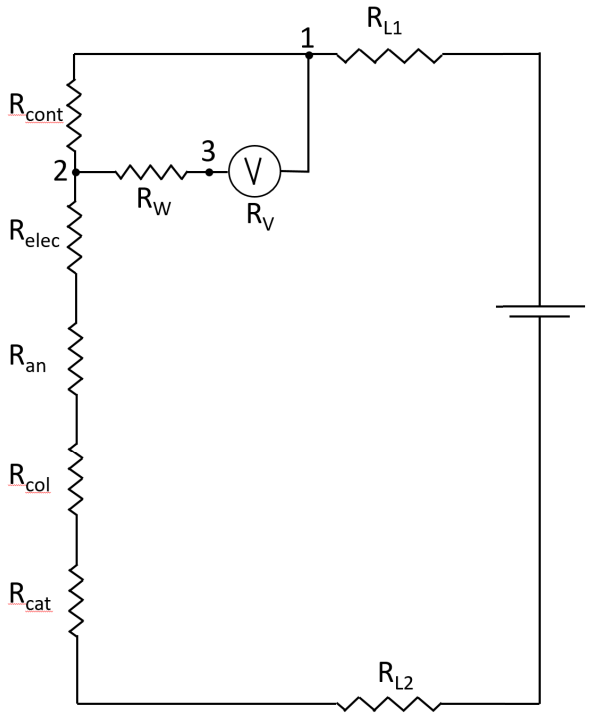

Fig. A.8: Figure A.7 viewed as an electrical diagram.

Steel experimentation utilized a customized contact tip as shown in Figure 2.2 and 3.3 [2]. This customized contact tip allowed the tungsten probe to measure contact tip voltage loss as close as possible to the point of contact. Aluminium experimentation utilized a normal industrial

contact tip as ohmic heating is often considered negligible in aluminium GMAW. As shown in Figure A.8, Ohm's law was used to determine the voltage loss associated between points 1 and 2:

$$V_{12} = R_{cont} I \tag{A.1}$$

$$V_{13} = R_V I_V \tag{A.2}$$

$$V_{13} = V_{12} + V_{23} = R_{cont} I + R_W I_V \tag{A.3}$$

Where V_{12} is the voltage loss between points 1 and 2, V_{13} is the voltage loss between points 1 and 3, V_{23} is the voltage loss between points 2 and 3, R_{cont} is the contact resistance of the contact tip, R_W is the contact resistance of the tungsten probe, R_V is the resistance of the voltmeter, I is the current of the welding system, and I_V is the current through the voltmeter. The voltmeter used in experimentation had a resistance of approximately $R_V = 3$ kΩ based on its design. Experimental values of V_{13} was 0.5 V giving a value of $I_V = 0.17$ mA. Since $I_V \ll I$, the resistance associated with the tungsten probe can be negelected:

$$V_{13} \approx V_{12} \tag{A.4}$$

A.4. Electrode Extension Voltage Loss

Steel experimentation utilized a customized contact tip as shown in Figure 2.2 and 3.3 [2]. The effects of Ohmic heating in steel electrodes has been shown to be substantial in GMAW. A known electrode extension allows for proper calculation of resistive heating into the wire electrode. Normal industrial contact tips can have a small variance in the measured electrode extension distance as it is unclear where the last point of contact is [2, 84]. Aluminium experimentation utilized a normal industrial contact tip as ohmic heating is often considered negligible in aluminium GMAW.

A tungsten indicator was set to the desired electrode extension distance as shown in Figure

3.3 and was used as a reference point for arc length measurements. All steel experiments attempted to have an electrode extension of ∼12.5 mm (0.5 in.) and arc length of ∼12.5 mm (0.5 in.). Arc lengths in steel experiments were visually verified in high speed videography. All aluminium experiments had varying electrode extensions and arc lengths and were each individually measured in high speed videography.

A known electrode extension allows for easier repetition and is used to calculate the resistance and voltage loss with a scaling analysis produced by Lehnhoff and Mendez [7]. The voltage drop in the electrode extension can be determined using an energy balance:

$$V_{elec} I = H_{c_2} U A_e \tag{A.5}$$

Where V_{elec} is the electrode voltage loss, H_{c_2} is the amount of joule heating gained by the electrode, U is the WFS, and A_e is the cross sectional area of the electrode. Following Lehnhoff, H_{c_2} can be calculated as [7]:

$$H_{c_2} = H_c \widehat{H_{c_2}^{+*}} \tag{A.6}$$

Where H_c is the enthalpy variation between room temperature and just before melting of the electrode. $\widehat{H_{c_2}^{+*}}$ can be determined as:

$$\widehat{H_{c_2}^{+*}} = 2\left[\frac{e^{\frac{d}{M_1}} - 1}{b\left(1 - e^{\frac{d}{M_1}}\right) + d\left(1 + e^{\frac{d}{M_1}}\right)}\right] \tag{A.7}$$

$$M_1 = \frac{U H_c A^2}{L \rho_0 I^2}, \quad d = \sqrt{b^2 - 4a}, \quad b = \frac{\Delta\rho_1}{\rho_0} + 4\frac{\Delta\rho_2}{\rho_0}, \quad a = -4\frac{\Delta\rho_2}{\rho_0} \tag{A.8}$$

Where ρ is the electrical resistivity, $\Delta\rho_0$ is the maximum change in ρ from H_0 to H_m, $\Delta\rho_1$ is the change in ρ, $\Delta\rho_2$ is the relative curvature in $\rho(H)$, H is the enthalpy in the wire material, and L is the electrode stickout [7]. Properties of ER70S-6 and pure aluminum were used for calculation of resistivity as shown in Table A.1 [7, 8].

Table A.1: Material parameters for AISI 1016 and experimental values used to determine electrode extension voltage loss [7, 8].

Material	ρ_0x10^7 (Ωm)	ρx10^7 (Ωm)	$\Delta\rho_1$x10^7 (Ωm)	$\Delta\rho_2$x10^7 (Ωm)	T_m (K)	H_cx10^{-9} (Jm^{-3})	A_ex10^6 (m^2)	Lx10^3 (m)
ER70S-6	3.30	11.7	11.7	3.30	1740	7.33	1.03	12.5
Aluminum	0.28	0.77	0.77	0	933	1.70	1.14	-

Appendix B: Equations and Uncertainty Analysis

B.1. List of Symbols

Table B.1: Symbols used throughout thesis.

Symbol	Definition	Units
A_e	Cross sectional area of electrode	m^2
D	Number of droplets counted in high speed video	-
d_d	Droplet diameter	m
d_w	Electrode/Wire diameter	m
e	Electron charge	C
f_c	Number of frames counted in high speed videography	-
f_d	Frequency of detachment	Hz
f_r	High speed video frame rate	Hz
H_{an}	Total anode/calorimeter heat	J
H_c	Electrode enthalpy variation between room temperature and melting point	J/m^3
H_{c_2}	Amount of joule heating gained by the electrode	J/m^3
H_d	Droplet enthalpy variation between average droplet temperature and melting point	J/m^3
H_f	Latent heat of fusion	J/m^3
H_m	Electrode enthalpy at melting temperature	J/m^3
H_0	Electrode enthalpy at room temperature	J/m^3
h	Convection coefficient between anode and arc	W/m^2K
H_w	Enthalpy of water	J/kg
I	Average current	A
J_a	Anode current density	A/m^2
k	Thermal conductivity	W/mK
k_{eff}	Effective thermal conductivity within anode	W/mK
L	Electrode stickout	m
L_A	Arc Length	m
L_{an}	Length of anode surface interaction	m
m	Portion of the anode heat lost by radiation	-
$\dot{m}$	Water flow rate in cathode	m^3/s
m_d	Mass of the droplet	g
P	Average instantaneous power	W
P_r	Prandtl number	-
q_{an}	Total anode heat input	W
q_{cat}	Total cathode heat input	W
q_{cond}	Heat conducted from arc to anode	W
q_{evap}	Heat lost from evaporation at anode	W
q_{rad}	Heat radiated from arc to anode	W
q'''_{rad}	Radiative heat flux of argon arc	W/m^3sr
q_{sur}	Heat radiated from anode to surroundings	W
r_d	Radius of a droplet	m
r_p	Radius of an arc sphere	m
T	Temperature of electrons	K
T_{an}	Anode (droplet) surface temperature	K
T_d	Average droplet temperature	K
T_f	Final temperature of the calorimeter and droplet	K
T_i	Initial temperature of the calorimeter	K
T_{in}	Inlet temperature of water in cathode	K
T_{out}	Outlet temperature of water in cathode	K
T_p	Arc temperature	K
T_∞	Surrounding temperature	K
U	Wire feed speed	$inch/min$ or m/s

Table B.1: Symbols used throughout thesis.

Symbol	Definition	Units
V	Average voltage	V
V_A	Anode sheath voltage	V
V_{an}	Overall anode fall voltage	V
V_C	Cathode sheath voltage	V
V_{cat}	Overall cathode fall voltage	V
V_{cont}	Contact tip voltage loss	V
V_{col}	Arc column voltage loss	V
V_{elec}	Electrode extension voltage loss from ohmic heating	V
V_{pot}	Arc column potential	V/mm
V_{tot}	Total average voltage not including welding cables	V
v_p	Velocity of arc/plasma	m/s
α	Thermal diffusivity	m^2/s
δ_t	Thickness of anode to arc boundary layer	m
ϵ_{Fe}	Emissivity coefficient of liquid iron	-
ϵ_o	Dielectric constant	-
η	Thermal Efficiency	%
ν	kinematic viscosity	m^2/s
ρ	Electrode resistivity	Ωm
ρ_e	Electrode density	kg/m^3
ρ_p	Plasma density	kg/m^3
$\Delta\rho_0$	Maximum resistivity change between H_0 and H_m	Ωm
$\Delta\rho_1$	Change between H_0 and H_m	Ωm
$\Delta\rho_2$	Relative curavture in $\rho(H)$	Ωm
ρ_w	Density of water	kg/m^3
σ	Stefan-Boltzmann constant	W/m^2K^4
ϕ_{an}	Anode work function	V
ϕ_{cat}	Cathode work function	V

B.2. Uncertainty of Equipment

Table B.2: Uncertainty of experimental equipment. Uncertainty of calorimeter was based on previous calibration tests [2].

Measuring Device	Symbol	Uncertainty (±)
Counted high speed video frames	δ_{f_c}	5
Total anode/calorimeter heat	$\delta_{H_{an}}$	1.1 %
Current transducer	δ_I	1.0 %
Water flow rate	$\delta_{\dot{m}}$	0.02 USGPM
Mass of droplets	δ_{m_d}	0.02 g
Thermocouples	δ_T	0.4 %
Wire feed speed	δ_U	1 inch/min (0.0254 m/min)
Voltage transducer	δ_V	0.9 %

B.3. Equations and Uncertainty

Outlined in this chapter are all major equations used in this thesis and will have some repeated equations as shown in Sections 2. Uncertainty calculations are also presented. Absolute uncertainties were used throughout all calculations.

B.3.1. Power

These equations were used to determine the average instantaneous power. Average instantaneous power was calculated between the contact tip and cathode.

$$P = \frac{1}{N}\sum_{i=1}^{N}(I_i V_i) \tag{B.1}$$

$$\delta_P = \frac{1}{N}\sum_{i=1}^{N}\left(\sqrt{(\delta_{I_i} V_i)^2 + (\delta_{V_i} I_i)^2}\right) \tag{B.2}$$

Where P is average instantaneous power, δ_P is the uncertainty in average instantaneous power, N is the number of data points of interest, I_i is instantaneous current, δ_{I_i} is the uncertainty in instantaneous current (1.0% of I_i), V_i is instantaneous voltage, and δ_{V_i} is the uncertainty in instantaneous voltage (0.9% of V_i).

B.3.2. Anode Heat Input

This equation was utilized to determine the heat input to the anode.

$$q_{an} = \frac{A_e \rho_e U H_{an}}{m_d} \tag{B.3}$$

$$\delta_{q_{an}} = A_e \rho_e \sqrt{\left(\frac{\delta_U H_{an}}{m_d}\right)^2 + \left(\frac{\delta_{H_{an}} U}{m_d}\right)^2 + \left(\frac{-\delta_{m_d} H_{an} U}{m_d^2}\right)^2} \tag{B.4}$$

Where q_{an} is the anode heat input, $\delta_{q_{an}}$ is the uncertainty in anode heat input, A_e is the cross sectional area of the electrode, ρ_e is the density of the electrode, U is the wire feed speed, δ_U is the uncertainty in wire feed speed (1 inch/min (0.0254 m/min)), H_{an} is the total anode/calorimeter heat, $\delta_{H_{an}}$ is the uncertainty in total calorimeter heat (1.1 % of H_{an}), m_d is the mass of the droplet, and δ_{m_d} is the uncertainty in droplet mass (0.02 g). For details on how H_{an} was calculated, see section E.1.

B.3.3. Cathode Heat Input

These equation was utilized to determine the heat input to the cathode from the welding arc.

$$q_{cat} = \dot{m}\Delta H_w \rho \tag{B.5}$$

$$\delta q_{cat} = \sqrt{(\Delta H_w \rho_w \delta_{\dot{m}})^2 + (\dot{m}\rho_w \delta_{\Delta H})^2} \tag{B.6}$$

Where q_{cat} is the cathode heat input, $\delta_{q_{cat}}$ is the cathode heat input uncertainty, $\dot{m}$ is the water flow rate, $\delta_{\dot{m}}$ is the water flow rate uncertainty (0.02 USGPM), ΔH_w is the enthalpy change in the water, $\delta_{\Delta H}$ is the water enthalpy change uncertainty (based on 0.4 % thermocouple uncertainty), and ρ_w is the density of the water. For details on how ΔH_w was calculated, see section E.2.

B.3.4. Efficiency

These equations were used to determine the thermal efficiency of the welding system

$$\eta = \frac{100(q_{an} + q_{cat})}{P} \tag{B.7}$$

$$\delta_\eta = \sqrt{\left(\frac{100\delta_{q_{an}}}{P}\right)^2 + \left(\frac{100\delta_{q_{cat}}}{P}\right)^2 + \left(\frac{-100\delta_P(q_{an} + q_{cat})}{P^2}\right)^2} \tag{B.8}$$

Where η is the thermal efficiency, δ_η is the uncertainty in thermal efficiency, q_{an} is the anode heat input, $\delta_{q_{an}}$ is the uncertainty anode heat input, q_{cat} is the cathode heat input, $\delta_{q_{cat}}$ is the uncertainty in cathode heat input, P is average instantaneous power, and δ_P is the uncertainty in average instantaneous power.

B.3.5. Frequency of Detachment

These equations were used to determine the droplet detachment frequency utilizing the high speed videos and manual counting.

$$f_d = \frac{Df_r}{f_c} \tag{B.9}$$

$$\delta_D = 100/D \tag{B.10}$$

$$\delta_{f_d} = \sqrt{\left(\frac{\delta_D f_r}{f_c}\right)^2 + \left(\frac{-\delta_{f_c} D f_r}{f_c^2}\right)^2} \tag{B.11}$$

Where f_d is the frequency of detachment, δ_{f_d} is the uncertainty of frequency of detachment, D is the number of droplets counted, δ_D is the uncertainty in droplets counted, f_r is the high speed videography frame rate, f_c is the number of frames counted during droplet detachment, and δ_{f_c} is the uncertainty of the number of frames counted (estimated value of 5).

B.3.6. Droplet Diameter

These equations were used to determine the droplet diameter utilizing the high speed videos.

$$d_d = \left(\frac{3U(d_w)^2}{2f_d}\right)^{\frac{1}{3}} \tag{B.12}$$

$$\delta_{d_d} = \sqrt{\left(\frac{\delta_U}{U^{2/3}}\left(\frac{3{d_w}^2}{2f_d}\right)^{1/3}\right)^2 + \left(\frac{-\delta_{f_d}}{{f_d}^{4/3}}\left(\frac{3{d_w}^2}{2}\right)^{1/3}\right)^2} \tag{B.13}$$

Where d_d is the droplet diameter, δ_{d_d} is the uncertainty of the droplet diameter, d_w is the electrode diameter, U is the wire feed speed, δ_U is the uncertainty of wire feed speed (1 inch/min (0.0254 m/min)), f_d is the frequency of detachment, and δ_{f_d} is the uncertainty in frequency of detachment.

B.3.7. Overall Anode Fall Voltage

Overall anode fall voltage was calculated based on anode heat input and average current.

$$V_{an} = \frac{q_{an}}{I} - V_{elec} - V_{cont} \tag{B.14}$$

$$\delta_{V_{an}} = \sqrt{(\delta_{q_{an}} I)^2 + \left(\frac{-\delta_I q_{an}}{I^2}\right)^2 + \delta_{elec} + \delta_{cont}} \tag{B.15}$$

Where V_{an} is the overall anode fall voltage, $\delta_{V_{an}}$ is the uncertainty in overall anode fall voltage, q_{an} is the anode heat input, $\delta_{q_{an}}$ is the anode heat input uncertainty, V_{elec} is the electrode extension voltage loss, $\delta_{V_{elec}}$ is the uncertainty in electrode extension voltage loss, V_{cont} is the contact tip voltage loss, $\delta_{V_{cont}}$ is the uncertainty in contact tip voltage loss, I is average current, and δ_I is the average current uncertainty (1.0% of I).

B.3.8. Overall Cathode Fall Voltage

Overall cathode fall voltage was calculated based on cathode heat input and average current.

$$V_{cat} = \frac{q_{cat}}{I} \tag{B.16}$$

$$\delta_{V_{cat}} = \sqrt{(\delta_{q_{cat}} I)^2 + \left(\frac{-\delta_I q_{cat}}{I^2}\right)^2} \tag{B.17}$$

Where V_{cat} is the overall cathode fall voltage, $\delta_{V_{cat}}$ is the uncertainty in overall cathode fall voltage, q_{cat} is the cathode heat input, $\delta_{q_{cat}}$ is the cathode heat input uncertainty, I is average current, and δ_I is the average current uncertainty (1.0% of I).

B.3.9. Arc Column Voltage Loss and Potential

Arc column voltage loss was calculated from the differences in the other voltage regions.

$$V_{col} = V - V_{cat} - V_{an} - V_{elec} - V_{cont} \tag{B.18}$$

$$\delta_{V_{col}} = \delta_V - \delta_{V_{cat}} - \delta_{V_{an}} - \delta_{V_{cont}} \tag{B.19}$$

$$V_{pot} = \frac{V_{col}}{L_A} \tag{B.20}$$

$$\delta_{V_{pot}} = \frac{\delta_{V_{col}}}{L_A} \tag{B.21}$$

Where V_{col} is the arc column voltage loss, $\delta_{V_{col}}$ is the uncertainty in arc column voltage loss, V is average voltage, and δ_V is the average voltage uncertainty (0.9% of V), V_{cat} is the overall cathode fall voltage, $\delta_{V_{cat}}$ is the uncertainty in the overall cathode fall voltage, V_{an} is the overall anode fall voltage, $\delta_{V_{an}}$ is the uncertainty in overall anode fall voltage, V_{elec} is the electrode extension voltage loss, V_{cont} is the contact tip voltage loss, $\delta_{V_{cont}}$ is the uncertainty in the contact tip voltage loss (0.9% of V_{cont}), V_{pot} is the arc column potential, $\delta_{V_{pot}}$ is the uncertainty in the arc column potential, and L_A is the arc length. It was assumed that the uncertainty in V_{elec} was zero.

B.3.10. Deposition Rate

This equation was used to determine the deposition rate or the overall anode fall voltage. No uncertainty calculation was performed alongside this calculation.

$$q_{an} = (V_{an} + V_{elec} + V_{cont})I = A_e U(H_d + H_f + H_c) \tag{B.22}$$

Where q_{an} is the total anode heat input, V_{an} is the overall anode fall voltage, V_{elec} is the electrode extension voltage loss, V_{cont} is the contact tip voltage loss, I is the current, A_e is the cross sectional area of the electrode, U is the wire feed speed, H_d is the droplet enthalpy variation between average droplet temperature and melting temperature, H_f is the latent heat of fusion, and H_c is the enthalpy variation between melting temperature and room temperature.

Appendix C: Conduction, Radiation, and Evaporation

C.1. Anode Heating and Cooling Within Arc

It was assumed throughout experimentation that convection, conduction, and radiation from the welding arc to the droplet was negligible. Heat gained by the anode by conduction, convection, and radiation from the plasma is calculated. Heat lost by the anode due to evaporation and radiation is calculated. These values were calculated based on some of the thermal properties of pure Ar shielding gas and pure Fe [7–12, 50]. Calculations with the 4043 electrode were not performed as a substantially lower amount of literature is available for comparisons.

C.1.1. Arc Conduction to Anode

The temperature differences between the arc and anode indicate that heat would transfer from the arc to the anode. Temperature measurements indicate that a GMAW arc is approximately 5,000 K to 15,000 K [16, 25–27] and the temperature of a carbon steel anode surface is approximately 3000 K during droplet growth [41]. The relatively low anode surface temperature causes a thermal boundary layer to form between the anode and arc. The boundary layer was assumed to be sufficient small as shown in Figure C.1. Boundary conditions were chosen to be 3,000 K at the anode surface and 6,000 K at the plasma. 6,000 K was chosen based on the temperature at which a Ar plasma starts to show significant electrical conductivity.

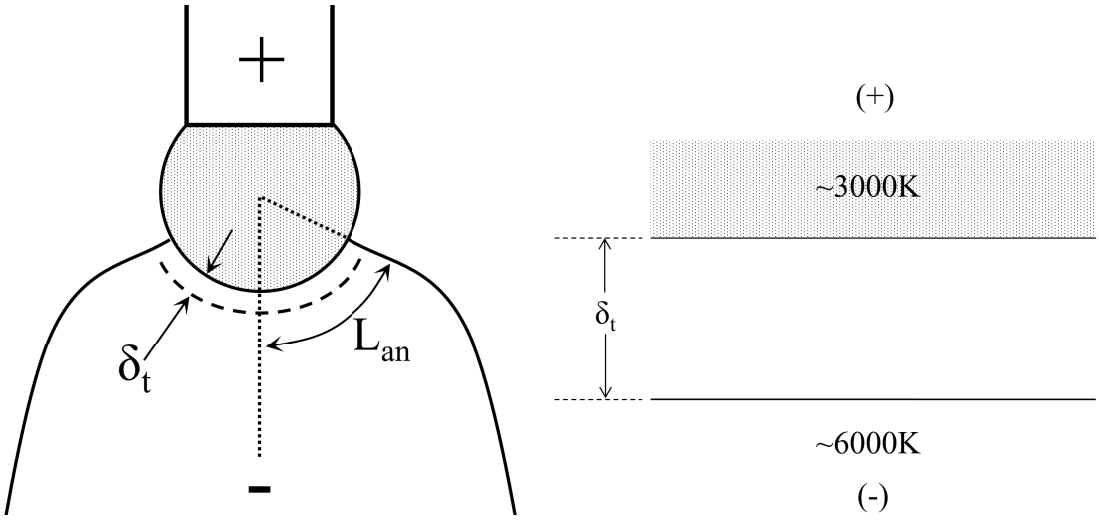

Fig. C.1: 1-D heat transfer at the anode surface. It was assumed that energy was not lost or generated.

Welding constants used in these calculations are shown in Table C.1. An average temperature of 4,500 K was used for the thermal boundary layer properties as shown in Table C.2 [9–12].

Table C.1: Welding values used for the 1-D heat transfer problem assuming a plasma temperature of 6,000 K.

Symbol	Value	Units	Description
μ_0	1.26x10^{-6}	$\frac{N}{A^2}$	Permeability of free space
I	200	A	Current
L_{an}	1.13	mm	Length of anode surface interaction
T_{an}	3,000	K	Temperature of anode surface
T_p	6000	K	Temperature of plasma near anode

Table C.2: Properties of pure Ar at 4,500 K [9–12].

Symbol	Value	Units	Description
k	0.120	$\frac{W}{mK}$	Thermal conductivity
ρ_p	0.108	$\frac{kg}{m^3}$	Density
C_p	520.4	$\frac{J}{kgK}$	Specific heat capacity
μ	1.53x10^{-4}	$\frac{kg}{ms}$	Dynamic viscosity
α	2.12x10^{-3}	$\frac{m^2}{s}$	Thermal diffusivity
P_r	0.667	-	Prandtl number

The Prandtl number lower than 1 indicates that thermal conduction dominates. 1-D conduction equations were applied as shown in Equations C.1-C.4 and Table C.3 [110].

$$q_{cond} = k\frac{T_p - T_{an}}{\delta_t}\pi L_{an}^2 \tag{C.1}$$

$$\delta_t = \sqrt{\pi\nu\frac{L_{an}}{v_p}}P_r^{-1/2} = \sqrt{\pi\alpha\frac{L_{an}}{v_p}} \tag{C.2}$$

$$v_p = \frac{1}{2}\frac{\mu_0^{1/2}L_{an}J_a}{\rho_p^{1/2}} = \frac{1}{2\pi}\frac{\mu_0^{1/2}I}{\rho_p^{1/2}L_{an}} \tag{C.3}$$

$$q_{cond} = \frac{1}{\sqrt{2}}\frac{kL_{an}\mu_0^{1/4}I^{1/2}}{\alpha^{1/2}\rho_p^{1/4}}(T_p - T_{an}) \tag{C.4}$$

Table C.3: Amount of heat conducted from arc to anode.

Symbol	Value	Units	Description
v_p	96.14	$\frac{m}{s}$	Velocity of plasma near the anode
δ_t	0.280	mm	Boundary layer thickness
q_{cond}	5.13	W	Amount of heat transfered at anode surface
q''_{cond}	1.28x10^6	$\frac{W}{m^2}$	Conduction heat flux
h	427.17	$\frac{W}{m^2K}$	Convection value

An arc temperature of 6,000 K may be too low near the anode surface [68]. Equations B.1-B.4 were used for an average plasma temperature of 17,000 K as shown in Table C.4. This temperature is considered high for a GMAW arc but was calculated to determine the extent of conduction heating [16, 25–27].

Table C.4: Amount of heat conducted from arc to anode assuming a plasma temperature of 17,000 K. An average boundary layer temperature of 10,000 K was used for the properties of pure Ar [9–12].

Symbol	Value	Units	Description
μ_0	1.26x10^{-6}	$\frac{N}{A^2}$	Permeability of free space
I	200	A	Current
L_{an}	1.13	mm	Length of anode surface interaction
T_{an}	3,000	K	Temperature of anode surface
T_p	17000	K	Temperature of plasma near anode
k	0.665	$\frac{W}{mK}$	Thermal conductivity
ρ_p	0.048	$\frac{kg}{m^3}$	Density
C_p	1480.0	$\frac{J}{kgK}$	Specific heat capacity
μ	2.64x10^{-4}	$\frac{kg}{ms}$	Dynamic viscosity
α	9.43x10^{-3}	$\frac{m^2}{s}$	Thermal diffusivity
P_r	0.586	-	Prandtl number
v_p	144.80	$\frac{m}{s}$	Velocity of plasma
δ_t	0.480	mm	Boundary layer thickness
q_{cond}	77.57	W	Amount of heat transfered at anode surface
q''_{cond}	1.94x10^7	$\frac{W}{m^2}$	Conduction heat flux
h	1385.15	$\frac{W}{m^2K}$	Convection value

C.1.2. Arc Radiation to Anode

Radiation energy from the arc will be distributed to the anode. The amount of energy absorbed by the anode will be dependent on the size of the arc, size of the droplet, emissivity of the arc, emissivity of the anode material, temperature of the anode, and temperature of the arc. To determine the amount of radiation absorbed by the anode, the droplet was simplified to be surrounded by a sphere of plasma as shown in Figure C.2.

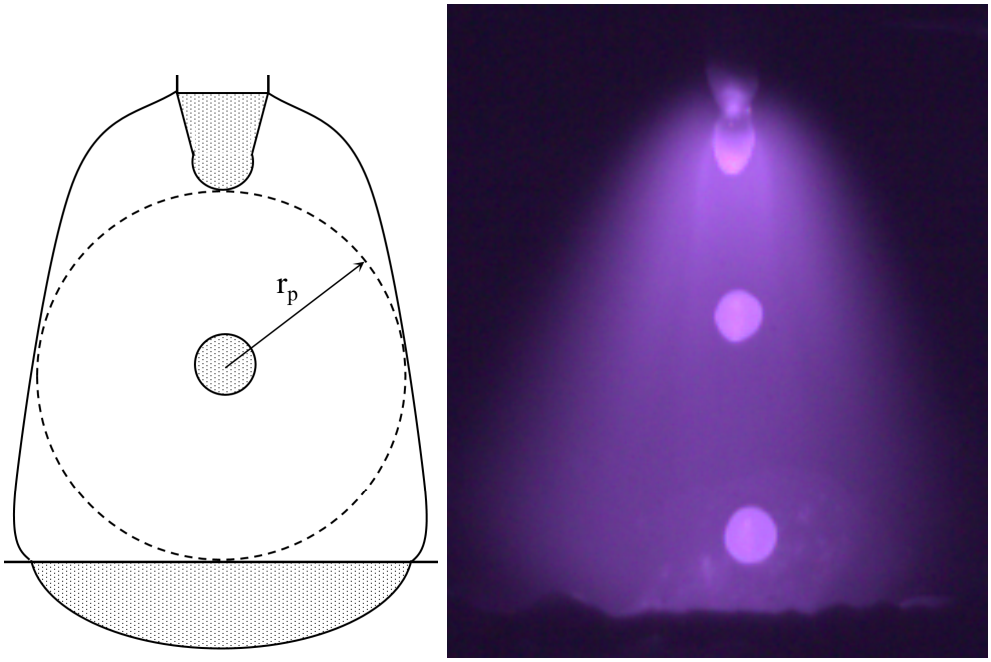

Fig. C.2: Droplet was simplified to be surrounded by a sphere of plasma.

It was assumed that half of all arc radiated energy would be directed towards the droplet, and half would be radiated away. It was also assumed that the temperature of the plasma would be at a constant 10,000K throughout the arc column despite the differences in inner and outer arc column temperatures [16, 25–27]. The size of the droplet and plasma were approximated from Figure C.2. The amount of energy absorbed by the droplet was then calculated with equation C.5 with results summarized in Table C.5.

$$q_{rad} = \epsilon_{Fe} \frac{2\pi}{3} (r_p^3 - r_d^3) q'''_{rad} \tag{C.5}$$

Table C.5: Amount of radiative energy absorbed by the iron anode from the welding arc [9–13].

Symbol	Value	Units	Description
d_d	1.02	mm	Droplet diameter
r_d	0.51	mm	Droplet radius
r_p	4.90	mm	Plasma radius
T_{an}	3000	K	Temperature of anode surface
T_p	10000	K	Temperature of plasma
q'''_{rad}	1.04x10^{-7}	$\frac{W}{m^3 sr}$	Radiative energy of argon plasma at 10,000 K
ϵ_{Fe}	0.29	-	Emissivity of liquid iron
q_{rad}	9.31	W	Radiative energy to anode from arc

C.1.3. Anode Radiation to Surroundings

The anode will emit radiative energy to the surrounding atmosphere during droplet growth and after detachment. This energy loss was determined with the Stefan-Boltzmann equation with results summarized in Table C.6. It was assumed that the entire droplet surface was at a temperature of 3000 K and is an over-approximation [41].

$$q_{sur} = \epsilon_{Fe}\sigma(T_d^4 - T_\infty^4) \tag{C.6}$$

Table C.6: Energy lost to surroundings from anode [9–13]. Droplet diameter determined from Figure C.2.

Symbol	Value	Units	Description
μ_0	1.26x10^{-6}	$\frac{N}{A^2}$	Permeability of Free Space
σ	5.67x10^{-8}	$\frac{W}{m^2 K^4}$	Stefan Boltzmann Constant
I	200	A	Current
ϵ_{Fe}	0.29	-	Emissivity of liquid iron
d_d	1.02	mm	Droplet diameter
T_{an}	3000	K	Temperature of anode surface
q_{sur}	6.14	W	Energy radiated away from anode to surroundings

C.1.4. Anode Evaporation

Evaporative supercooling will occur at the droplet surface lowering the overall energy of the droplet. It was assumed that the droplet surface temperature is 3,000 K and all metal vapours

produced are metallic. Soderstrom has found that fumes emitted from an ER70S-6 electrode is approximately 83 wt% Fe and 17 wt% Mn. Utilizing the enthalpy of vapourization and typical fume formation rates, energy lost by evaporation was calculated and is summarized in Table C.7

Table C.7: Typical energy loss by anode evaporation [14, 15]. It was assumed that vapours from an ER70S-6 electrode was 83 wt% Fe and 17 wt% Mn [3].

Symbol	Value	Units	Description
FFR	0.1	$\frac{g}{min}$	Low fume formation rate (project spray region)
FFR	0.9	$\frac{g}{min}$	High fume formation rate (spray region)
H_{Fe}	6189	$\frac{J}{g}$	Iron enthalpy of vapourization
H_{Mn}	4023	$\frac{J}{g}$	Manganese enthalpy of vapourization
H_v	5821	$\frac{J}{g}$	ER70S-6 enthalpy of vapourization
T_a	3000	K	Temperature of anode surface
q_{evap}	9.7	W	Low evaporation energy (project spray region)
q_{evap}	87.3	W	High evaporation energy (spray region)

C.2. Anode Energy Lost and Gained

As shown in Sections C.1.1-C.1.4, the amount of energy gained and lost at the anode by conduction, radiation, and evaporation was determined. These results are summarized in Table C.8 for an iron anode with typical measured anode heat inputs.

Table C.8: Influence of conduction, radiation, and evaporation on anode heat inputs in a ER70S-6 electrode.

Symbol	Value	Units	% of q_{an}	Description
q_{an}	1750	W	-	Typical anode heat inputs
q_{cond}	5.13	W	0.29	Conduction from arc to anode (T_p of 6,000 K)
q_{cond}	77.57	W	4.43	Conduction from arc to anode (T_p of 17,000 K)
q_{rad}	9.31	W	0.53	Radiation from arc to anode
q_{sur}	-6.14	W	-0.35	Radiation from anode to surroundings
q_{evap}	-9.70	W	-0.55	Evaporation at anode surface (projected spray)
q_{evap}	-87.31	W	-4.99	Evaporation at anode surface (projected spray)

As shown in Table C.8, conduction and radiation typically influence total anode heat inputs by <1%. If the arc is assumed to be a very high temperature of 17,000 K, then conduction begins to measurably influence anode heat inputs by up to 4.4 %. Evaporative supercooling can reduce total anode heat input by 5%. Both conductive and evaporative energy were not accounted

for when calculating q_{an} as shown in section 3.5.2. The full extent which conduction and evaporation influence overall anode fall voltage is unclear, but results indicate that conduction and evaporation are significant and should be accounted for in future overall anode fall voltage calculations.

C.3. Anode Thermal Conductivity Coefficient

Conduction inside the anode was determined based on the overall anode fall voltage. Conduction inside the droplet was assumed to follow a conical frustum path as shown in Figure C.3. Conduction inside the droplet was then calculated with equation C.7.

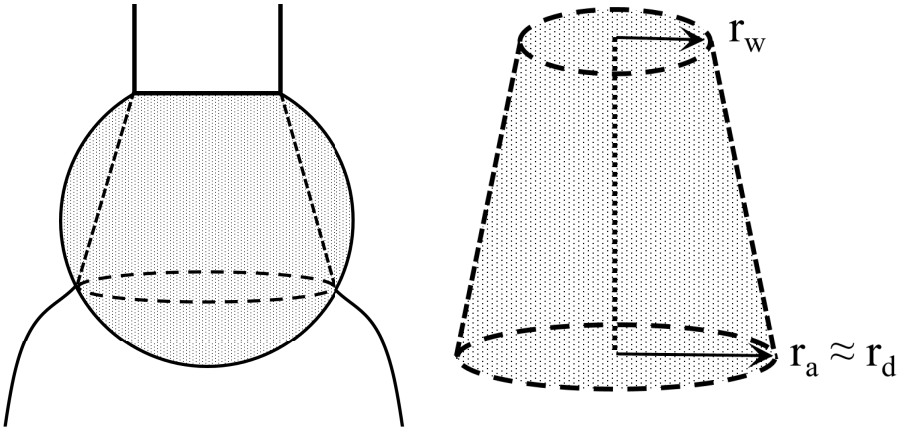

Fig. C.3: Conduction inside the droplet was assumed to follow a conical frustum path.

$$k_{eff} = \frac{1}{\sqrt{\pi}} \frac{V_{an} d_d}{d_w} \frac{\sqrt{I J_a}}{T_d - T_m} \tag{C.7}$$

Where k_{eff} is the effective thermal conductivity coefficient in the anode, V_{an} is the overall anode fall voltage, d_d is the droplet diameter, d_w is the diameter of the wire, I is the current, J_a is the current density at the anode, T_d is the average droplet temperature, and T_m is the melting temperature. It was assumed that the current density was constant at 5.0x10^7 A/m^2. Experimental results outlined in sections 3.4 and 4.4, were used with results summarized in Figure C.4.

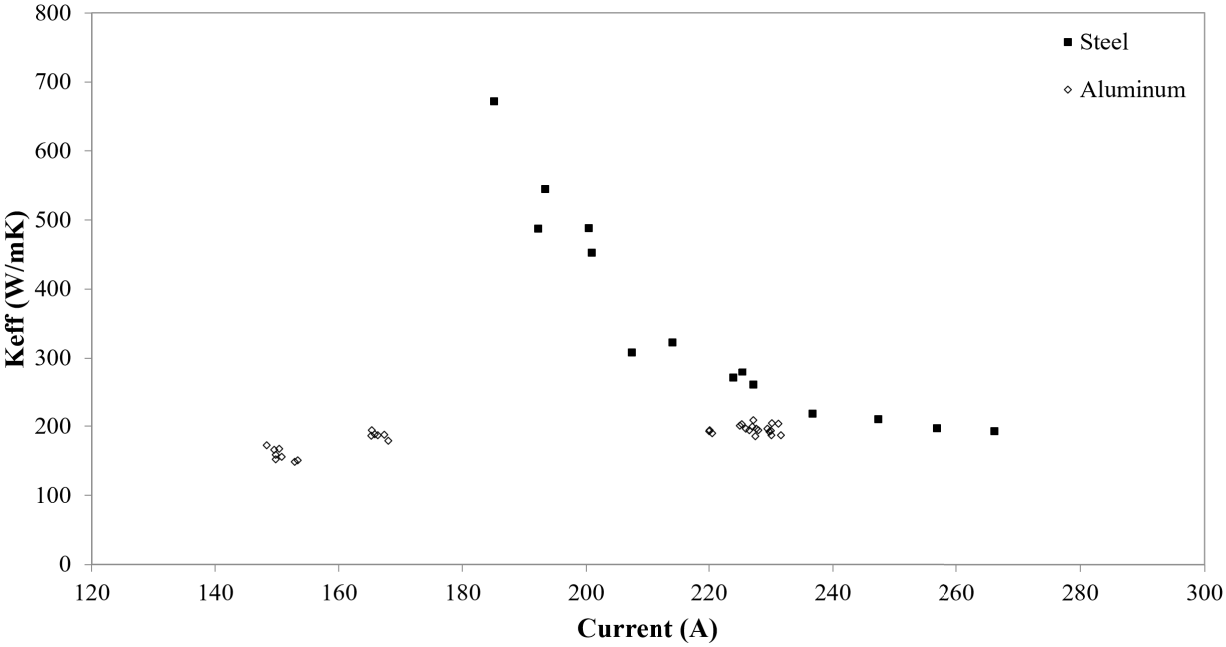

Fig. C.4: Thermal conductivity of droplets using an 0.045 in. (1.143 in.) ER70S-6 carbon steel and 3/64 in. (1.2 mm) 4043 aluminum electrode. Both steel and aluminum used 100% Ar shielding gas.

Thermal conductivity within a steel anode appears to be dependent on current. Thermal conductivity of steel in projected spray metal transfer approached approximately 200 W/mK. Aluminum appears to be constant with current and waveform selection at approximately 200 W/mK.

Appendix D: Deposition Rates

D.1. Deposition Rate Experiments

Many researchers have determined anode and cathode fall voltage by comparing the deposition rates in direct current electrode positive (DCEP) polarity and direct current electrode negative (DCEN) polarity. With knowledge of droplet temperature and thermal properties of the electrode, empirical findings of deposition rates can be used to calculate total electrode heat input. This heat input can be used to calculate a fall voltage. A series of deposition rate experiments were conducted with steel in DCEP to compare the anode fall voltage findings with those found in the calorimeter.

D.2. Deposition Rate Experimental Setup

Bead on plate tests were performed with an 0.045 in. (1.143 mm) ER70S-6 electrode on a carbon steel plate. All welds were done in constant voltage (CV) mode, in DCEP, in the 1-G (PA) position, and at a travel speed of 5 mm/s (11.8 inch/min). All welds had a contact tip to work piece distance of 25 mm. Electrode extension and arc length were both approximately 12.5 mm. 100% Ar, 95% Ar - 5% CO_2, 90% Ar - 10% CO_2, and 85% Ar - 15% CO_2 shielding gas blends were used for experimentation. Shielding gas was mixed to 35 standard cubic feet per hour (16.52 l/min) using an OMEGA FL-6GP-40ST-40ST-40ST gas proportioning rotameter. Welding was performed with a Lincoln Power Wave S500, a Lincoln 84 Dual Feeder (program 5 weld set reference: Z153615), and a Tregaskiss Tough Gun I.C.E. water-cooled robotic MIG torch.

The anode fall voltage was calculated from the total anode heat input and is the same as equation B.22.

$$q_{an} = (V_{an} + V_{elec} + V_{cont})I = A_e U(H_d + H_f + H_c) \tag{D.1}$$

Where q_{an} is the total anode heat input, V_{an} is the overall anode fall voltage, V_{elec} is the electrode extension voltage loss, V_{cont} is the contact tip voltage loss, I is the current, A_e is the cross sectional area of the electrode, U is the wire feed speed, H_d is the droplet enthalpy

variation between average droplet temperature and melting temperature, H_f is the enthalpy of fusion, and H_c is the enthalpy variation between melting temperature and room temperature. Experimental and material parameters used in this calculation are shown in Table D.1.

Table D.1: Experimental and material parameters for deposition rate tests [7, 8].

T_m (K)	T_d (K)	R_{cont} (Ω)	V_{an} (V)	$H_c x10^{-9}$ (J/m^3)	$H_f x10^{-9}$ (J/m^3)	$A_e x10^6$ (m^2)	$L x10^3$ (m)
1740	2773	2.16	4.7	7.33	1.73	1.03	12.5

Lehnhoff's model was used to determine V_{elec} with an electrode extension of 12.5 mm (0.5 in.) as shown in Appendix A.4. V_{cont} was calculated from the previously measured contact tip resistance of 2.16 $m\Omega$. These calculations assumed a constant droplet temperature of 2500 °C.

D.3. Deposition Rate Results

Deposition rate as a function of current were experimentally determined and are shown in Figures D.1-D.4. Higher currents could not be tested with 90% Ar - 10% CO_2 and 85% Ar - 15% CO_2 shielding gas blends as the maximum voltage output was reached attempting to maintain an arc length of 12.5 mm at these high currents. All values are shown in Tables D.2-D.5.

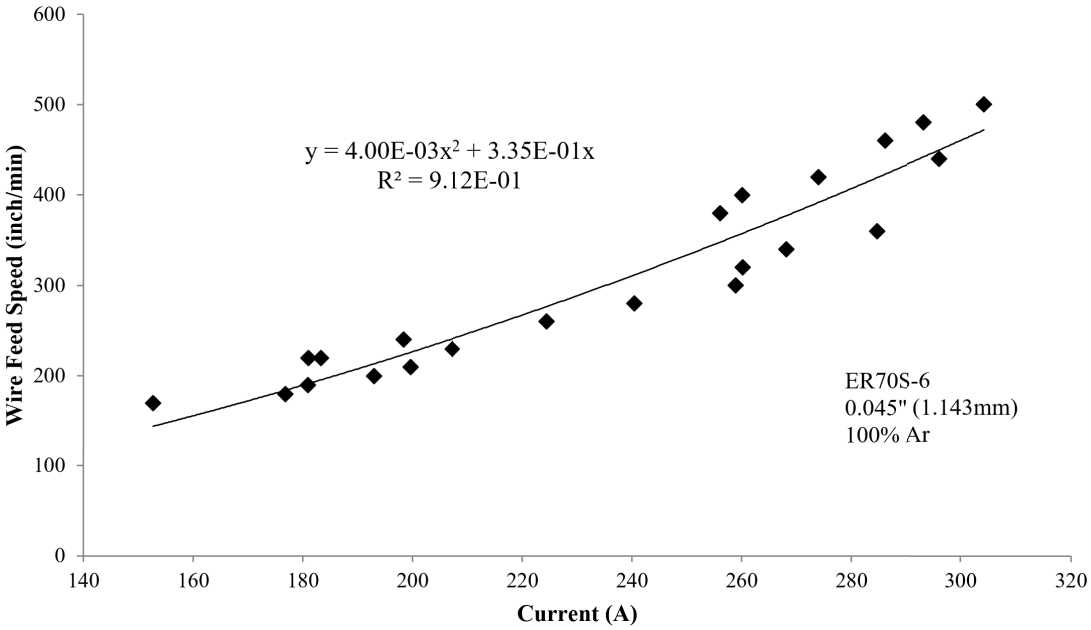

Fig. D.1: Bead on plate deposition rates as a function of current for a 0.045 in. (1.143 mm) ER70S-6 electrode with 100% Ar shielding gas. Electrode extension was 12.5 mm (0.5 in.). See Table D.2 for details.

Table D.2: Tabulated values shown in Figure D.1. Welding results for a 0.045 in. (1.143 mm) ER70S-6 electrode with 100% Ar shielding gas. Electrode extension was 12.5 mm (0.5 in.).

100% Ar				
Average Voltage (V)	Average Current (A)	Wire Feed Speed (inch/min)	Frequency of Detachment (Hz)	Droplet Diameter (mm)
30.2	152.7	170	68	1.275
26.1	176.8	180	72	1.272
26.2	180.9	190	60	1.382
26.4	193.0	200	30	1.760
26.8	199.6	210	39	1.642
28.8	183.3	220	74	1.352
27.0	181.0	220	72	1.362
27.1	207.3	230	75	1.367
29.6	198.3	240	118	1.190
28.8	224.5	260	306	0.890
30.0	240.5	280	476	0.787
32.7	259.0	300	478	0.804
33.6	260.2	320	491	0.815
34.1	268.1	340	500	0.826
34.6	284.7	360	530	0.826
34.4	256.1	380	513	0.850
34.8	260.1	400	533	0.854
35.7	274.0	420	559	0.854
35.7	296.1	440	570	0.862
35.8	286.1	460	567	0.876
35.8	293.2	480	664	0.843
35.7	304.2	500	780	0.810

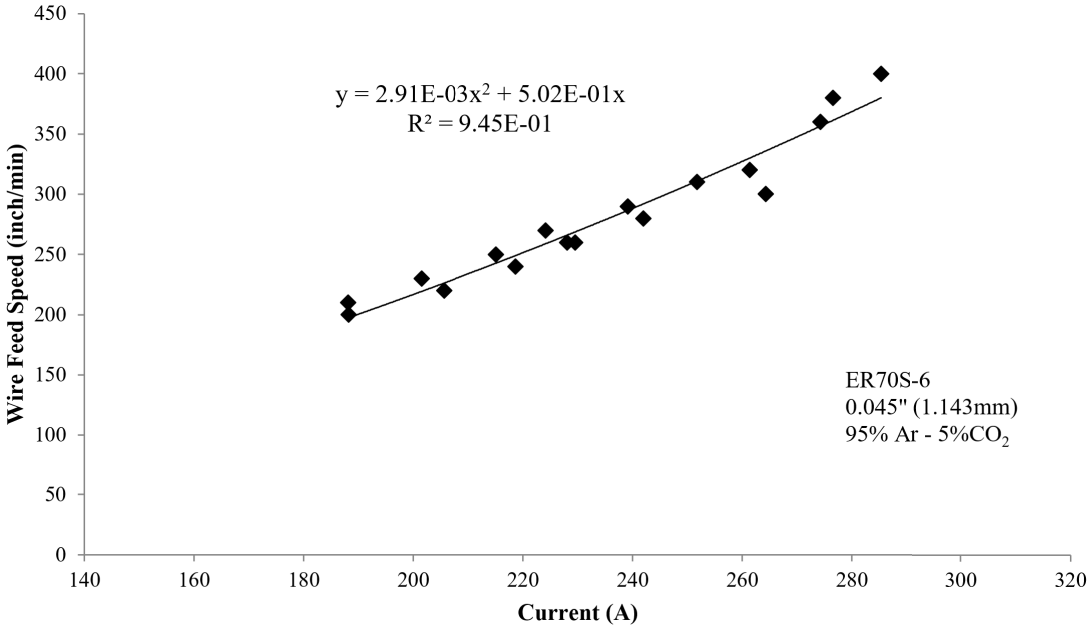

Fig. D.2: Bead on plate deposition rates as a function of current for a 0.045 in. (1.143 mm) ER70S-6 electrode with 95% Ar - 5% CO_2 shielding gas. Electrode extension was 12.5 mm (0.5 in.). See Table D.3 for details.

Table D.3: Tabulated values shown in Figure D.2. Welding results for a 0.045 in. (1.143 mm) ER70S-6 electrode with 95% Ar - 5% CO_2 shielding gas. Electrode extension was 12.5 mm (0.5 in.).

95% Ar - 5% CO2				
Average Voltage (V)	Average Current (A)	Wire Feed Speed (inch/min)	Frequency of Detachment (Hz)	Droplet Diameter (mm)
32.4	188.2	200	75	1.304
32.8	188.1	210	40	1.636
N/A	205.6	220	79	1.320
32.9	201.6	230	87	1.299
33.0	218.8	240	191	1.013
33.2	215.2	250	196	1.019
32.5	228.2	260	239	0.967
32.7	229.6	260	281	0.916
33.4	224.2	270	241	0.976
32.2	242.1	280	355	0.868
33.5	239.2	290	344	0.888
34.1	264.4	300	424	0.837
33.6	251.8	310	411	0.855
33.7	261.4	320	394	0.877
34.3	274.3	360	456	0.868
34.5	276.5	380	463	0.880
35.1	285.3	400	467	0.892

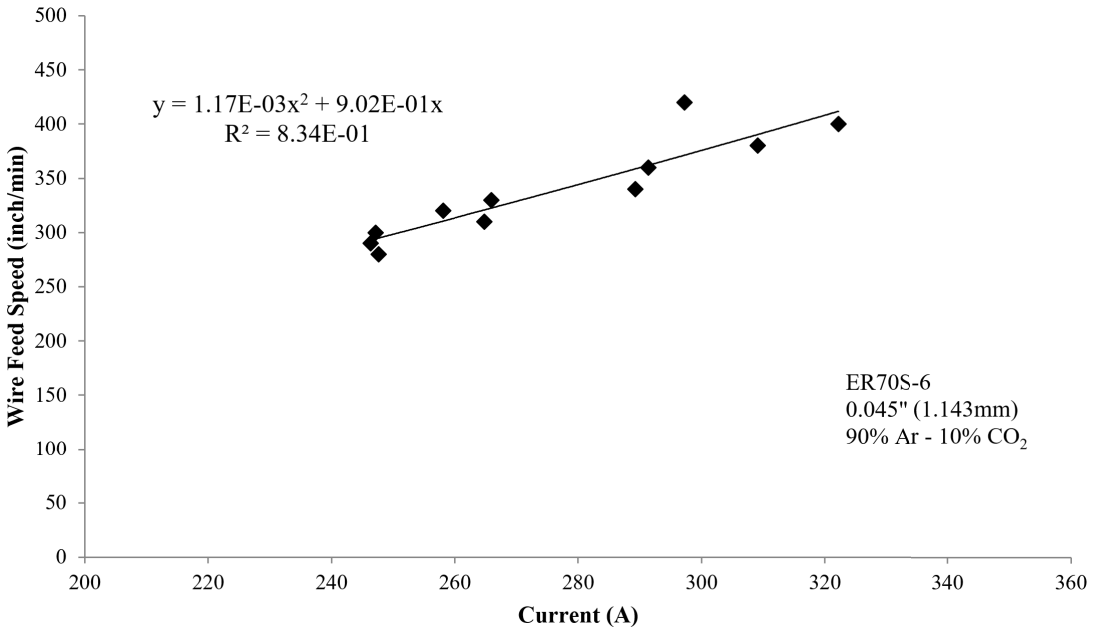

Fig. D.3: Bead on plate deposition rates as a function of current for a 0.045 in. (1.143 mm) ER70S-6 electrode with 90% Ar - 10% CO_2 shielding gas. Electrode extension was 12.5 mm (0.5 in.). See Table D.4 for details.

Table D.4: Tabulated values shown in Figure D.3. Welding results for a 0.045 in. (1.143 mm) ER70S-6 electrode with 90% Ar - 10% CO_2 shielding gas. Electrode extension was 12.5 mm (0.5 in.).

90% Ar - 10% CO2				
Average Voltage (V)	Average Current (A)	Wire Feed Speed (inch/min)	Frequency of Detachment (Hz)	Droplet Diameter (mm)
31.7	247.7	280	143	1.177
31.8	246.4	290	158	1.151
32.1	247.2	300	221	1.041
32.4	264.9	310	234	1.032
33.0	258.1	320	247	1.024
33.1	266.1	330	264	1.012
33.6	289.3	340	267	1.019
34.8	291.5	360	323	0.974
35.3	309.2	380	346	0.970
35.5	322.2	400	409	0.933
33.6	297.3	420	433	0.930

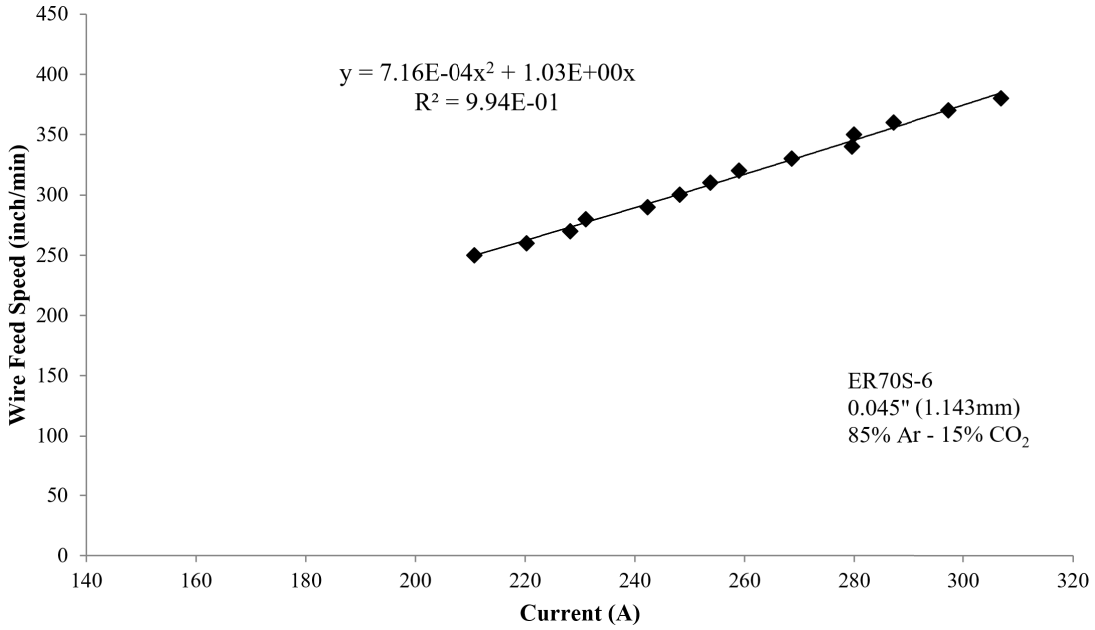

Fig. D.4: Bead on plate deposition rates as a function of current for a 0.045 in. (1.143 mm) ER70S-6 electrode with 85% Ar - 15% CO_2 shielding gas. Electrode extension was 12.5 mm (0.5 in.). See Table D.5 for details.

Table D.5: Tabulated values shown in Figure D.4. Welding results for a 0.045 in. (1.143 mm) ER70S-6 electrode with 85% Ar - 15% CO_2 shielding gas. Electrode extension was 12.5 mm (0.5 in.).

85% Ar - 15% CO2				
Average Voltage (V)	Average Current (A)	Wire Feed Speed (inch/min)	Frequency of Detachment (Hz)	Droplet Diameter (mm)
30.6	211.0	250	32	1.864
30.9	220.5	260	50	1.629
31.7	228.4	270	58	1.571
32.0	231.2	280	84	1.405
33.1	242.4	290	61	1.580
34.6	248.3	300	64	1.574
34.8	253.8	310	102	1.362
35.1	259.1	320	109	1.345
35.3	268.6	330	176	1.158
35.4	279.6	340	204	1.114
35.5	279.9	350	223	1.092
35.7	287.2	360	222	1.104
36.0	297.3	370	242	1.082
36.3	306.9	380	250	1.081

A parabolic trend was associated for each shielding gas blend as shown in Figures D.1-D.4. It was assumed that these trends must pass through 0. The experimental current ranged from approximately 150-310 A. Using equations D.1, overall anode fall voltage was calculated for the tested current range as shown in Figure D.5 and Table D.6. Overall anode fall voltage

predictions outside this range begin to deviate rapidly with extrapolated values as shown in Figure D.6.

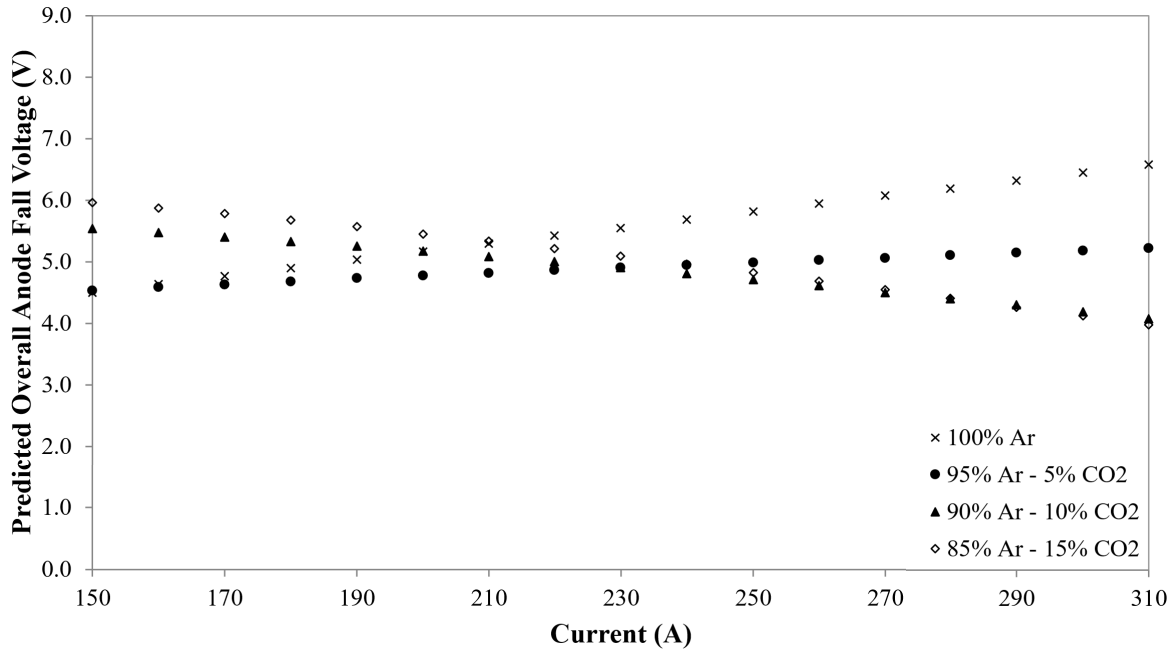

Fig. D.5: Prediction of overall anode fall voltage from experimental deposition rates with various shielding gas blends for a 0.045 in. (1.143 mm) ER70S-6 electrode. Electrode extension and arc length were both 12.5 mm (0.5 in.) throughout calculations. See Table D.6 for exact prediction values.

Table D.6: Prediction of overall anode fall voltage from experimental deposition rates with various shielding gas blends for a 0.045 in. (1.143 mm) ER70S-6 electrode. Electrode extension and arc length were both 12.5 mm (0.5 in.) throughout calculations.

	Overall Anode Fall Voltage Prediction (V)			
Current (A)	100% Ar	95% Ar - 5% CO2	90% Ar - 10% CO2	85% Ar - 15% CO2
150	4.50	4.53	5.54	5.97
160	4.63	4.58	5.47	5.87
170	4.77	4.63	5.41	5.78
180	4.90	4.68	5.33	5.67
190	5.03	4.73	5.25	5.57
200	5.16	4.77	5.17	5.45
210	5.29	4.82	5.08	5.33
220	5.42	4.86	4.99	5.21
230	5.55	4.90	4.90	5.09
240	5.68	4.95	4.81	4.96
250	5.81	4.99	4.71	4.82
260	5.94	5.03	4.61	4.69
270	6.07	5.07	4.51	4.55
280	6.20	5.10	4.40	4.41
290	6.32	5.14	4.30	4.27
300	6.45	5.18	4.19	4.12
310	6.58	5.22	4.08	3.98
Average	5.55	4.89	4.87	5.04

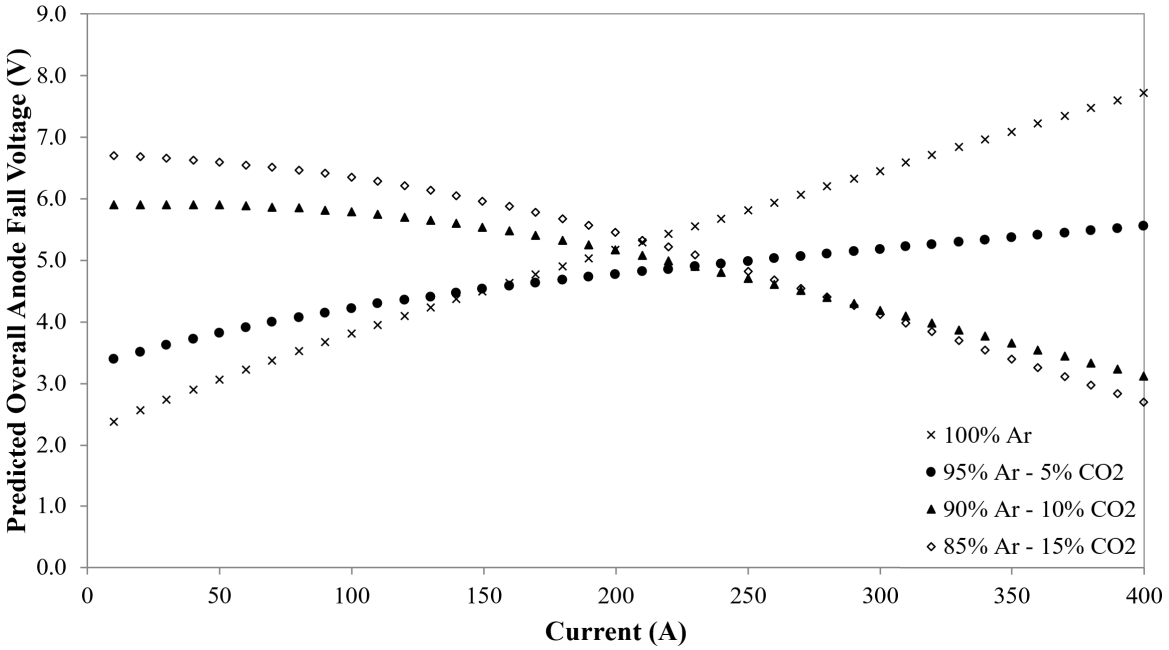

Fig. D.6: Predicted overall anode fall voltage for extrapolated values outside of Figure D.5. Prediction of overall anode fall voltage from experimental deposition rates with various shielding gas blends for a 0.045 in. (1.143 mm) ER70S-6 electrode. Electrode extension and arc length were both 12.5 mm (0.5 in.) throughout calculations.

D.4. Deposition Rate Conclusions

Overall predicted anode fall voltage was 5.09 V as shown in Table D.6. As outlined in section 3.4.2, overall anode fall voltage was 4.7 ± 0.6 V and 4.5 ± 0.5 V for 100% Ar and 95% Ar - 5% CO_2 respectively. Comparing these two different methods indicates that these results are similar and that overall anode fall voltage is approximately 5.0 V to 5.2 V when evaporation is included. As mentioned in section 3.5.2, evaporation will account for approximately 0.05 V to 0.45 V of additional voltage loss depending on welding parameters and electrode composition [3, 14, 15, 41]. These losses should be included in the calorimeters measurement of overall anode fall voltage for proper fall voltage values. As shown in Figure D.6, using the extrapolated values of wire feed speed results in a very large amount of variation in overall anode fall voltage. These tests have shown that both the calorimeter and deposition rate calculations will determine similar anode fall voltage values at tested currents. Although more complex, the calorimeter setup measures multiple voltage loss regions simultaneously which can provide additional insight into the arc column.

Appendix E: Matlab Scripts

E.1. Calorimeter Enthalpy Calculation

```
% This code allows for the calculation of the calorimeter interpolation
% functions. The c values are geometry specific, therefore if the locations
% of the thermocouples change they will have to be recalculated.

% import data from text file. Change directory to call the file of
% interest.
Data=load('calorimeter.txt');
time=(0:0.1:(length(Data)-1)*0.1)';

% converging all thermocouples to the average at the start of the test.
% This is saying the the calorimeter is initially isothermal.
T1in= 1.00038716178387E+00*Data(1,1) - 2.23525911530366E-01;
T2in= 1.00383572388361E+00*Data(1,2) - 1.03302524712160E+00;
T3in= 9.99585975261211E-01*Data(1,3) - 1.97629437159787E-01;
T4in= 1.00107320973242E+00*Data(1,4) - 5.64381709063400E-01;
T5in= 1.00383556974132E+00*Data(1,5) - 1.06641745924072E+00;
T6in= 1.00458209384896E+00*Data(1,6) - 1.24979968333064E+00;
T7in= 1.00383294932949E+00*Data(1,8) - 9.98322628326948E-01;
T8in= 1.00210697060091E+00*Data(1,15) - 6.60308566463250E-01;
T9in= 1.00009937361094E+00*Data(1,16) + 2.21390078312539E-02;
T10in= 9.99815037359825E-01*Data(1,17) + 3.29002553268273E-02;

% average temperature from the first data point collected. avgT is the
% initial temperature of the calorimeter
avgT=(T1in+T2in+T3in+T4in+T5in+T6in+T7in+T8in+T9in+T10in)/10;

% find tdiff using the corrected TC values.
T1diff=T1in-avgT;
T2diff=T2in-avgT;
T3diff=T3in-avgT;
T4diff=T4in-avgT;
T5diff=T5in-avgT;
T6diff=T6in-avgT;
T7diff=T7in-avgT;
T8diff=T8in-avgT;
T9diff=T9in-avgT;
T10diff=T10in-avgT;
```

```
38
39 % if/then for linear correction function
40 if T1diff <0 TC1corrected=(1.00038716178387E+00*Data(1:end,1) - 2.23525911530366E
       -01)+abs(T1diff); end
41 if T1diff >0 TC1corrected=(1.00038716178387E+00*Data(1:end,1) - 2.23525911530366E
       -01)-abs(T1diff); end
42 if T2diff <0 TC2corrected=(1.00383572388361E+00*Data(1:end,2) - 1.03302524712160E
       +00)+abs(T2diff); end
43 if T2diff >0 TC2corrected=(1.00383572388361E+00*Data(1:end,2) - 1.03302524712160E
       +00)-abs(T2diff); end
44 if T3diff <0 TC3corrected=(9.99585975261211E-01*Data(1:end,3) - 1.97629437159787E
       -01)+abs(T3diff); end
45 if T3diff >0 TC3corrected=(9.99585975261211E-01*Data(1:end,3) - 1.97629437159787E
       -01)-abs(T3diff); end
46 if T4diff <0 TC4corrected=(1.00107320973242E+00*Data(1:end,4) - 5.64381709063400E
       -01)+abs(T4diff); end
47 if T4diff >0 TC4corrected=(1.00107320973242E+00*Data(1:end,4) - 5.64381709063400E
       -01)-abs(T4diff); end
48 if T5diff <0 TC5corrected=(1.00383556974132E+00*Data(1:end,5) - 1.06641745924072E
       +00)+abs(T5diff); end
49 if T5diff >0 TC5corrected=(1.00383556974132E+00*Data(1:end,5) - 1.06641745924072E
       +00)-abs(T5diff); end
50 if T6diff <0 TC6corrected=(1.00458209384896E+00*Data(1:end,6) - 1.24979968333064E
       +00)+abs(T6diff); end
51 if T6diff >0 TC6corrected=(1.00458209384896E+00*Data(1:end,6) - 1.24979968333064E
       +00)-abs(T6diff); end
52 if T7diff <0 TC7corrected=(1.00383294932949E+00*Data(1:end,8) - 9.98322628326948E
       -01)+abs(T7diff); end
53 if T7diff >0 TC7corrected=(1.00383294932949E+00*Data(1:end,8) - 9.98322628326948E
       -01)-abs(T7diff); end
54 if T8diff <0 TC8corrected=(1.00210697060091E+00*Data(1:end,15) - 6.60308566463250
       E-01)+abs(T8diff); end
55 if T8diff >0 TC8corrected=(1.00210697060091E+00*Data(1:end,15) - 6.60308566463250
       E-01)-abs(T8diff); end
56 if T9diff <0 TC9corrected=(1.00009937361094E+00*Data(1:end,16) + 2.21390078312539
       E-02)+abs(T9diff); end
57 if T9diff >0 TC9corrected=(1.00009937361094E+00*Data(1:end,16) + 2.21390078312539
       E-02)-abs(T9diff); end
58 if T10diff <0 TC10corrected=(9.99815037359825E-01*Data(1:end,17) +
       3.29002553268273E-02)+abs(T10diff); end
59 if T10diff >0 TC10corrected=(9.99815037359825E-01*Data(1:end,17) +
       3.29002553268273E-02)-abs(T10diff); end
```

```
60
61 % plot corrected temperatures vs. time
62 figure1 = figure('Color',[1 1 1]);
63 axes1 = axes('Parent',figure1,'LineWidth',1.25,'FontSize',10,'FontName','
       Helvetica Narrow');
64 box(axes1,'on');
65 hold(axes1,'all');
66 plot(time,TC1corrected)
67 plot(time,TC2corrected)
68 plot(time,TC3corrected)
69 plot(time,TC4corrected)
70 plot(time,TC5corrected)
71 plot(time,TC6corrected)
72 plot(time,TC7corrected)
73 plot(time,TC8corrected)
74 plot(time,TC9corrected)
75 plot(time,TC10corrected)
76 % time,TC2corrected, time,TC3corrected, time,TC4corrected, time,TC5corrected,
       time,TC6corrected, time,TC7corrected, time,TC8corrected, time,TC9corrected,
       time,TC10corrected)
77 xlabel('Time (s)','FontSize',12,'FontName','Helvetica Narrow')
78 ylabel('Temperature (K)','FontSize',12,'FontName','Helvetica Narrow')
79
80 % final temperature of the calorimeter is taken to be the average of the
81 % ten thermocouples
82 TC1max=max(TC1corrected);
83 TC2max=max(TC2corrected);
84 TC3max=max(TC3corrected);
85 TC4max=max(TC4corrected);
86 TC5max=max(TC5corrected);
87 TC6max=max(TC6corrected);
88 TC7max=max(TC7corrected);
89 TC8max=max(TC8corrected);
90 TC9max=max(TC9corrected);
91 TC10max=max(TC10corrected);
92 Tf=(TC1max+TC2max+TC3max+TC4max+TC5max+TC6max+TC7max+TC8max+TC9max+TC10max)/10
93
94 % apply interpolation functions to obtain total enthalpy
95 % c2, c3, c5, c6, c7 are all zero according to the volume integrals of the
96 % cylindrical calorimeter. all units are si and are calculated in the excel
97 % spreadsheet "Crucible Temp". if numbers on the spreadsheet change, the
98 % numbers in this code will change.
```

```
% m=mass, v=volume, r=radius, h=height
mcal=0.62296;
vcal=mcal/8930;
rcal=0.02535;
hcal=0.0331;

c1coeff=vcal;
c4coeff=(2*pi*hcal^2*rcal^2)/4;
c8coeff=(pi*hcal*rcal^4)/4;
c9coeff=(pi*hcal*rcal^4)/4;
c10coeff=(2*pi*hcal^3*rcal^2)/6;

% TC1 c values
c1TC1=0.888415841;
c4TC1=28.69415297;
c8TC1=-1893.321718;
c9TC1=-1882.532747;
c10TC1=-1275.309447;

% TC2 c values
c1TC2=0.06832373;
c4TC2=-17.37485823;
c8TC2=210.1882822;
c9TC2=-210.3273411;
c10TC2=769.7511487;

% TC3 c values
c1TC3=-0.581874393;
c4TC3=55.99537956;
c8TC3=914.0922186;
c9TC3=348.0845307;
c10TC3=-1299.737958;

% TC4 c values
c1TC4=0.550649727;
c4TC4=-48.17302694;
c8TC4=-414.6806391;
c9TC4=411.7798253;
c10TC4=954.7044722;

% TC5 c values
c1TC5=0.067165;
```

```
141 c4TC5=-17.30269254;
142 c8TC5=-578.5838209;
143 c9TC5=575.5871607;
144 c10TC5=769.4110022;
145
146 % TC6 c values
147 c1TC6=-0.578737617;
148 c4TC6=55.71974856;
149 c8TC6=1206.286075;
150 c9TC6=53.94151056;
151 c10TC6=-1294.230148;
152
153 % TC7 c values
154 c1TC7=0.548956602;
155 c4TC7=-47.99974403;
156 c8TC7=-9.718787323;
157 c9TC7=10.82680443;
158 c10TC7=950.3311622;
159
160 % TC8 c values
161 c1TC8=0.066124173;
162 c4TC8=-17.1657672;
163 c8TC8=368.3955387;
164 c9TC8=-365.2598196;
165 c10TC8=764.9853145;
166
167 % TC9 c values
168 c1TC9=-0.579416735;
169 c4TC9=55.71975117;
170 c8TC9=-227.0565751;
171 c9TC9=1480.506706;
172 c10TC9=-1292.012769;
173
174 % TC10 c values
175 c1TC10=0.550393671;
176 c4TC10=-48.11294332;
177 c8TC10=424.3994264;
178 c9TC10=-422.6066297;
179 c10TC10=952.1072227;
180
181 % temperature to enthalpy for each tc
182 % enthalpy vs T for copper (J/kg) AVERAGE OF ALL SOURCES w/o MILLS TO 800K
```

```
183 HcuTC1=3.996237E+02*TC1corrected - 1.191949E+05;
184 HcuTC2=3.996237E+02*TC2corrected - 1.191949E+05;
185 HcuTC3=3.996237E+02*TC3corrected - 1.191949E+05;
186 HcuTC4=3.996237E+02*TC4corrected - 1.191949E+05;
187 HcuTC5=3.996237E+02*TC5corrected - 1.191949E+05;
188 HcuTC6=3.996237E+02*TC6corrected - 1.191949E+05;
189 HcuTC7=3.996237E+02*TC7corrected - 1.191949E+05;
190 HcuTC8=3.996237E+02*TC8corrected - 1.191949E+05;
191 HcuTC9=3.996237E+02*TC9corrected - 1.191949E+05;
192 HcuTC10=3.996237E+02*TC10corrected - 1.191949E+05;
193
194 % enthalpy vs T for copper (J/kg) Mills interpolated to 800K
195 % HcuTC1=4.13290735E+02*TC1corrected - 1.24873099E+05;
196 % HcuTC2=4.13290735E+02*TC2corrected - 1.24873099E+05;
197 % HcuTC3=4.13290735E+02*TC3corrected - 1.24873099E+05;
198 % HcuTC4=4.13290735E+02*TC4corrected - 1.24873099E+05;
199 % HcuTC5=4.13290735E+02*TC5corrected - 1.24873099E+05;
200 % HcuTC6=4.13290735E+02*TC6corrected - 1.24873099E+05;
201 % HcuTC7=4.13290735E+02*TC7corrected - 1.24873099E+05;
202 % HcuTC8=4.13290735E+02*TC8corrected - 1.24873099E+05;
203 % HcuTC9=4.13290735E+02*TC9corrected - 1.24873099E+05;
204 % HcuTC10=4.13290735E+02*TC10corrected - 1.24873099E+05;
205
206 % enthalpy vs T for copper (J/kg) White interpolated to 450K
207 % HcuTC1=3.921148E+02*TC1corrected - 1.170866E+05;
208 % HcuTC2=3.921148E+02*TC2corrected - 1.170866E+05;
209 % HcuTC3=3.921148E+02*TC3corrected - 1.170866E+05;
210 % HcuTC4=3.921148E+02*TC4corrected - 1.170866E+05;
211 % HcuTC5=3.921148E+02*TC5corrected - 1.170866E+05;
212 % HcuTC6=3.921148E+02*TC6corrected - 1.170866E+05;
213 % HcuTC7=3.921148E+02*TC7corrected - 1.170866E+05;
214 % HcuTC8=3.921148E+02*TC8corrected - 1.170866E+05;
215 % HcuTC9=3.921148E+02*TC9corrected - 1.170866E+05;
216 % HcuTC10=3.921148E+02*TC10corrected - 1.170866E+05;
217
218 % enthalpy vs T for copper (J/kg) Thermocalc interpolated to 450K
219 % HcuTC1=4.360650E+02*TC1corrected - 1.299474E+05;
220 % HcuTC2=4.360650E+02*TC2corrected - 1.299474E+05;
221 % HcuTC3=4.360650E+02*TC3corrected - 1.299474E+05;
222 % HcuTC4=4.360650E+02*TC4corrected - 1.299474E+05;
223 % HcuTC5=4.360650E+02*TC5corrected - 1.299474E+05;
224 % HcuTC6=4.360650E+02*TC6corrected - 1.299474E+05;
```

```
% HcuTC7=4.360650E+02*TC7corrected - 1.299474E+05;
% HcuTC8=4.360650E+02*TC8corrected - 1.299474E+05;
% HcuTC9=4.360650E+02*TC9corrected - 1.299474E+05;
% HcuTC10=4.360650E+02*TC10corrected - 1.299474E+05;

% enthalpy vs T for copper (J/kg) Stephens interpolated to 450K
% HcuTC1=3.759583E+02*TC1corrected - 1.120356E+05;
% HcuTC2=3.759583E+02*TC2corrected - 1.120356E+05;
% HcuTC3=3.759583E+02*TC3corrected - 1.120356E+05;
% HcuTC4=3.759583E+02*TC4corrected - 1.120356E+05;
% HcuTC5=3.759583E+02*TC5corrected - 1.120356E+05;
% HcuTC6=3.759583E+02*TC6corrected - 1.120356E+05;
% HcuTC7=3.759583E+02*TC7corrected - 1.120356E+05;
% HcuTC8=3.759583E+02*TC8corrected - 1.120356E+05;
% HcuTC9=3.759583E+02*TC9corrected - 1.120356E+05;
% HcuTC10=3.759583E+02*TC10corrected - 1.120356E+05;

% enthalpy vs T for copper (J/kg) Mills interpolated to 450K
% HcuTC1=3.945946E+02*TC1corrected - 1.178054E+05;
% HcuTC2=3.945946E+02*TC2corrected - 1.178054E+05;
% HcuTC3=3.945946E+02*TC3corrected - 1.178054E+05;
% HcuTC4=3.945946E+02*TC4corrected - 1.178054E+05;
% HcuTC5=3.945946E+02*TC5corrected - 1.178054E+05;
% HcuTC6=3.945946E+02*TC6corrected - 1.178054E+05;
% HcuTC7=3.945946E+02*TC7corrected - 1.178054E+05;
% HcuTC8=3.945946E+02*TC8corrected - 1.178054E+05;
% HcuTC9=3.945946E+02*TC9corrected - 1.178054E+05;
% HcuTC10=3.945946E+02*TC10corrected - 1.178054E+05;

% v- interpolation function for each thermocouple. integrated form of hi,
% units are m^3
v1=c1coeff*c1TC1+c4coeff*c4TC1+c8coeff*c8TC1+c9coeff*c9TC1+c10coeff*c10TC1;
v2=c1coeff*c1TC2+c4coeff*c4TC2+c8coeff*c8TC2+c9coeff*c9TC2+c10coeff*c10TC2;
v3=c1coeff*c1TC3+c4coeff*c4TC3+c8coeff*c8TC3+c9coeff*c9TC3+c10coeff*c10TC3;
v4=c1coeff*c1TC4+c4coeff*c4TC4+c8coeff*c8TC4+c9coeff*c9TC4+c10coeff*c10TC4;
v5=c1coeff*c1TC5+c4coeff*c4TC5+c8coeff*c8TC5+c9coeff*c9TC5+c10coeff*c10TC5;
v6=c1coeff*c1TC6+c4coeff*c4TC6+c8coeff*c8TC6+c9coeff*c9TC6+c10coeff*c10TC6;
v7=c1coeff*c1TC7+c4coeff*c4TC7+c8coeff*c8TC7+c9coeff*c9TC7+c10coeff*c10TC7;
v8=c1coeff*c1TC8+c4coeff*c4TC8+c8coeff*c8TC8+c9coeff*c9TC8+c10coeff*c10TC8;
v9=c1coeff*c1TC9+c4coeff*c4TC9+c8coeff*c8TC9+c9coeff*c9TC9+c10coeff*c10TC9;
v10=c1coeff*c1TC10+c4coeff*c4TC10+c8coeff*c8TC10+c9coeff*c9TC10+c10coeff*c10TC10;

```

```
% total calorimeter enthalpy- sum of interpolation function multiplied by
% thermocouple measurements converted to enthalpy
% units are J
Htot=8930*(HcuTC1*v1+HcuTC2*v2+HcuTC3*v3+HcuTC4*v4+HcuTC5*v5+HcuTC6*v6+HcuTC7*v7+
    HcuTC8*v8+HcuTC9*v9+HcuTC10*v10);
Hcal=(max(Htot)-min(Htot));

% calibration function
calib=0.1046*(Tf-298);

% overall enthalpy
Hcaltot=Hcal-Hcal*(3.5992/100)+Hcal*(calib/100)

% plot of total enthalpy vs. time
figure2 = figure('Color',[1 1 1]);
axes1 = axes('Parent',figure2,'LineWidth',1.25,'FontSize',12,'FontName','Time New
    Roman');
box(axes1,'on');
hold(axes1,'all');
plot(time,Htot)
xlabel('Time (s)','FontSize',12,'FontName','Times New Roman');
ylabel('Enthalpy (J)','FontSize',12,'FontName','Times New Roman');

% enthalpy as a function of z and time.
% H(o,o,z,t)=sum(hi(o,o,z,t)*Hi)
% this is looking at how enthalpy changes along the z axis while time is
% changing. the non-integrated form is used because we are looking at
% profiles, not at overall enthalpy of the volume. hi's are dimensionless,
% HcuTCi is in J/kg.
% z=(0:(hcal/49):hcal)';
% h1=(c1TC1+c4TC1*z+c10TC1*z.^2)';
% h2=(c1TC2+c4TC2*z+c10TC2*z.^2)';
% h3=(c1TC3+c4TC3*z+c10TC3*z.^2)';
% h4=(c1TC4+c4TC4*z+c10TC4*z.^2)';
% h5=(c1TC5+c4TC5*z+c10TC5*z.^2)';
% h6=(c1TC6+c4TC6*z+c10TC6*z.^2)';
% h7=(c1TC7+c4TC7*z+c10TC7*z.^2)';
% h8=(c1TC8+c4TC8*z+c10TC8*z.^2)';
% h9=(c1TC9+c4TC9*z+c10TC9*z.^2)';
% h10=(c1TC10+c4TC10*z+c10TC10*z.^2)';

% H at 18.7 seconds
```

```
307 % H1=mcal*(h1*HcuTC1(187,1)+h2*HcuTC2(187,1)+h3*HcuTC3(187,1)+h4*HcuTC4(187,1)+h5
      *HcuTC5(187,1)+h6*HcuTC6(187,1)+h7*HcuTC7(191,1)+h8*HcuTC8(187,1)+h9*HcuTC9
      (187,1)+h10*HcuTC10(187,1));
308 % H at 19.1 seconds for diferent z depths specified above
309 % H2=mcal*(h1*HcuTC1(191,1)+h2*HcuTC2(191,1)+h3*HcuTC3(191,1)+h4*HcuTC4(191,1)+h5
      *HcuTC5(191,1)+h6*HcuTC6(191,1)+h7*HcuTC7(191,1)+h8*HcuTC8(191,1)+h9*HcuTC9
      (191,1)+h10*HcuTC10(191,1));
310 % H at 19.5 seconds
311 % H3=mcal*(h1*HcuTC1(195,1)+h2*HcuTC2(195,1)+h3*HcuTC3(195,1)+h4*HcuTC4(195,1)+h5
      *HcuTC5(195,1)+h6*HcuTC6(195,1)+h7*HcuTC7(195,1)+h8*HcuTC8(195,1)+h9*HcuTC9
      (195,1)+h10*HcuTC10(195,1));
312 % H at 26.6 seconds
313 % H4=mcal*(h1*HcuTC1(266,1)+h2*HcuTC2(266,1)+h3*HcuTC3(266,1)+h4*HcuTC4(266,1)+h5
      *HcuTC5(266,1)+h6*HcuTC6(266,1)+h7*HcuTC7(266,1)+h8*HcuTC8(266,1)+h9*HcuTC9
      (266,1)+h10*HcuTC10(266,1));
314 % H at 36.5 seconds
315 % H5=mcal*(h1*HcuTC1(365,1)+h2*HcuTC2(365,1)+h3*HcuTC3(365,1)+h4*HcuTC4(365,1)+h5
      *HcuTC5(365,1)+h6*HcuTC6(365,1)+h7*HcuTC7(365,1)+h8*HcuTC8(365,1)+h9*HcuTC9
      (365,1)+h10*HcuTC10(365,1));
316 % H at 61.3 seconds
317 % H6=mcal*(h1*HcuTC1(613,1)+h2*HcuTC2(613,1)+h3*HcuTC3(613,1)+h4*HcuTC4(613,1)+h5
      *HcuTC5(613,1)+h6*HcuTC6(613,1)+h7*HcuTC7(613,1)+h8*HcuTC8(613,1)+h9*HcuTC9
      (613,1)+h10*HcuTC10(613,1));
318
319 % plotting H vs. depth for  different times
320 % figure4 = figure('Color',[1 1 1]);
321 % axes1 = axes('Parent',figure4,'XDir','reverse');
322 % xlim(axes1,[0 0.0331]);
323 % box(axes1,'on');
324 % hold(axes1,'all');
325 % plot(z,H1,z,H2,z,H3,z,H4,z,H5,z,H6);
326 % xlabel('Surface to Bottom of Cal. (m)');
327 % ylabel('Enthalpy (J)');
328
329
330 % These lines were used to calculate initial temperatures based on the
331 % calorimeter enthalpy and the thermophysical properites of the electrode
332 % material. Caution should be used when calculating for the Ni/WC wires as
333 % the enthalpy balance changes if some WC dissolves.
334
335 % FOR Castolin NiWC:
336
```

```
337 % melting point of nickel (K)
338 % Tmnickel=1728;
339 % Mdep=7.36;
340
341 % enthaply functions. all are functions of temperature and have constants
342 % that have been omitted because they will cancel. All T's are in K.
343 % fractions are weight percent.
344
345 % solid wire
346 % H= 0.40096061*T - 130.37432249
347
348 % liquid wire
349 %  H=0.48647515*T - 118.40023369
350 % A = 0.48647515;
351 %
352 % Hsolid = 0.40096061*(Tmnickel-Tf);
353 % Hfus = 159;
354 % Hliq = (Hcaltot/Mdep)-Hfus-Hsolid;
355 %
356 % Ti=(Hliq/A)+ Tmnickel
357
358
359 % CTC Wire:
360
361 % melting point of nickel (K)
362 % Tmnickel=1676;
363 % Mdep=5.43;
364
365 % enthaply functions. all are functions of temperature and have constants
366 % that have been omitted because they will cancel. All T's are in K.
367 % fractions are weight percent.
368
369 % solid wire
370 % H= 0.3554*T - 120.869
371 % B = 0.3554;
372 % liquid wire
373 % H=0.6419*T - 402.11
374 % A = 0.6419;
375 %
376 % Hsolid = B*(Tmnickel-Tf);
377 % Hfus = 181.3;
378 % Hliq = (Hcaltot/Mdep)-Hfus-Hsolid;
```

```
379 %
380 % Ti=(Hliq/A)+ Tmnickel
381
382 % FOR TIN CALIBRATION:
383
384 % enthalpy of fusion (J/g), melting temp (K), and mass (g) of Sn:
385 % Hfussn=60.61;
386 % Tfussn=505.12;
387 % msn=33.86;
388
389 % Initial Sn temp (K). TC9 is channel 18, column 19. TC10 is channel 19 column
        20:
390 % sn1TC9=1.004937083806E+00*Data(1:end,17) + 1.409474177953E-01;
391 % sn2TC10= 1.009807897595E+00*Data(1:end,18) - 1.006894429918E-01;
392 % avgTsn=(sn1TC9+sn2TC10)/2;
393 % Tsnin=max(avgTsn);
394
395
396 % Final Sn temp (K)
397 % Tsnfin=(TC2max+TC5max+TC8max)/3;
398
399 % solid enthalpy funcion (J/g):
400 % H = 0.000080*T^2 + 0.180125*T - 7.531335
401
402 % liquid enthalpy function (J/g):
403 % H = 0.238060*T + 44.622550
404
405 % A=0.00008;
406 % B=0.180125;
407 % D=0.238060;
408
409 % Sn enthalpy (J):
410 % Hsn=(0.238060*(Tsnin-Tfussn) + Hfussn + ((0.000080*Tfussn^2 + 0.180125*Tfussn)
        -(0.000080*Tsnfin^2 +0.180125*Tsnfin)))*msn
411
412 % Initial temp of tin based on calorimeter enthalpy:
413 % Tsnfromcal=((-A*Tfussn^2-B*Tfussn+A*Tsnfin^2+B*Tsnfin-Hfussn)/D)+(Hcaltot/(msn*
        D))+Tfussn
414
415 % FOR STEEL TRIALS:
416 % enthalpy functions for pure iron in J/g. constant will cancel so they are
417 % disregarded
```

```
418
419 % Transition temperatures (K)
420 %Tfus=1811;
421 %Talphagamma=1184;
422
423 % Ferrite
424 %H = 0.0003*(Tf)^2 + 0.2029*Tf - 86.244;
425 %A=0.00032194;
426 %B=0.20289;
427 %dHferrite=A*(Talphagamma^2-Tf^2)+B*(Talphagamma-Tf);
428
429 % gamma/delta
430 %H = 0.6893*Tf - 208.17;
431 %D=0.689253;
432 %dHgammadelta=D*(Tfus-Talphagamma);
433
434 % liquid
435 %H = 0.8302*Tf - 205.77;
436 %F=0.830154;
437
438 % fusion (J/g)
439 %Hfus=247;
440
441 % Mass of deposition (g)
442 %mfe=load('DropMass.txt');
443
444 % Heat input of droplet (J/g)
445 %Hdroptot=Hcaltot/mfe
446
447 % initial droplet temperature
448 %Ti=((Hcaltot/(F*mfe))-(A*(Talphagamma^2-Tf^2)+B*(Talphagamma-Tf)-D*(Tfus-
        Talphagamma)-Hfus)/F)+Tfus;
449 %dHliq=(Hcaltot/mfe)-dHferrite-dHgammadelta-Hfus;
450
451 %Ti=(dHliq/F)+Tfus
452
453 % FOR ALUMINIUM TRIALS:
454 % enthalpy functions for pure iron in J/g. constant will cancel so they are
455 % disregarded
456
457 % Transition temperatures (K)
458 Tmelt = 887.15;
```

```
459
460 %fusion (J/g)
461 Hfus = 425;
462
463 % Solid (J/g)
464 dHsolid = 1.0074*Tf-309.33;
465
466 % Mass of deposition (g)
467 mfe=load('DropMass.txt');
468
469 % Heat input of droplet (J/g)
470 Hdroptot=Hcaltot/mfe
471
472 %inital droplet temperature
473 dHliq = Hdroptot-Hfus-dHsolid;
474 Ti = (dHliq-151.22)/1.0147
475
476 % ****END OF CODE****
```

E.2. Cathode Enthalpy Calculation

```
% ****BEGIN COPY HERE****

% import data from text file. Change directory to call the file of
% interest.

Data=load('calorimeter.txt');
time=(0:0.1:(length(Data)/10-1)*0.1)';

% Flow rate of water (Gallons per minute)
GPM = 0.29;

% Calls the specific cathode thermocouples
T11in= Data(1,7);
T12in= Data(1,18);

% initial temperature of the water before welding is the average of the two
% thermocouples
avgT=(T11in+T12in)/2;

% Takes the difference of the two thermocopules from the average
T11diff=T11in-avgT;
T12diff=T12in-avgT;

% if/then for correction function. This will change all data points
% relative to the starting initial TC temperature.
if T11diff <=0 TC11corrected= Data(1:length(Data)/10,7)+abs(T11diff); end
if T11diff >0 TC11corrected= Data(1:length(Data)/10,7)-abs(T11diff); end
if T12diff <=0 TC12corrected= Data(1:length(Data)/10,18)+abs(T12diff); end
if T12diff >0 TC12corrected= Data(1:length(Data)/10,18)-abs(T12diff); end

% plot the cathode thermocouples
figure1 = figure('Color',[1 1 1]);
axes1 = axes('Parent',figure1,'LineWidth',1.25,'FontSize',10,'FontName','
    Helvetica Narrow');
box(axes1,'on');
hold(axes1,'all');
plot(time,TC11corrected)
plot(time,TC12corrected)
xlabel('Time (s)','FontSize',12,'FontName','Helvetica Narrow')
ylabel('Temperature (K)','FontSize',12,'FontName','Helvetica Narrow')
```

```
40
41 % Maximum temperature water reached (Average of 9 points around the maximum point
       )
42 [M, I] = max(TC11corrected(:));
43 MaxTemp = mean( TC11corrected([I-4 I-3 I-2 I-1 I I+1 I+2 I+3 I+4]))
44 MaxDifference = MaxTemp - mean(TC12corrected([I-4 I-3 I-2 I-1 I I+1 I+2 I+3 I+4])
       )
45
46 % Calculate the enthalpy vs T for water (J/s) reference P.E. Liley
47 % interpolated from 273K to 323K.
48 HcuTC11=(4.1853*TC11corrected-1142.5)*GPM*6.309E-05*1000000;
49 HcuTC12=(4.1853*TC12corrected-1142.5)*GPM*6.309E-05*1000000;
50
51 % total enthalpy of water (J/s) (Average of 9 points around the maximum point)
52 Hwater = mean(HcuTC11([I-4 I-3 I-2 I-1 I I+1 I+2 I+3 I+4]))-mean(HcuTC12([I-4 I-3
       I-2 I-1 I I+1 I+2 I+3 I+4]))
53
54 % ****END OF CODE****
```

E.3. Data Acquisition Analysis

```
clear all

% Import data from Text file
Data=load('After_Averaging.txt');

% For running my data:
A=[0:0.0001:(length(Data)-1)*0.0001]';
B=Data(:,2);
C=Data(:,3);

time=A;
current=B;
voltage=C;

% for running Erik's data
% A=[0:0.0002:(length(Data)-1)*0.0002]';
% B=Data(:,3);
% C=Data(:,2);
%
% time=A;
% current=B*150;
% voltage=C*10;

%Data analysis
avoltage = mean(voltage);
acurrent = mean(current);
stdvoltage = std(voltage);
stdcurrent = std(current);
AvgPower = avoltage*acurrent;
RMSvoltage = sqrt(mean(voltage.*voltage));
RMScurrent = sqrt(mean(current.*current));
RMSPower = RMSvoltage*RMScurrent;
AriPower = mean(voltage.*current);

%Sampling rate used during testing
samprate = (time(2)- time(1)).^-1

%FFT analysis for voltage signal
fftvolt = fft(voltage);
N = length(fftvolt);
```

```
41 fftvolt(1) = [];
42 power = abs(fftvolt(1:N/2)).^2;
43 nyquist = 1/2 * samprate;
44 voltfreq = (1:N/2)/(N/2)*nyquist;
45 sortpower = sort(power,'descend');
46
47 for i=1:3;
48
49     indexv(i) = voltfreq(find(power==sortpower(i)));
50
51 end
52
53 %FFT analysis for current signal
54 fftcurrent = fft(current);
55 Nc = length(fftcurrent);
56 fftcurrent(1) = [];
57 currentpower = abs(fftcurrent(1:Nc/2)).^2;
58 currentfreq = (1:Nc/2)/(Nc/2)*nyquist;
59 sortcurrentpower = sort(currentpower,'descend');
60
61 for j=1:3;
62
63     indexc(j) = currentfreq(find(currentpower==sortcurrentpower(j)));
64
65 end
66
67 %Create figures showing all data values calculated and FFT analysis
68 Statistics = figure;
69
70 annotation1 = annotation(...
71 Statistics,'textbox',...
72 'Position',[0 0 1 1],...
73 'BackgroundColor',[1 1 1],...
74 'FitHeightToText','on',...
75 'HorizontalAlignment','center',...
76 'String',{'average voltage = ',avoltage,'',...
77 'standard deviation voltage =',stdvoltage,'',...
78 'average current = ',acurrent,'',...
79 'standard deviation current = ',stdcurrent,'',...
80 'average power = ',AvgPower,'',...
81 'RMS voltage = ',RMSvoltage,'',...
82 'RMS current = ',RMScurrent,'',...
```

```
'RMS power = ',RMSPower,'' ,...
'Arithmetic power = ',AriPower,'' ,...
'most popular detachment frequency based on voltage = ', indexv,''...
'most popular detachment frequency base on current = ', indexc,''});


scrsz = get(0,'ScreenSize');
figure1 = figure('Position',[5 scrsz(4)/3 scrsz(3)/1 scrsz(4)/2]);
propertyeditor('on');

axes1 = axes('Position',[0.09 0.60 0.45 0.37],'Parent',figure1);
box('on');
hold('all');
plot1 = plot(time,voltage,'Red', 'Parent', axes1);
xlabel('Time (seconds)');
ylabel('Voltage');

axes2 = axes('Position',[0.09 0.10 0.45 0.37],'Parent',figure1);
box('on');
plot2 = plot(time,current,'Parent',axes2);
xlabel('Time (seconds)');
ylabel('Current (Amperes)');

axes3 = axes('Position',[0.5703 0.6 0.34 0.34],'Parent',figure1);
box('on');
hold('all');
plot3 = plot(voltfreq, power, 'red');
xlim([0 500]);
grid on;
xlabel('Frequency');

axes4 = axes('Position',[0.5703 0.10 0.34 0.34],'Parent',figure1);
box('on');
hold('all');
plot4 = plot(currentfreq, currentpower, 'blue');
xlim([0 500]);
grid on;
xlabel('Frequency');
```

E.4. High Speed Video Synchronization

```
%%%%%%%%%%%%%%%%%%%%%%%%%%%%%%Animation.m%%%%%%%%%%%%%%%%%%%%%%%%%%%%%%%%%%

%Original code created by Erik Soderstrom, Colorado School of Mines, Golden, CO
%Reworked code created by Cory McIntosh, University of Alberta, Edmonton, AB

%Last Edited: March 23, 2016

%The following lines of code are used to generate an animation that
%displays voltage or current signals in the same figure. The purpose of
%this file is to create a movie displaying a voltage or current plot in
%relation to time. This plot can then be used in conjunction with high
%speed video to produce synchronized data acquisition and high speed
%videos. This program does not perform the synchronization but uses the
%data obtained from the synchronized data acquired through the PCC 1.3 software
%and data acquisition.

%The lines of code can be modified in this file for specific data files,
%copied, and then pasted into the MATLAB command window. Comments below
%indicate where to begin and end copying the code.  Once the code is
%copied, simply paste into the MATLAB command window on the command line
%and execute. Several preparations need to be done in order for this
%program to work. Because the program calls specific '.txt' files and
%the correct names need to be entered. The voltage signal that is displayed
%in the animation comes from a file also used for data analysis. This
%program assumes the import file is properly sychronized with the video
%associated with it. The voltage or current file must contain the time in
%the first column, unconditioned voltage or current signal in the second
%column and no headers.  This program will condition the input signals
%by multiplying the voltage or current values by a specified amount.

%Any further comments will describe the command directly following it.

%Start program.

%Closes all previous opened figures in Matlab

close all

%Matlab uses the VideoWriter to create the video file. Files will be saved
%as '(name).avi'. writerObj refers to the overall video project. Change the
```

```
41 %framerate to adjust to the desired playing framerate (default is 30 fps).
42
43 writerObj = VideoWriter('Voltage_Video.avi');
44 writerObj.FrameRate = 27;
45 open(writerObj);
46
47 %Sets all figures in Matlab with default look (Black background with white
48 % axes). Change colors for customization.
49
50 set(0,'defaultfigurecolor','k')
51
52 set(0,'DefaultAxesColor','w')
53
54 %Import voltage or current data file 'Voltage_Edited.txt' into matrix
55 %'ndata'.  For more information on importing data, go to MATLAB help
56 %(press F1), and search for the MATLAB function 'dlmread'.
57
58 ndata = dlmread('After_Averaging.txt');
59
60 %Label the first column in matrix 'ndata', which is time.  Label the
61 %second column in matrix 'ndata', which is unconditioned voltage or current.
62 %MATLAB uses the apostrophe operator (') to perform a transpose of the
63 %matrix.  Because the matrix is not symmetric, the columns need to be
64 %transposed into rows to simplify further operations.
65
66 time = ndata(:,1)';
67 voltage = ndata(:,3)';
68
69 %The variable 's' is a time related parameter that is defined as the
70 %inverse of the high speed videos recording framerate.  For example, if the
71 %video is recorded at 2000 fps, s = 0.0005. The variable 's' will be used
72 %later to advance the time scale for the voltage signal a fixed amount,
73 %which must correspond to the advancing video footage.
74
75 s = 1/5000;
76
77 % Create a 'for' loop that will generate successive images within the
78 % figure that will be compiled into the final video.  The matrix 'k'
79 % represents the number of iterations that will be performed.  Anything
80 % between the 'for' and 'end' commands will be repeated during each
81 % iteration.  The size of the 'k' matrix is important.  For example, if
82 % video was recorded at 2000 fps and the matrix is made 1:2000, a total of
```

```
% 1 real second of video will be processed.  Use caution - about 1 Gb of ram
% memory runs out around 1250 frames.  The progam will encounter an error
% and terminate. If large sized for loops are used, exit all other open
% programs

for k = 1:3000

% Create the plot that will contain the time and voltage plot.  More
% information under MATLAB help 'plot'.

    plot(time,voltage,'k')

% The 'xlim' function defines the limits of the x-axis for the voltage
% plot.  In order to animate the voltage plot, the values of the x-axis
% need to change with every iteration.  In this case, the voltage plot will
% being with the marker centered over 0 s, with the limits ranging from
% -0.01 s to 0.01 s.  With each iteration ('k' value), the x limits will
% shift a value 's', defined above as the inverse of framerate.  The y
% limits can also be changed, depending on the welding parameters used.

    xlim([(s*k)-0.010001  0.010001+(s*k)]);
    ylim([20  35]);

% Create a vertical line in center of the voltage plot that will serve as a
% visual indicator, aka 'the marker', of the current position of the video.

    annotation('line',[0.5172  0.5172],[0.95  0.11]);

% Create a label for the x-axis of the voltage plot.  Because the x-axis is
% time, the label is 'Time (seconds)'.

    xlabel('Time(s)','Color','w','fontsize',18);
    set(gca,'XColor','w','fontsize',12);

% Create a label for the y-axis of the voltage or current plot.  In this
% case, it is simply 'Voltage')

    ylabel('Voltage(V)','Color','w','fontsize',18);
    set(gca,'YColor','w','fontsize',12);
    set(gca, 'XTickLabel', num2str(get(gca,'XTick)','%0.3f'))

% Takes a screenshot of the current frame. The matrix M(k) will consist of
```

```
% thousands of screenshots which will be compiled into the VideoWriter.
% See MATLAB help 'getframe' for further information.

    M(k) = getframe(gcf);


end

% Compiles matrix M(k) into the writerObj to create a video

writeVideo(writerObj,M);

% Close the writerObj program

close(writerObj);

%%%%%END OF CODE%%%%%%

%%%%%%%%%%%%%%%%%%%%%%%%%%%%%%%%%%%%%%%%%%%%%%%%%%%%%%%%%%%%%%%%%%%%%%%%%%%
```